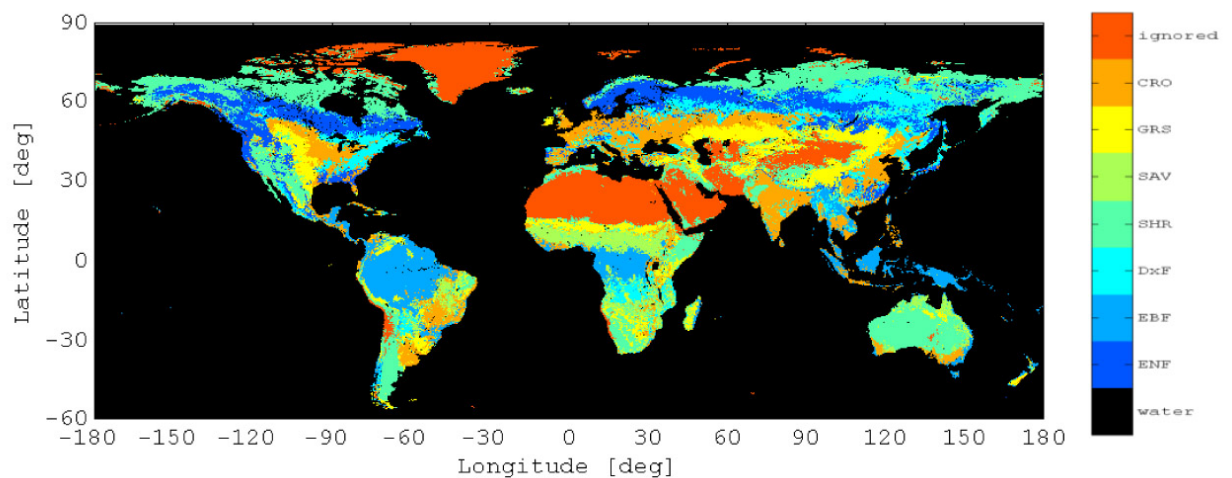# Max-Planck-Institut für Biogeochemie

TECHNICAL REPORTS
21

Quantifying carbon processes of the terrestrial biosphere in a global atmospheric inversion based on atmospheric mixing ratio, remote sensing and meteorological data

by
Bakr Badawy

MAX-PLANCK-GESELLSCHAFT

Technical Reports - Max-Planck-Institut für Biogeochemie 21, 2011

Quantifying carbon processes of the terrestrial biosphere in a global atmospheric inversion based on atmospheric mixing ratio, remote sensing and meteorological data

Dissertation

zur Erlangung des akademischen Grades doctor rerum naturalium
(Dr. rer. nat.)

durchgeführt am Max-Planck-Institut für Biogeochemie Jena

vorgelegt dem Rat der ChemischGeowissenschaftlichen Fakultät
der
Friedrich-Schiller-Universität Jena

vorgelegt von

Bakr Badawy

aus
Ägypten

Jena,

2011

Selbstständigkeitserklärung

Ich erkläre, dass ich die vorliegende Arbeit selbstständig und nur unter Verwendung der angegebenen Hilfsmittel, persönlichen Mitteilungen und Quellen angefertigt habe.

Contents

List of Figures

List of Tables

Acknowledgement

I would like to thank all people who have helped and inspired me during my doctoral study. First and foremost I offer my sincerest gratitude to my advisor Christian Rödenbeck, who has supported me throughout my thesis. His encouragement and supervision from the preliminary to the concluding level enabled me to develop an understanding of the subject. This thesis is simply impossible without him. Many thanks go to Prof. Martin Heimann for many useful discussions, advices, and insights throughout my work. I am very grateful to Prof. Christiane Schmullius, my university advisor and the chairman of my regular advisory committee meeting, for her encouragement, and useful comments. Furthermore, I would like to thank Prof. Magdy Abdel wahab, the former Head of the department of Astronomy and Meteorology, at Cairo University. He has been my teacher and mentor for many years. He offers advice and suggestions whenever I need him.

Furthermore, I would like to thank Markus Reichstein, the team leader of the MDI-BGC group, first, for the updated formula of the soil respiration model that used in this thesis, second, for his contributions and feedbacks during my regular advisory committee meetings. The MDI-BGC group has been a source of friendships as well as good advice and collaboration. I am especially grateful to Nuno Carvalhais and Martin Jung for providing the land cover map and the fAPAR data, and also for their feedbacks and useful comments. Besides, I would like to thank Miguel Mahecha for answering my questions on statistics. I am grateful for Christian Beer for providing the global field of GPP used for comparison.

I thank all my colleagues and friends at the MPI-BGC for their support. In particular, I would like to thank Gregor Schürmann for his comments and the precious suggestions. I am grateful for Julia Marshall for the time and effort she put into proofreading my thesis. I thank Julia Steinbach for all the time she dedicated to me: helping with R-programming, and with German paperwork. I am grateful for general discussions with Prof. Christoph Gerbig , Ravan Ahmadov, Huilin Chen, Dhanyalekshmi Kuttappan Pillai, Kristina Trusilova, Valentina Sicardi, Jan Winderlich, Roberto Kretschmer, Veronika Beck, Ute Karstens, Sönke Zaehle , Thomas Koch, Marc Geibel, Annette Höfer, Daniela Dalmonech, and Gionata Biavati. I thank Karen Harm, Silvana Schott, Antje Weitz and Kornelia Kampman for supporting so magnificently in every aspects throughout my PhD studies.

My deepest gratitude goes to my family in Egypt for their unflagging love and support throughout my life; this dissertation is simply impossible without them. I am indebted to my father for his care and love. Although he is no longer with us (may ALLAH bless him), he is forever remembered. My deepest gratitude goes to my mother for her everlasting love to me. Special thanks go to my brothers for their support. Finally I come to address my appreciation to my wife, Dai El-Sadani, not only for her constant encouragement but also for her patience and understanding throughout. It is difficult to find words to express my gratitude for her. Without my wife's encouragements, I would not have finished the degree. My son, Eiad, has made me enjoy the life. It is to my wife and my son I also wish to convey my considerable thanks, and it is also to them I would like to dedicate this work.

Abstract

The role of land ecosystems as sources or sinks of carbon in response to human perturbation is not well understood given the spatial heterogeneity and the temporal variability of the biospheric CO_2 exchange (Ciais et al., 2000). Therefore, understanding and quantifying the role of the land biosphere in the global carbon budget is necessary, particularly the response and feedback of carbon fluxes to climatic controls. Atmospheric CO_2 measurements have played a key role in assessing source/sink distributions on global scales using atmospheric CO_2 inversions (top-down approach) (e.g. Enting et al. (1995); Kaminski et al. (2002); Bousquet et al. (2000); Rödenbeck et al. (2003); Baker et al. (2006)). Process-based models (bottom-up approaches) of carbon fluxes are also useful tools for exploring the underlying processes involved in the uptake and release of carbon in the terrestrial biosphere. These methods on their own are unlikely to provide enough information to fully understand the biological processes driving the uptake and release of atmospheric CO_2. Therefore, within this thesis, we developed a modeling framework that couples bottom-up and top-down approaches and uses different data constraints (atmospheric CO_2 concentrations, satellite-driven data, and climate data) in order to quantify the carbon sources and sinks of the terrestrial biosphere. This allows us to better understand the underlying processes by optimizing some internal key parameters of the biosphere model in order to fit the observed CO_2 concentrations.

The bottom-up approach is represented by a data-driven Simple Diagnostic Photosynthesis and Respiration Model (SDPRM) based on pre-existing models. The ecosystem respiration (R_{eco}) model is based on the formulations introduced by Lloyd and Taylor (1994) and modified by Reichstein et al. (2003) while the photosynthesis model is based on the light use efficiency logic, suggested by Monteith (1977), for calculating the Gross Primary Production (GPP). SDPRM is driven by satellite-derived fAPAR (fraction of Absorbed Photosynthetically Active Radiation) and climate data from NCEP/NCAR. The model estimates 3-hourly values of GPP for seven major biomes and daily R_{eco}. The motivation is to provide reliable and fine-grained first guess fields of surface CO_2 fluxes for the inverse model which is presented by the standard inversion algorithm (STD-inv) introduced by Rödenbeck (2005). Then, from the coupled inversion system, fine-grained adjustments and interpretable parameters of SDPRM can be achieved based on the atmospheric information.

The simulated fluxes from SDPRM showed that the model is capable of producing real-

istic flux patterns comparable to the ones inferred from the atmospheric CO_2 inversion or inferred from the process-based models. This is promising since the model is much simpler and easier to apply than sophisticated process-based models. Different analyses were carried out to test the sensitivity of the estimated fluxes of GPP, R_{eco} and NEE to their driving forces (fAPAR and climate data). It is found that the interannual variability of NEE is mainly driven by climate. Also, the results show that temperature is a limiting factor for the interannual variability of GPP and R_{eco} over the northern hemisphere regions, in particular in the cold boreal forest. Vapor pressure deficit (VPD) is the main limiting factor of the interannual variability of GPP for the water-limited regions while radiation is the main limiting factor in tropical regions. Furthermore, the analyses show that precipitation controls the interannual variability of R_{eco} over a large area of the globe in particular over the tropics and the southern hemisphere. These results are consistent with the findings of Nemani et al. (2003).

The results of the coupled system (SDPRM-inv) are promising as they demonstrate that the method works and is capable of correcting carbon fluxes from SDPRM for annual and seasonal time scales, as well as for different processes (e.g. GPP and R_{eco}). The optimization algorithm in the system substantially reduces the a-priori uncertainties for most of the parameters (more than 88%). The optimized model produces a good fit to the seasonal cycle of atmospheric CO_2 concentrations and a moderate fit to its interannual variability. Also, based on the optimized results, the interannual variability of R_{eco} dominates the interannual variability of NEE in the tropics. Furthermore, from such a system, it has been found that some of the missing processes in SDPRM (for example biomass burning) can explain some of the differences between the flux variability simulated by the coupled system and the one seen by the atmospheric signals as has been shown for Tropical Asia in 1998.

There is a range of possible results to explore from the coupled system that can improve our understanding of the terrestrial carbon cycle. For instance, the response of the terrestrial biosphere fluxes to the climate anomalies can be investigated based on the optimized results. In addition, the coupled system is flexible enough to be modified and refined in order to include various sources of information or processes. For example, fire emissions can be added as an additional process to the model. As a further possibility, the isotopic composition of the atmospheric CO_2 (such as $^{13}CO_2$, $^{14}CO_2$) can be used to discriminate between the signals from different processes (GPP, R_{eco}, and fossil fuel burning).

Zusammenfassung

Die Rolle von Ökosystemen als Quellen oder Senken von Kohlenstoff infolge der anthropogenen Störung ist noch nicht gut verstanden, insbesondere durch die räumliche Heterogenität und zeitliche Variabilität des biosphärischen CO_2-Austauschs (Ciais et al., 2000). Deshalb ist es wichtig, die Rolle der Landbiosphäre im globalen Kohlenstoff-Budget zu verstehen und zu quantifizieren, besonders die Reaktionen und Feedbacks der Kohlenstoff-Flüsse auf klimatische Einflüsse. Atmosphärische CO_2-Messungen spielen eine Schlüsselrolle in der Untersuchung der Verteilung von Quellen und Senken auf globaler Skala, wobei atmosphärische CO_2-Inversionen zum Einsatz kommen ("Top-down approach") (e.g. Enting et al. (1995); Kaminski et al. (2002); Bousquet et al. (2000); Rödenbeck et al. (2003); Baker et al. (2006)). Prozessorientierte Modelle der Kohlenstoff-Flüsse ("Bottom-up approach") sind ebenfalls nützliche Werkzeuge, um die Prozesse zu untersuchen, die der Aufnahme und Abgabe von Kohlenstoff durch die terrestrische Biosphäre zugrunde liegen. Diese einzelnen Methoden für sich können aber noch nicht genug Informationen liefern, um die biologischen Prozesse der Aufnahme und Abgabe von Kohlenstoff voll zu verstehen. In dieser Dissertation haben wir deshalb ein Modellsystem entwickelt, das "Top-down approach" und "Bottom-up approach" koppelt und verschiedene Datenströme nutzt (atmosphärische CO_2-Konzentration, satellitenbasierte Daten, Wetterdaten). Ziel ist, die Kohlenstoff-Quellen und -Senken der Biospäre zu quantifizieren und die zugrundeliegenden Prozesse zu verstehen, indem interne Schlüsselparameter durch Anpassung an die CO_2-Beobachtungen optimiert werden.

Der "Bottom-up approach" wird durch ein daten-getriebenes einfaches Diagnostisches Photosynthese- und Respirationsmodell (SDPRM) auf der Grundlage existierender Modelle representiert. Die Ökosystem-Atmung (R_{eco}) beruht auf den Formulierungen von Lloyd and Taylor (1994) mit Änderungen nach Reichstein et al. (2003). Das Photosynthese-Modell, das die Netto-Primärproduktion (GPP) berechnet, basiert auf der "light use efficiency"-Formulierung von Monteith (1977). SDPRM wird von satellitenbasiertem fAPAR (Anteil der absorbierten photosynthetisch aktiven Strahlung) und Klimadaten von NCEP/NCAR angetrieben. Das Modell schätzt 3-stündliche Werte von GPP für 7 Haupt-Biome, sowie tägliches R_{eco}. Es stellt damit verlässliche, hochaufgelöste a-priori-Felder der CO_2-Flüsse bereit, die in der atmosphärischen Inversion (Algorithmus nach Rödenbeck (2005)) verwendet werden. Das gekoppelte System erzeugt dann hochaufgelöste Korrekturen zu den Fluss-Feldern sowie interpretierbare Parameter auf der Grundlage der atmosphärischen Information.

Die Simulationen mit SDPRM zeigen, dass das Modell in der Lage ist, realistische Fluss-Muster zu erzeugen, die mit denen aus der Standard-Inversion oder von Prozessmodellen vergleichbar sind. Das ist vielversprechend, da das Modell deutlich weniger komplex und einfacher anwendbar ist als Prozessmodelle. In verschiedenen Analysen wurde die Sensitivität der berechneten Felder von GPP, R_{eco} und NEE bezüglich ihrer Einflussfaktoren (fAPAR und Klimadaten) untersucht. Es ergibt sich, dass die interannuale Variabilität von NEE hauptsächlich von Klimadaten bestimmt ist. Temperatur ist der limitierende Faktor der interannualen Variabilität von GPP und R_{eco} in der Nordhemispäre, besonders in kalten borealen Wäldern. Dampfdruck-Defizit (VPD) ist der wichtigste limitierende Faktor der interannualen Variabilität von GPP in wasserlimierten Gebieten, während Strahlung der wichtigste limitierende Faktor in den Tropen ist. Die Analysen zeigten außerdem, dass Niederschlag die interannuale Variabilität von R_{eco} in weiten Teilen der Erde bestimmt, besonders in den Tropen und der Südhemispäre. Diese Ergebnisse sind konsistent mit Nemani et al. (2003).

Die Ergebnisse des gekoppelten Systems bestätigen das Konzept und zeigen, dass das System die Kohlenstoff-Flüsse aus dem SDPRM auf saisonaler und interannualer Zeitskala sowie für die einzelnen GPP- und R_{eco}-Komponenten korrigieren kann. Der Optimierungs-Algorithmus reduziert die a-priori-Unsicherheiten der meisten Parameter beträchtlich (über 88%). Das optimierte Modell zeigt einen guten Fit an den Jahresgang der CO_2-Konzentrationen, und einen mäßigen Fit an die interannuale Variabilität. Nach den optimierten Ergebnissen ist die interannuale Variabilität von NEE von den Tropen dominiert, die wiederum durch R_{eco} dominiert sind. Weiterhin wurde gefunden, dass Prozesse, die in SDPRM fehlen (z.B. Biomassen-Verbrennung), manche der Unterschiede zwischen der Fluss-Variabilität aus dem gekoppelten Modell und den atmospärischen Signalen erklären können, wie etwa 1998 im tropischen Asien.

Eine Reihe weiterer möglicher Ergebnisse des gekoppelten Systems können genutzt werden, unser Verstndnis des terrestrischen Kohlenstoff-Kreislaufs zu verbessern. Beispielsweise kann anhand der optimierten Ergebnisse die Reaktion der biospärischen Flüsse auf Klima-Anomalien untersucht werden. Daneben kann das gekoppelte System flexibel modifiziert und erweitert werden, um verschiedene Informationsquellen oder Prozesse hinzuzufügen. Beispielsweise können Emissionen aus Feuer als weiterer Prozess hinzugefügt werden. Eine weitere Möglichkeit besteht darin, die Isotopen-Zusammensetzung des atmosphärischen CO_2 (wie $^{13}CO_2$, $^{14}CO_2$) zu nutzen, um zwischen den Signalen verschiedener Prozesse (GPP, R_{eco}, fossile Verbrennung) zu unterscheiden.

Acronyms

CO_2	Carbon Dioxide
O_2	Oxygen
CH_4	Methane
GPP	Gross Primary Production
Ra	Autotrophic Respiration
Rh	Heterotrophic Respiration
R_{eco}	Ecosystem Respiration
NPP	Net Primary Production
NEP	Net Ecosystem Production
NEE	Net Ecosystem Exchange
NBP	Net Biome Production
NDVI	Normalized Difference Vegetation Index
PAR	Photosynthetically Active Radiation
APAR	Absorbed Photosynthetically Active Radiation
fAPAR	fraction of Absorbed Photosynthetically Active Radiation
LAI	Leaf Area Index
PFT	Plant Functional Types
VPD	Vapor Pressure Deficit
SDPRM	The Simple Diagnostic Photosynthesis and Respiration Model
STD-inv	The Standard Inversion
SDPRM-inv	The coupled inversion system (SDPRM + STD-inv)
TransCom	Atmospheric Tracer Transport Model Inter-comparison Project
CCDAS	Carbon Cycle Data Assimilation System
GIMMS	Global Inventory Modeling and Mapping Studies
AVHRR	Advanced Very High Resolution Radiometer
SYNMAP	Synergetic land cover product
EDGAR	The Emission Database for Global Atmospheric Research
GFEDv2	Global Fire Emissions Database version 2
IPCC	The Intergovernmental Panel on Climate Change
UNFCCC	The United Nations Framework Convention on Climate Change
FAO	Food and Agriculture Organization
NCEP	The National Center for Environmental Prediction
NCAR	The National Center for Atmospheric Research Reanalysis
NOAA	The National Oceanic and Atmospheric Administration
ppm	parts-per-million
PgC	1 Petagram = 1 x 10^{15} gram

Chapter 1

Introduction

1.1 Background

There is increasing evidence that Earth's climate is changing (Schär and Jendritzky, 2004; Trenberth et al., 2007; Klein Tank and Können, 2003). The Earth's climate is influenced by many factors such as the amount of incoming solar radiation and also the amount of greenhouse gases and aerosols in the atmosphere, and the properties of the Earth's surface, which determine how much of this solar energy is retained or reflected back to space. According to the 2007 Fourth Assessment Report (AR4) by the Intergovernmental Panel on Climate Change (IPCC), global surface temperature increased by 0.74 ± 0.18 °C during the 20th century. The increase in Earth's average temperature is called global warming. Based on measurements and studies of past climate (Joos et al., 1999), the observed temperature increase since the middle of the 20th century is caused by increasing carbon dioxide (CO_2) concentration, the main anthropogenic greenhouse gas (IPCC AR4, 2007).

Ice core data (EPICA, 2004), which provide a reliable and accurate record of CO_2 concentration going back hundreds of thousands of years (figure 1.1), show that the CO_2 concentration in the atmosphere was never even close to as high as it is at present; the current CO_2 concentration is above 380 ppm (parts-per-million), while the preindustrial level throughout the Holocene (the past 10,000 years) was close to 280 ppm (Denman et al., 2007).

Since the late 1950s when Charles D. Keeling began the first systematic monitoring of CO_2 concentrations at Mauna Loa, Hawaii, and at the South Pole (Keeling et al., 2005b), the annual mixing ratio of CO_2 is steadily increasing in the atmosphere and even accelerating (figure 1.2). The increasing concentration of CO_2 in the atmosphere comes primarily
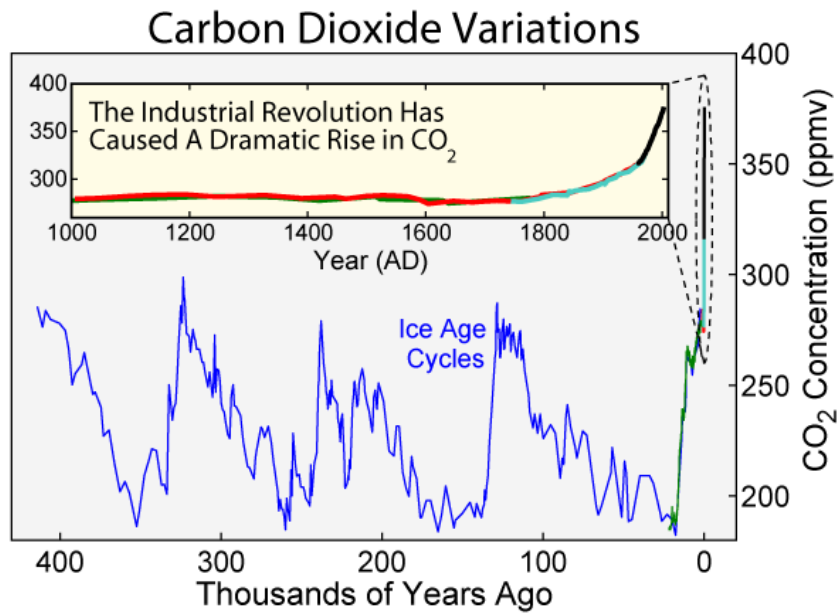
Figure 1.1— The variations in concentration of carbon dioxide (CO_2) in the atmosphere during the last 400 thousand years as measured from ice cores (EPICA, 2004) (Courtesy: Global Warming Art http://www.globalwarmingart.com).
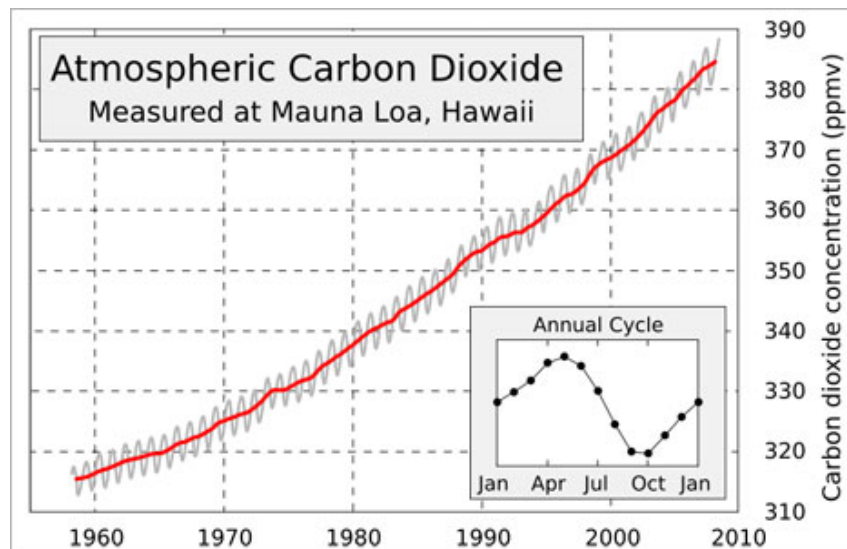
Figure 1.2— Recent Atmospheric CO_2 concentrations at Mauna Loa Observatory (Courtesy: Global Warming Art http://www.globalwarmingart.com).
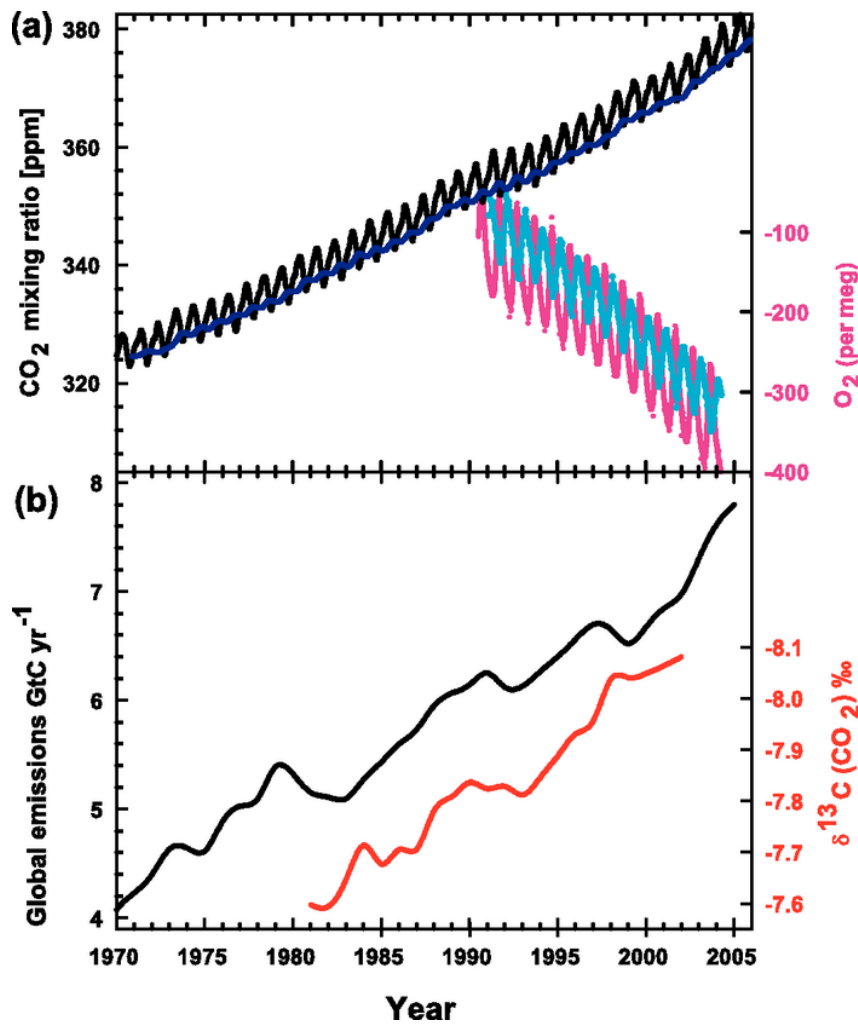
Figure 1.3— Recent CO_2 concentrations and emissions. (a) CO_2 concentrations (monthly averages) from Mauna Loa, Hawaii (black; (Keeling and Whorf, 2005)) and Baring Head, New Zealand (blue; (Manning et al., 1997)). In the lower right of the panel, atmospheric oxygen (O_2) measurements from flask samples are shown from Alert, Canada (pink) and Cape Grim, Australia (cyan) (Manning and Keeling, 2006). (b) Annual global CO_2 emissions from fossil fuel burning and cement manufacture in Gt C/year (gigatonnes of carbon = 1 billion tonnes = 1 Petagram = 1 x 10^{15} g) (black) through 2005, using data from the CDIAC website (Marland et al., 2006) to 2003. Annual averages of the ^{13}C/^{12}C ratio measured in atmospheric CO_2 at Mauna Loa from 1981 to 2002 (red) are also shown (Keeling et al., 2005a) (Courtesy:IPCC AR4 (2007)).

from anthropogenic (human) activities, particularly fossil fuel burning (i.e. combustion of coal, oil, natural gas), and changes in land use, such as the conversion of forests to agricultural lands (Houghton, 2003). These anthropogenic activities are transferring carbon from Earth's crust and living biomass into the atmosphere in the form of extra CO_2 superimposed on the natural fluxes of carbon in the Earth system.

There is much evidence confirming that anthropogenic emissions are the main cause for the observed increase in atmospheric CO_2. First, figure 1.1 shows that the timing of the increase is coincident with the rising emissions of carbon from fossil fuel combustion and land-use change starting with the industrial revolution. Second, the latitudinal gradient in CO_2 concentrations is highest at northern mid-latitudes and lower in the southern hemisphere, consistent with the fact that most of the emissions of fossil fuel are located in northern mid-latitudes. This latitudinal gradient has increased in proportion to emissions of carbon from fossil fuels (Keeling et al., 2005b). Third, the characteristic isotopic signatures of fossil fuel (its lack of ^{14}C, and depleted content of ^{13}C) leave their mark in the atmosphere. Fourth, atmospheric oxygen O_2 is declining at a rate comparable with fossil fuel emissions of CO_2 (combustion consumes O_2) (figure 1.3).

Therefore, understanding the global carbon cycle is necessary, particularly the response and feedback of carbon fluxes to climatic controls. In the following section an overview of the global carbon cycle including the main reservoirs of carbon will be presented. The main focus of this thesis will be on the processes that lead the land to be an important sink of carbon.

1.2 Overview of Global Carbon Cycle

The carbon cycle can be viewed as transfer of carbon between a set of reservoirs (figure 1.4). The major reservoirs (or pools) are the atmosphere, the terrestrial biosphere (including vegetation and non-living organic material, such as soil carbon), the ocean (including dissolved inorganic carbon (DIC) and living and non-living marine biota), the sediments (including fossil fuels), and the Earth's interior (i.e. the Earth's mantle and crust). Each of these reservoirs holds a form of carbon such as calcium carbonate in rocks or CO_2 and methane and other minor gases in the atmosphere. The exchange, or flux, of carbon among the atmosphere, oceans, and land surface is called the global carbon cycle (figure 1.4). The rate at which carbon moves between important reservoirs has been changed due to human actions. Burning fossil fuel speeds up the "weathering" of buried hydrocarbons and deforestation accelerates the natural pace at which forests die and decompose, releasing carbon back to the atmosphere.

According to IPCC AR4 (2007), about 80% of anthropogenic CO_2 emissions during the 1990s resulted from fossil fuel burning and cement production, and about 20% from land use change (primarily deforestation). Measurements of atmospheric carbon dioxide levels (going on since 1957) indicate that only about 45% of the combined anthropogenic CO_2 emissions accumulate in the atmosphere (Prentice, 2001) and show both a pronounced seasonality (Bolin and Keeling, 1963) and interannual variations associated with vegetation
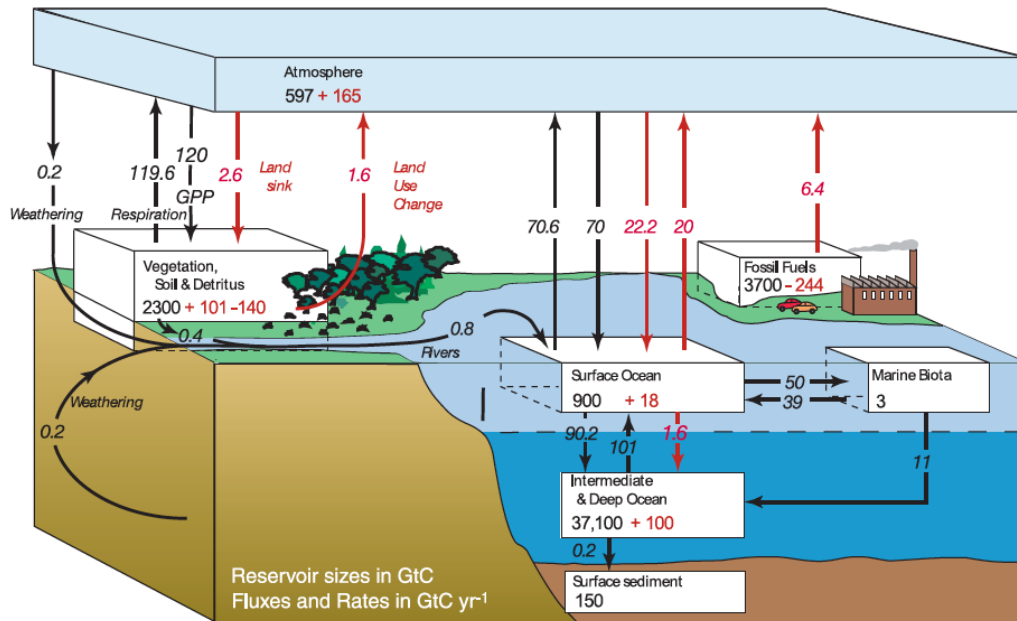
Figure 1.4— The global carbon cycle. In the figure the carbon fluxes are shown in Gt C/year with the natural fluxes depicted by black arrows and the anthropogenic fluxes by red arrows (Courtesy: IPCC AR4 (2007)). Units are in gigatonnes of carbon (1 Gt = 1 billion tonnes = 1 Petagram = 1 x 10^{15} g).

responses to climatic variations (Keeling et al., 1995; Francey et al., 1995). This suggests that the actual atmospheric CO_2 increase is significantly modified by ocean and land uptake of CO_2 (Prentice, 2001). Based on inorganic carbon measurements and a tracer-based separation technique, oceans are estimated to have taken up approximately 30% of the anthropogenic CO_2 emissions (fossil fuel plus land use) (Sabine et al., 2004) suggesting that the rest is taken up by the terrestrial biosphere (25%).

The global carbon budget has several terms that have a higher degree of certainty than others. For example, fossil fuel emissions, based on international energy statistics (Marland and Rotty, 1984; Andres et al., 1996), are probably the best-known term in the global carbon budget. Also, the partitioning of the net flux of carbon into the ocean and the terrestrial biosphere is well constrained by CO_2, O_2/N_2, and $\delta^{13}C$ measurements (Ciais et al., 1995; Francey et al., 1995; Keeling et al., 1993, 1995; Battle et al., 2000; Piper et al., 2001). In addition, the uptake of carbon by oceans has been estimated by a number of different ocean models, which generally agree with the observation-based budget estimates (Gloor et al., 2003; Mikaloff Fletcher et al., 2006; Sabine et al., 2004; Manning and Keeling, 2006). Nevertheless, the most uncertain aspect of the anthropogenic global carbon

budget is the breakdown of the terrestrial sources (from land use) and terrestrial sinks or the so-called "residual land sink" which is part of the global carbon cycle calculation once the other components are accounted for (fossil fuel emissions, land-use emissions, atmospheric increase, and ocean uptake). For example, for the decade of 2000s, fossil fuel emissions account for 7.7 ± 0.5 PgC/year (Petagram=10^{15} g), land use change is 1.1 ± 0.7 PgC/year, oceans take up 2.3 ± 0.4 PgC/year and 4.1 ± 0.1 PgC/year remains in the atmosphere (Global Carbon Project: http://www.globalcarbonproject.org/, updated from Le Quéré et al. (2009)). The land sink is calculated as the residual of the sum of all sources minus the sum of atmosphere and ocean sinks and accounts for 2.4 PgC/year.

To understand the role of the terrestrial biosphere in the global carbon cycle, it is important that we understand the processes that transfer carbon between the atmosphere and terrestrial biosphere reservoirs. Understanding the underlying processes may help to predict their behavior in the future and predict if the terrestrial biosphere will continue to store a substantial fraction of the carbon dioxide that human are producing or if it will stop or even reverse and accelerate the atmospheric increase.

1.3   Terrestrial biosphere carbon cycle processes

There are several processes that exchange carbon between the terrestrial biosphere and the atmosphere. Carbon exists in the atmosphere as the compound CO_2, methane (CH_4) and other minor gases. It first enters the terrestrial biosphere when plants absorb CO_2 through tiny pores in their leaves. The plants then capture CO_2 and convert it into simple organic compounds like glucose through the biochemical process known as "photosynthesis". During photosynthesis, plants use energy from sunlight to combine CO_2 from the atmosphere with water from the soil to create carbohydrates (carbo- and hydrate, signify carbon and water) to grow and to reproduce. Current estimates suggest that global photosynthesis removes about 120 PgC/year from the atmosphere (IPCC AR4, 2007) (see figure 1.4).

Plants also release CO_2 back to the atmosphere through the process of respiration, known as Autotrophic Respiration (Ra). Respiration is the process in which oxygen is used to break down organic compounds, namely carbohydrates made during photosynthesis, into CO_2 and water (H_2O). The CO_2 is released back to the atmosphere, ready to be recycled again. Plant respiration represents approximately half (60 PgC/year) of the CO_2 that is returned to the atmosphere in the terrestrial portion of the carbon cycle (IPCC AR4, 2007).

Soil respiration, known as Heterotrophic Respiration (Rh), is another process and considered one of the largest sources by which carbon is returned to the atmosphere as CO_2. The

release of CO_2 through respiration is not unique to plants, but is something all organisms do. When dead organic matter is broken down or decomposed (consumed by bacteria and fungi), CO_2 is released into the atmosphere at an average rate of about 60 PgC/year globally (IPCC AR4, 2007).

Fire and human land use practices (Houghton, 2003) also play an important role in the transfer of carbon dioxide from the land to the atmosphere. For example, fires consume biomass and organic matter to produce carbon dioxide, methane, carbon monoxide, and smoke, and the vegetation that is killed but not consumed by the fire decomposes over time adding further carbon dioxide to the atmosphere. Also, when forests are cleared for agriculture the carbon contained in the living material and soil is released. In contrast, when forests are allowed to re-grow, carbon is stored in the accumulating living biomass and soils.

The carbon balance of an ecosystem at any point in time is the difference between its carbon gains through photosynthesis and losses through respiration by autotrophs (plants and photosynthetic bacteria) and heterotrophs (fungi, animals and some bacteria). The balance of CO2-assimilation and all respiratory processes is defined as Net Ecosystem Productivity (NEP). However, besides respiratory losses, there are carbon losses through fire, harvest and grazing. Based on that, the total carbon balance, including respiratory and non-respiratory losses, is termed Net Biome Productivity (NBP) (Schulze and Heimann, 1998; Schulze et al., 2000).

The previous definitions can be summarized in the following terminologies

- **Gross Primary Production (GPP):** the total amount of carbon fixed by photosynthesis in an ecosystem. The total global GPP estimate is about 120 PgC/year (IPCC AR4, 2007).

- **Ecosystem Respiration (R_{eco}):** the total respiration of plants, animals, and microbes (autotrophic and heterotrophic respiration).

$$R_{eco} = Ra + Rh \qquad (1.1)$$

- **Net Primary Production (NPP):** the net production of organic carbon by plants in an ecosystem; equals GPP minus the amount of carbon consumed by plants in autotrophic respiration (Ra). The total global NPP estimate is about 60 PgC/year (IPCC AR4, 2007).

$$NPP = GPP - Ra \qquad (1.2)$$

- **Net Ecosystem Production (NEP):** the difference between NPP and heterotrophic respiration (Rh), which determines the amount of carbon lost or gained by the ecosystem without disturbances, such as harvests and fire.

$$NEP = NPP - Rh = GPP - (Ra + Rh) = GPP - R_{eco} \qquad (1.3)$$

- **Net Ecosystem Exchange (NEE):** is fairly similar to NEP and determines the amount of CO_2 entering an ecosystem and the amount of carbon being lost through respiration simultaneously.

$$NEE = -NEP = R_{eco} - GPP \qquad (1.4)$$

- **Net Biome Production (NBP):** the carbon accumulated by the terrestrial biosphere when carbon losses from non-respiratory processes (fires, harvests) are taken into account.

$$NBP = NEP - (\mathrm{non-respiratory\ fluxes}) \qquad (1.5)$$

When photosynthesis is larger than the sum of plant respiration, soil respiration, fire, and land use releases, there is a net sink of carbon from the atmosphere to the terrestrial biosphere. There is a net source of carbon from the ecosystem to the atmosphere when the photosynthesis is less than the sum of the other terms. The gain and loss of carbon in the terrestrial biosphere on seasonal time scales is clear from subtle changes in atmospheric CO_2 measurements (Bolin and Keeling, 1963). On longer timescales from decades to centuries, the amount of carbon stored in the terrestrial biosphere is the result of the balance between NPP and carbon losses through respiration, land use, fire, and other disturbance.

Many studies have been carried out to quantify the residual land sink. But which processes dominate, or in what regions of the Earth this carbon sinks occurs are still open questions. A major source of uncertainty in quantifying the carbon uptake by the terrestrial biosphere is the limited understanding of the mechanisms driving carbon sources and sinks, given the great heterogeneity of vegetation and soils. Several scenarios could cause the land to take up more CO_2 than is released each year. For example re-growth of forests on previously deforested land (Dixon et al., 1994; Schimel et al., 2001; Houghton, 2003) could account for some of the missing carbon. However, the contributions of land cover and/or land use changes to regional and global carbon budgets, are highly uncertain and remains problematic (Houghton et al., 1999).

To determine the possible mechanisms behind terrestrial carbon sources and sinks, different modeling tools and datasets are used on different spatial and temporal scales. The main methods, which are used to quantify regional and global carbon budgets, are briefly summarized in the following section.

1.4 Methods of estimating terrestrial carbon fluxes

Here we review some of the main methods used to determine the size and the geographical locations of terrestrial carbon.

1.4.1 Measurements

1.4.1.1 Forest inventory

Forests sequester and store more carbon than any other terrestrial ecosystem. The carbon stored in the aboveground living biomass of trees is typically the largest pool and the most directly impacted by deforestation and degradation. Thus, estimating aboveground forest biomass carbon is a critical step in quantifying carbon stocks and fluxes from forests. Ground-based measurements of tree height and diameters at breast height (DBH) can be combined using allometric relationships to estimate forest carbon stocks. Allometric equations statistically relate these measured forest attributes to destructive harvest measurements (e.g. Brown (1997); Keller et al. (2001)).

These measurements can be spatially aggregated to estimate the regional fluxes (Dixon et al., 1994; Goodale et al., 2002). The main disadvantage of inventory-based methods is that most of the inventories have been carried out in forested ecosystems limited to the aboveground biomass with limited consideration of belowground processes and non-forested ecosystems.

Many countries, mainly tropical countries, already carry out regular measurement of terrestrial carbon stocks on sub-national and national scales for policy development and planning. Then, several organizations and research groups collect these data and combine them in order to estimate spatial pattern of carbon fluxes. For example, FAO (Food and Agriculture Organization of the United Nations) has been compiling forest inventories since 1946, providing detailed data on carbon stocks. Also, they calculated the impacts of forest changes on carbon flux in the temperate and boreal forest (UN-ECE/FAO, 2000). A further source of inventory data comes from the United Nations Framework Convention on Climate Change (UNFCCC, 2000). In parallel to these inventories, different forest biomass inventories (Fang et al., 2001; Goodale et al., 2002; Nabuurs et al., 2003; Shvidenko and Nilsson, 2003) and soil carbon inventories combined with models (Ogle, 2003; Bellamy et al., 2005; van Wesemael et al., 2005; Falloon et al., 2006) are compiled for different

regions to calculate the changes in carbon stocks from which fluxes can be calculated.

1.4.1.2 Eddy flux measurements

The eddy covariance technique is used to measure vertical turbulent fluxes of energy, water vapor, carbon dioxide, methane, and various other gases within the atmospheric boundary layer. It provides an accurate way to measure surface-to-atmosphere fluxes. The basic idea behind the eddy covariance method is simple. Airflow can be imagined as a horizontal flow of numerous rotating eddies with each eddy having horizontal and vertical components. The turbulent eddies transport matter and energy vertically within the atmospheric boundary layer. Measurements are made such that the vertical wind speed w and a scalar such as concentration c are measured from a few to several tens of meters above the ground. The measured variables are divided into an average and a fluctuating component (denoted with a bar and a prime, respectively (Seinfeld and Pandis, 1998):

$$w = \bar{w} + w' \tag{1.6}$$

$$c = \bar{c} + c' \tag{1.7}$$

In very simple terms, the covariance between the fluctuating components is the eddy flux (F_E) of the desired substance:

$$F_E = \overline{w'c'} \tag{1.8}$$

The eddy covariance technique is a unique data source for measuring Net Ecosystem Exchange (NEE), Latent Heat flux (LH), and sensible heat flux (H) with high temporal resolution (less than 1 hour) over a small region (1 km^2). At present over 500 flux sites have been established around the world and operated on a long-term and continuous basis (Baldocchi and Wilson, 2001). Eddy flux measurements are useful to obtain terrestrial fluxes at local scales. However, missing or rejected data in these measurements due to equipment failures, maintenance and calibration, errors or spikes in the raw data when turbulence is low, and also due to physical and biological constraints (e.g. storms, and non-optimal wind directions) are a vital problem of the approach. Overall, about 17-50% of the observations are reported as missing or rejected at FluxNet (a network of regional networks coordinating regional and global analysis of observations from flux sites) (Falge et al., 2001).

To accurately calculate annual values of NEE and energy fluxes the gaps in the records have to be filled. Several gap-filling methods exist (e.g. Greco and Baldocchi (1996); Jarvis et al. (1997); Falge et al. (2001); Barr et al. (2004); Braswell et al. (2005); Desai

et al. (2005); Papale and Valentini (2003); Reichstein et al. (2005); Monson et al. (2002); Hui et al. (2004); Aubinet et al. (1999)) using various approaches, including interpolation and extrapolation, probabilistic filling, look-up tables, regression analysis, artificial neural networks, and process-based models operated in data-assimilation mode.

In order to generate spatial flux maps from point data, several studies have attempted to scale up fluxes at sites to regions, known as "up-scaling". Up-scaling exercises of eddy covariance based carbon fluxes to large regions has been conducted for the US (Xiao et al., 2008; Yang et al., 2007), for Europe (Jung et al., 2008; Papale and Valentini, 2003; Vetter et al., 2008), and for the globe (Jung et al., 2009). However, given the heterogeneity of land, the coverage and accuracy of the measurements are not sufficient for obtaining confidence in the large-scale flux estimates derived through up-scaling approaches.

Further information about eddy covariance methods, tower locations, site characteristics as well as data availability can be found at the FluxNet website (http://www.fluxnet.ornl.gov).

1.4.2 Modeling

Direct measurements of carbon fluxes using inventory or eddy covariance methods are an essential approach to measure and monitor carbon fluxes at local scales with high temporal resolution. However, there are many regions of the globe, the tropics in particular, where measurements are incomplete or entirely lacking. Thus, there are some difficulties to scale up these measurements to regional and also to longer time-scales (decadal). Therefore, numerical modeling approaches have been developed to quantify magnitude and geographical distribution of sources and sinks of carbon at regional and global scales.

Hereafter, two different modeling approaches, so-called bottom-up and top-down models, are summarized.

1.4.2.1 Bottom-up approach

Under this modeling scheme, models range in complexity from simple regression "statistical" models to more complex process-based models. The simple statistical biosphere models are mainly based on empirical relations between one or more estimates of biological processes (e.g. soil respiration) and important climatic variables (e.g. temperature, precipitation) (e.g. Raich and Schlesinger (1992); Lloyd and Taylor (1994); Reichstein et al. (2003, 2005)) (see chapter 2). On the other hand, the process-based models integrate knowledge of physiological and ecological processes to model the response of the system to environmental changes (Cramer et al., 2001; Schimel et al., 2000; McGuire et al., 2001). The process-based models have the advantage of being able to describe the mechanisms of

how and why the distributions of sources and sinks are changing. However, these complex models include representations of processes affecting the terrestrial carbon fluxes, which are based on only limited understanding of these processes. Therefore, it is expected that some of the processes will be simplified or inadequately represented, and some important processes will not be included in the models. As a result, different models, using different simplified assumptions, will produce different estimates of sources and sinks of carbon. Moreover, these models are driven by various data (e.g. meteorological fields, atmospheric CO_2 observations, land cover maps, etc.), and hence any errors in the input data may lead to incorrect flux estimates. Furthermore, validation and verification of these models is difficult on a large scale due to difficulties in scaling up small-scale measurements as mentioned in the pervious section.

Several ecosystem process-based models have been developed in order to estimate and to predict the terrestrial carbon fluxes. The Carnegie-Ames-Stanford Approach model (CASA) (Potter et al., 1993), the Terrestrial Observation and Prediction System model (TOPS) (Nemani et al., 2003), the Lund- Potsdam-Jena model (LPJ) (Sitch et al., 2003), LPJ - Dynamic Global Vegetation Model (LPJ-DGVM) (Haxeltine and Prentice, 1996; Kaplan et al., 2003; Prentice et al., 1992), BioGeochemical Cycles model (BIOME-BGC) (Thornton et al., 2005), and ORganizing Carbon and Hydrology In Dynamic EcosystEms model (ORCHIDEE) (Krinner et al., 2005) are examples of process-based terrestrial carbon cycle models. These models have been applied and tested in various studies (Churkina and Running, 1998; Churkina et al., 2003; Kimball et al., 2000; Vetter et al., 2005; Brovkin et al., 2004; Sitch et al., 2005).

Among other related studies, the Carbon Cycle Model Linkages Project CCMLP (McGuire et al., 2001) has carried out a comprehensive study investigating the role of the terrestrial biosphere in the Earth system by comparing four global terrestrial biosphere models. CCMLP used four different process-based terrestrial ecosystem models driven by a combination of historical climate, CO_2 and the historical land use data from Ramankutty and Foley (1999). This study showed that there were substantial differences in the magnitude of interannual variability simulated by the models. The models also varied considerably in their ability to simulate the observed changing amplitude of the seasonal cycle of atmospheric CO_2.

1.4.2.2 Top-down approach

After the first systematic measurements of CO_2 concentrations at Mauna Loa, Hawaii, and at the South Pole by Charles D. Keeling in the late 1950s, a global observational network measuring atmospheric CO_2 among other trace gases has been implemented since

the 1980s. This is in order to provide an improved spatial and temporal structure of the global-scale atmospheric CO_2 concentration. Although there are only 100 sampling sites, at which global observational networks provide concentration measurements of atmospheric CO_2, they accurately measure gradients in CO_2 concentration between two different points of the globe. This reflects the distribution of the surface fluxes dispersed by the atmosphere's transport (Keeling et al., 1989; Tans et al., 1990). Since atmospheric tracer transport is linear, a model of atmospheric transport can be used in an "inverse" mode to estimate carbon sources and sinks from observed concentrations. The transport model simulates how the atmospheric circulation moves the trace gas by advection, diffusion and convection. The inversion of the atmospheric transport model is commonly referred to as the top-down approach.

Due to the small number of the observing stations, the inverse problem is highly underdetermined which means there are many flux fields yielding the same modeled concentrations at the observational sites (Kaminski and Heimann, 2001). In other words, the inferred fluxes are poorly constrained by the observations. In order to handle the underdetermined problem, different approaches have been used. As one solution, the number of the sources and sinks (unknowns) has to be reduced so that the total number of observations is greater than the number of fluxes to be estimated. This can be achieved by identifying fluxes at continental or ocean basin scales by dividing the globe into large regions (Tans et al., 1990; Brown, 1993; Ciais et al., 1995). As another solution, a-priori information of regional land and ocean fluxes (e.g. direct flux measurements, or modeled fluxes) and their plausible uncertainty ranges can be included to constrain the results using a classical Bayesian approach (Tarantola, 1987; Enting, 1993). These approaches have been described in more details by Kaminski and Heimann (2001).

In the last two decades, a number of atmospheric inversion experiments have been performed in an effort to quantify CO_2 sources and sinks at a variety of spatial and temporal scales. First inversion studies attempted to estimate the long-term mean fluxes at continental or ocean basin scales. In these studies (defined as synthesis inversions) the globe has been divided into a few large regions in which flux patterns are prescribed and all grid cells are adjusted by a single scaling factor (Enting et al., 1995; Ciais et al., 1995; Rayner et al., 1999; Bousquet et al., 2000; Peylin et al., 2002). The advantage of that approach is that the inversion problem becomes over-determined. Therefore even if the observation network samples only part of a region, all points in the region are constrained. The disadvantage is that variations of fluxes at scales smaller than the selected regions cannot be estimated. Also, aggregation errors can occur when incorrectly prescribed flux patterns are assigned within regions (Kaminski and Heimann, 2001). Most recent studies attempt

to infer fluxes at the resolution of the underlying transport model (defined as adjoint inversions) (Kaminski and Heimann, 2001; Rödenbeck et al., 2003) using a Bayesian framework to include additional a-priori information into the solution to constrain the flux estimates. After the optimization processes, the fluxes are usually aggregated together into larger regions.

In most of the adjoint inversion studies, the uncertainties of the a-priori information are fully uncorrelated between grid cells (Kaminski et al., 1999; Houweling et al., 1999). This is opposite to large-scale studies (synthesis inversions) that assume fluxes are fully correlated over a region. In Rödenbeck et al. (2003), spatio-temporal correlations between fluxes are introduced to avoid the "spatial rectification biases". Overall, significant differences in the results among these models are shown, in particular when fluxes are partitioned regionally. This is because of the different inversion methods, setups, and transport models used by each group (Peylin et al., 2002).

To quantify and diagnose the main sources of uncertainty in atmospheric CO_2 inversion studies and also to have a better view of net carbon uptake in the land and oceans, the Atmospheric Tracer Transport Model Inter-comparison Project (TransCom) was established in the 1990s. The most recent phase of this experiment is the TransCom3 in which the forward CO_2 sensitivities from different modeling groups are collected to explore the uncertainties arising in the inversion process from the transport, the data and the inversion set-up itself (Gurney et al., 2002, 2003, 2004; Baker et al., 2006). In addition, different sensitivity studies have been performed to investigate different aspects of the TransCom atmospheric inversion (e.g. using different CO_2 and fossil fuel CO_2 data uncertainties, or using different observing networks) (Law et al., 2003; Gurney et al., 2005; Patra and Maksyutov, 2003; Patra et al., 2006).

The most important finding of TransCom3 is that the transport model is one of the main contributors to the inversion uncertainty. Furthermore, incorrect spatial and temporal patterns in the prescribed fluxes will result in errors in the estimated fluxes. Also, many of the regional flux estimates for individual models were the result of strong responses at particular stations or subtle tradeoffs and compensation among regions. These findings point to some important technical difficulties; first, atmospheric transport models are not perfect; second, the observational network is sparse, in particular in the tropics; third, individual measurements are usually not representative of the appropriate temporal and spatial scale of the transport model.

Commonly, the resolution of atmospheric transport models used in the inversion studies is on the order of $2°$ latitude $\times$ $2°$ longitude or coarser. On the other hand, both the

surface fluxes and atmospheric transport over land have substantial small-scale variability. Ignoring such important variability introduce large errors in the flux estimates (Gerbig et al., 2003a,b; van der Molen and Dolman, 2007; Pérez-Landa et al., 2007; Ahmadov et al., 2007). Some recent studies have been conducted to solve this problem using "zoomed" atmospheric transport models (Peylin et al., 2005) or using nested models (Peters et al., 2007). A recent study by Rödenbeck et al. (2009) used a two-step scheme that uses global and regional models sequentially in separate inversion steps.

In general, atmospheric CO_2 inversion approaches have the attraction that they estimate the total net flux generated by the sum of all mechanisms (natural and anthropogenic) giving estimates of the location and magnitude based on the atmospheric measurements of CO_2. However, they provide little or no information about the underlying processes responsible for the estimated fluxes. Hence, they cannot be used to understand or predict the future behavior of the carbon cycle.

1.5 Problem statement

In the previous section, the advantages and the disadvantages of different methods used to estimate terrestrial carbon fluxes are summarized. For example, direct measurement of carbon sources and sinks (inventory or eddy covariance data) has the disadvantage that the coverage and accuracy of the measurements are not sufficient for obtaining confidence in the large-scale flux estimates. From a modeling point of view, terrestrial biosphere models are useful tools for exploring the processes involved in the uptake and release of carbon in the terrestrial system and are in theory able to project future fluxes. However, the validation of these models on the global scale is difficult. Also, the inverse model (relating concentrations to fluxes by an atmospheric transport model) is a powerful tool to quantify carbon fluxes over large regions but does not provide any information about the underlying processes and cannot make future projections.

In light of the above, it is clear that there is an urgent need to combine the different modeling approaches (bottom-up "terrestrial biosphere models" and top-down "inverse models") to understand and quantify carbon sources and sinks in a "multiple constraint" approach. As a benefit, the bottom-up approach can be validated on a global scale using atmospheric measurements of CO_2 which integrate the CO_2 signal over large areas. Also, optimizing some key parameters in the biosphere model with respect to the atmospheric CO_2 measurements can achieve more understanding about the underlying processes controlling the fluxes.

Some progress has been made in the direction of tuning or optimizing parameters in terrestrial biosphere models in order to fit the atmospheric measurements of CO_2. For

example, Fung et al. (1987) used the annual cycle of atmospheric CO_2 observations to test their model for estimating the exchange of CO_2 between the terrestrial biosphere and the atmosphere from satellite data and field measurements. A similar study by Knorr and Heimann (1995) has been performed to optimize some key parameters in a simple diagnostic biosphere model (SDBM) with respect to the seasonal cycle of atmospheric CO_2 measurements. In these two studies, the parameters were adjusted manually until they got a reasonable fit with atmospheric CO_2 measurements. Later, Kaminski et al. (2002) introduced a systematic method for optimizing parameters following a similar systematic approach introduced by Enting et al. (1995) in which the uncertainty of the flux magnitude can be calculated. In this study, they optimized the controlling parameters of the SDBM (Knorr and Heimann, 1995) with respect to the seasonal cycle of atmospheric CO_2 concentrations using a variational data assimilation approach. They also estimated an uncertainty range for the optimized parameters. These optimized parameters are then used to run the model to predict some diagnostic quantities of interest such as net fluxes and net primary productivity (NPP).

These studies are purely diagnostic so that they cannot be used to make prediction of the future carbon sources and sinks. This leads to another approach that combines different data constraints (e.g. satellite data, CO_2 measurements) in a more mechanistic model and allows a prediction of some of the behavior of the terrestrial biosphere. That approach is usually known as data assimilation. Scholze et al. (2003) and Rayner et al. (2005) presented a Carbon Cycle Data Assimilation System (CCDAS), in which they use a more comprehensive, prognostic terrestrial biosphere model, the Biosphere Energy Transfer Hydrology Scheme (BETHY) (Knorr and Heimann, 2001). CCDAS is capable of assimilating both remote sensing data as well as atmospheric CO_2 concentration measurements into a process-based model of the terrestrial biosphere (Scholze et al., 2003) in order to (1) calibrate the model parameters, (2) derive terrestrial CO_2 fluxes consistent with the atmospheric observations, and (3) present uncertainties on both model parameters and derived quantities such as fluxes.

1.6   Objectives of this thesis

Here, we attempt to follow the same path of the data assimilation method discussed in the previous section, assimilating atmospheric concentration data into a terrestrial biosphere model but using a simple diagnostic approach. Therefore, within this thesis, we developed a modeling framework that couples bottom-up and top-down approaches and uses different data constraints (atmospheric CO_2 concentrations, satellite-derived data, and climate data) in order to quantify the carbon sources and sinks of the terrestrial

biosphere and to understand the underlying processes by optimizing some internal key parameters of the biosphere model (the bottom-up approach) in order to fit the observed CO_2 concentrations. Our modeling framework has drawn upon certain techniques from previous modeling approaches while including new features (see next section).

Also, as an objective, the following scientific questions will be addressed

- What is the role of the climatic drivers (e.g. precipitation, temperature, radiation) on the interannual variability of the estimated fluxes?

- Similarly, what is the role of different land processes (e.g. respiration, photosynthesis, fire) on the interannual variability of the estimated fluxes?

- Can we improve CO_2 flux estimates by such a coupling?

1.7 Methodology

Since this approach is not new, we follow the methodology of Kaminski et al. (2002) (see section 1.5) but using a different model algorithm for the biosphere model as well as for the inverse model. First, we implemented a Simple Diagnostic Photosynthesis and Respiration Model (SDPRM) based on pre-existing formulations. The ecosystem respiration model is based on formulations introduced by Lloyd and Taylor (1994), Raich et al. (2002) and the modification made by Reichstein et al. (2003). The photosynthesis model is based on the light use efficiency logic presented by Monteith (1977) of calculating the Gross Primary Production (GPP). The SDPRM is driven by remote sensing and climate data. Second, for the inverse model, we used the inversion algorithm presented in Rödenbeck (2005), hereafter referred to as the Standard Inversion (STD-inv).

The SDPRM model was then coupled to the STD-inv (hereafter referred to as SDPRM-inv) by replacing the simple statistical linear flux model of the STD-inv (described in chapter 3). This was done for two reasons: first, to provide a reliable a-priori CO_2 fluxes with high spatio-temporal resolution to the STD-inv so small-scale forcing can transported to the atmospheric information, second, to optimize some internal (physiological & interpretable) parameters of the SDPRM in order to fit the atmospheric measurements of CO_2.

To couple the SDPRM model to the inverse model, it has been linearized in the adjustable parameters in order for the quick minimization algorithm in the inverse model to work. This is one of the difference between the modeling framework used here and the CCDAS introduced by Rayner et al. (2005) (see section 1.5). In CCDAS, they used a process-based model (BETHY) (Knorr and Heimann, 2001) which is more complicated than the

SDPRM. Thus, as the process models tend not to be linear, the minimization algorithm in the CCDAS is a more involved process.

The model framework is schematically shown in figure 1.5 representing different input data and calculation steps. Starting from the input data, there is first the satellite data (Normalized Difference Vegetation Index (NDVI)) that is used to calculate the fraction of Absorbed Photosynthetically Active Radiation (fAPAR). Besides the satellite-based input data, there is the climate data taken from the National Center for Environmental Prediction/National Center for Atmospheric Research Reanalysis (NCEP/NCAR) (Kalnay et al., 1996). Both fAPAR and the climate data are interpolated and mapped to the resolution $4°$ latitude $\times$ $5°$ longitude. The SDPRM produces a space-time distribution of modeled Gross Primary Production (GPP), Ecosystem Respiration R_{eco}, and Net-ecosystem Exchange (NEE$= R_{eco}$-GPP) (more details in chapter 2).

The next step is to use GPP and R_{eco} as a-priori fluxes with some linearized terms in the inversion calculation algorithm (more details in chapter 3). NEE is only one component of the atmospheric carbon budget. Therefore, some other flux components (fossil fuel emission and ocean-atmosphere carbon fluxes) need to be included in the inversion calculation (see chapter 3). The main input to the atmospheric inversion is the atmospheric CO_2 measurements. Finally, the inverse model produces, among other things, a space-time distribution of modeled fluxes inferred from the atmospheric CO_2 measurements. The optimized parameters in the SDPRM models are one of the important outputs of the coupled system SDPRM-inv that can improve our understanding of the ecosystem behavior.

1.8   Thesis outline

The thesis is comprised of a total of 4 chapters:

Chapter 2 is devoted to the description of the empirical equations of the Simple Diagnostic Photosynthesis and Respiration Model (SDPRM). To test the performance of the model, the output is compared with results of two different approaches (process-based model and atmospheric inverse model). Furthermore, the sensitivity of the estimated fluxes to the driving forces based on different analyses is presented. Finally, a brief conclusion is given at the end of the chapter.

Chapter 3 describes the inverse model algorithm and the implementation details of the coupled system SDPRM-inv. The results of the coupled system are analyzed and presented. The time series of the estimated fluxes as well as their annual mean for different regions of the globe are shown. In addition, the optimized parameters of the biosphere model and their uncertainties compared to their initial values, along

with the a-posteriori correlation matrix, are presented and discussed. After that, some examples of the fit to the concentration data used in the calculations are shown. Finally, we show the estimated annual mean of GPP for different biomes and compare it with the results of Beer et al. (2010) . A brief conclusion is given at the end of the chapter.

Chapter 4 contains the main conclusions of this work and the outlook.
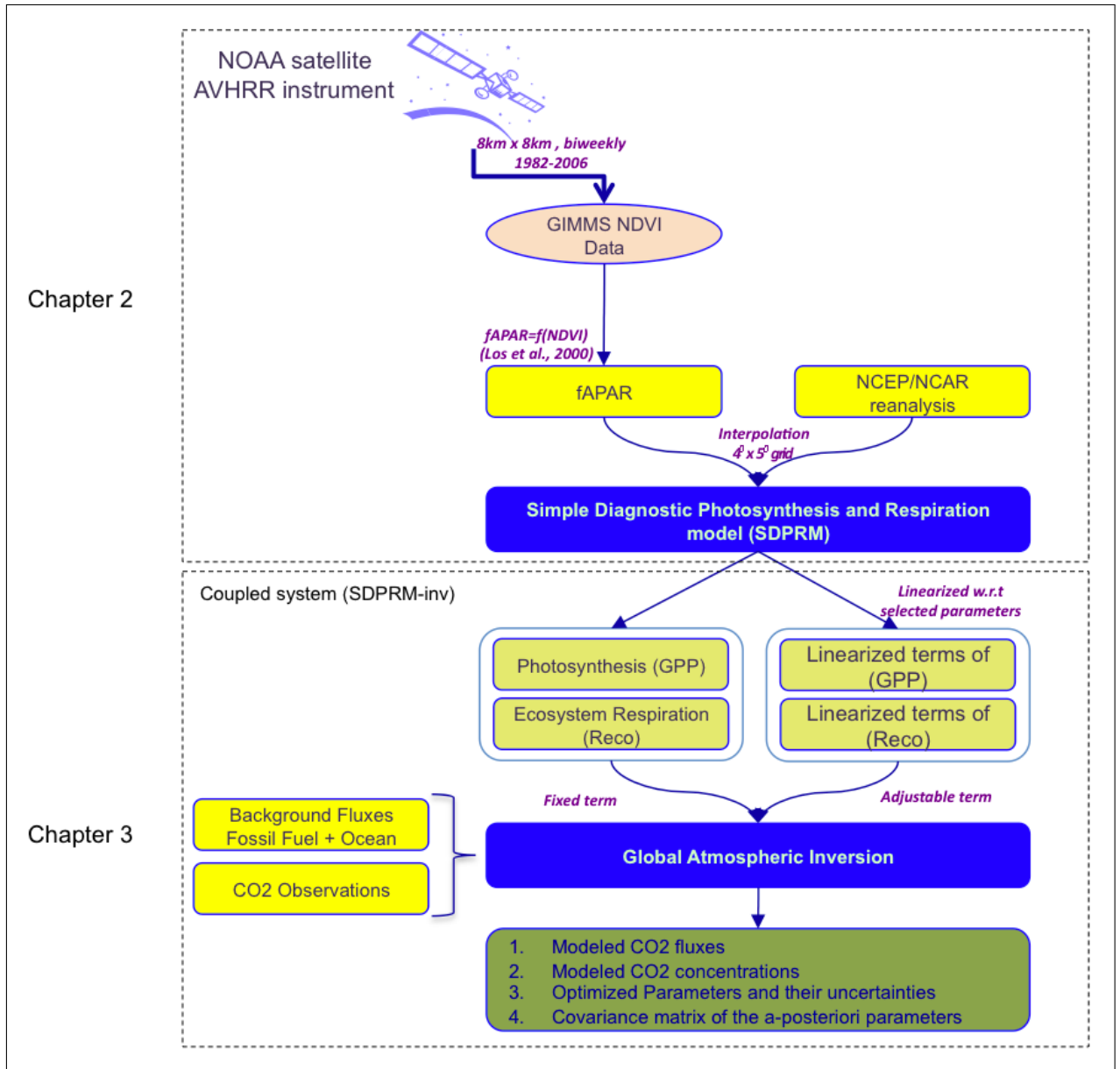
Figure 1.5— Model framework

Chapter 2

Simple Diagnostic Photosynthesis and Respiration Model (SDPRM)

Here, we describe the empirical equations of the Simple Diagnostic Photosynthesis and Respiration Model (SDPRM). In order to test the performance of the model, the results of the model are demonstrated and compared with some other modeling approaches. In addition, various sensitivity analyses are carried out in order to quantify the role of the climate controls on the estimated fluxes of GPP and R_{eco}. The results of these analyses are presented along with concluding remarks.

2.1   Introduction

Several methods are used to quantify the size and the geographical locations of terrestrial carbon sources and sinks at regional and continental scales. One of these methods is the direct measurement of carbon fluxes (e.g. eddy covariance data). Unfortunately, there are many regions of the globe, in particular the tropics, where measurements are incomplete or entirely lacking. Therefore, difficulties arise when scaling up these measurements to regional and global scales. Thus, estimates of CO_2 fluxes at regional and continental scales require the integration of remote sensing and climate data with field measurements and experimental manipulations (Running, 1999).

In principle, biosphere-atmosphere carbon exchange, generally referred to as the Net Ecosystem Exchange of CO_2 (NEE), can be approximated as the balance between CO_2 uptake through Gross Primary Production (GPP), the photosynthetic uptake of carbon by plants, and CO_2 emission through plant and soil respiration, generally referred to as Ecosystem Respiration (R_{eco}) (see chapter 1, section 1.3). Many diurnal and seasonal patterns of atmospheric CO_2 concentration are dominated by only these two processes (GPP,

R_{eco}) (Denning et al., 1996; Heimann et al., 1998). However, additional processes including fire, dissolved organic carbon (DOC) and dissolved inorganic carbon (DIC) losses in rivers, erosion, and land use changes need to be considered when the interannual and decadal dynamics in atmospheric CO_2 are analyzed (Canadell et al., 2000; Pacala et al., 2001). As the Earth system is regulated by several complex physical, biological, and chemical processes, the challenge lies in implementing simple models that use few variables and parameters (easy to be changed and modified) and are robust across the time scales of interest.

Here, we present a Simple Diagnostic Photosynthesis and Respiration Model (SDPRM) which is implemented based on pre-existing formulations (see section 2.3 and 2.4). The model estimates 3-hourly values of Ecosystem Respiration (R_{eco}) and daily values of Gross Primary Production (GPP). The model is driven by meteorology and remote sensing data, and uses some adjustable parameters. The motivation is to provide reliable first-guess fields of surface CO_2 fluxes, with fine temporal and spatial scales, for applications in inverse models. The model will replace the simple statistical flux representation of the standard inversion (STD-inv) (Rödenbeck, 2005) (see chapter 3) to adjust some selected parameters of the model in order to fit the observed CO_2 concentrations.

The algorithm of SDPRM and the data used are described in the following sections.

2.2   Data

2.2.1   GIMMS NDVI

Usually, terrestrial biosphere models require a set of land-surface biophysical parameters that control the exchange of energy, mass (e.g. water and CO_2) and momentum between the Earth's surface and the atmosphere (e.g. land cover classification, Leaf Area Index (LAI), fraction of Absorbed Photosynthetically Active Radiation (fAPAR)). The estimation of land surface parameters at a global scale, especially with regional scale detail, is, to some extent, only feasible through remote sensing. The estimations of these key variables are based on the spectral properties of vegetation; vegetation strongly absorbs visible light, using the energy for photosynthesis, and strongly reflects near-infrared radiation. Based on this fact, the Normalized Difference Vegetation Index (NDVI) (Tucker, 1979) is expressed as:

$$NDVI = \frac{\rho_{nir} - \rho_{red}}{\rho_{nir} + \rho_{red}} \qquad (2.1)$$

where ρ_{red} and ρ_{nir} stand for the spectral reflectance measurements acquired in the visible and near-infrared bands, respectively. The possible range of NDVI values is between -1 and 1, and the number is unitless. However, no green leaves give a value close to zero. A zero means no vegetation and close to +1 (0.8 - 0.9) indicates the highest possible density of green leaves. Soil and rock will have values that are close to zero while the differential for water bodies such as rivers will have negative values. Also, clouds and snow will have negative NDVI values.

Researchers have established quantitative relations between NDVI and biophysical variables controlling vegetation productivity and land-atmosphere fluxes (Sellers, 1985; Nemani and Running, 1989). For example, it is found that changes in NDVI time series indicate changes in vegetation conditions proportional to the fAPAR (Sellers, 1985). That led to the current generation of ecosystem models that use satellite-based vegetation indices for simulating carbon, energy, and water fluxes in response to climate variability and ecosystem disturbance (Randerson et al., 1996; Sellers et al., 1996b; Kaminski et al., 2002; van der Werf et al., 2004; Zhao and Running, 2010).

SDPRM requires two (mutually consistent) types of satellite-based information: a land cover classification into plant functional types (PFTs) (see section 2.2.2), and fAPAR (f(NDVI)). Therefore, the global NDVI dataset produced by the Global Inventory Modeling and Mapping Studies (GIMMS) –version g– was used to create a fAPAR dataset using an algorithm described by Los et al. (2000) (section 2.2.3). The GIMMS NDVI data are available at the Global Land Cover Facility (http://glcf.umiacs.umd.edu/) at a biweekly temporal resolution from 1982 to 2006 and a spatial resolution of 8 km $\times$ 8 km. The GIMMS NDVI data are derived from imagery obtained from the Advanced Very High Resolution Radiometer (AVHRR) instrument onboard the NOAA satellite series 7, 9, 11, 14, 16 and 17 (Tucker et al., 2005). GIMMS NDVI data are chosen because they cover a longer time period (1982-2006) compared to other satellite data sources (e.g. MODIS). Furthermore, the data are collected by a consistent series of instruments. In addition, several independent studies used earlier versions of the GIMMS NDVI data and showed reasonable agreement between GIMMS NDVI and other measures of vegetation (Davenport and Nicholson, 1993; Malmstrom et al., 1997; D'Arrigo et al., 2000).

Nevertheless, as any satellite-based measurement, GIMMS NDVI suffers from numerous deficiencies including sensor degradation, cloud contamination, limitation due to viewing geometry, and atmospheric effects. Therefore, GIMMS NDVI has been corrected for the following effects which are not related to vegetation change (Tucker et al., 2005):

- Residual sensor degradation and sensor inter-calibration differences between satel-

lites: the coefficients by Vermote and Kaufman (1995) are used to correct the visible and near infrared reflectances for in-flight sensor degradation.

- Solar zenith angle and viewing angle effects due to satellite orbit drift: the GIMMS NDVI datasets were corrected using the solar zenith angle values from the AVHRR sensor for the period 1981-2002 (Tucker et al., 2005).

- Volcanic aerosols: over the measurement period 1982-2006, there were two major volcanic eruptions, El Chichon in 1982 and Mt. Pinatubo in 1991, which injected large quantities of aerosols into the atmosphere. These aerosols can introduce significant variability in the AVHRR NDVI record. The GIMMS NDVI datasets were corrected for the known changes of the atmosphere from these two volcanic eruptions, but reductions in the NDVI signal are still visible over densely-vegetated tropical land cover for limited time periods.

- Low signal to noise ratios due to sub-pixel cloud contamination and water vapor: in order to construct cloud-free views of the Earth, composite images were constructed at regular temporal intervals by selecting pixels with the maximum NDVI during regularly spaced intervals. Choosing pixels with maximum NDVI reduces cloud cover and water vapor effects since both strongly reduce NDVI.

GIMMS NDVI spatial/temporal variations for a certain region/time are affected by these corrections, producing some variations, which are not related to actual variations in the vegetation. Also, some sources of error are not accounted for by the GIMMS corrections. One of these errors is caused by soil effects. Soils tend to darken when they are wet, so that their reflectance is a direct function of water content. If the spectral response to moistening is not exactly the same in the two spectral bands, the NDVI of an area can appear to change as a result of soil moisture changes (precipitation or evaporation) and not because of vegetation changes. However, this affects only low NDVI values, but does not affect high NDVI values.

Overall, GIMMS NDVI presents generalized patterns that may result in poor representations of the vegetation changes. Therefore, quantitative conclusions of the satellite-based estimates of ecosystem productivity should be drawn with caution. Details on development of the GIMMS NDVI dataset and its quality can be found in Tucker et al. (2005).

In the following sections, the procedures used to produce the land cover map and fAPAR dataset are discussed.
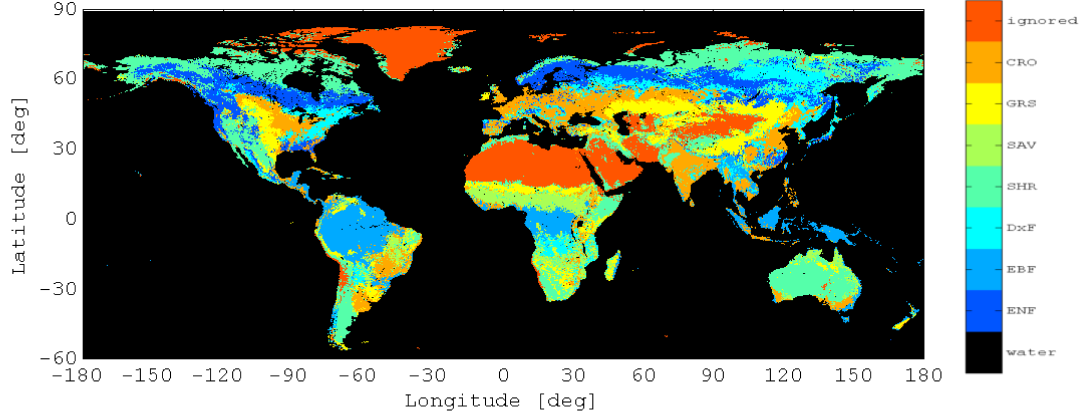
Figure 2.1—— The SYNMAP (Jung et al., 2006) land cover dataset aggregated into seven major PFTs (see table 2.1). PFT labels are described in table 2.2.

2.2.2   Land Cover Classification

To produce a land cover classification into plant functional types (PFTs), the synergetic land cover dataset (SYNMAP) from Jung et al. (2006) are projected to the GIMMS NDVI grid (8 km $\times$ 8 km). Then, its classifications are aggregated into seven major PFTs (see table 2.1 and figure 2.1). As a criterion of this aggregation, the spatial extent of the aggregated PFTs should not be too small in order to be distinguishable by the atmospheric observations through the atmospheric inversion calculations (see chapter 3). Therefore, classes of limited extent are joined to others. Also, all deciduous and mixed forests are joined into DxF (see table 2.1) (despite ecological differences between them).

For each PFT, a density map (fractional cover) $0 \leq \varrho_{\text{PFT}}(x, y) \leq 1$ is taken, by summing up the original land-surface classes:

$$\varrho_{\text{PFT}}(x, y) = \sum_{\text{class} \in \text{PFT}} \varrho_{\text{class}}(x, y). \tag{2.2}$$

The density map of all (non-ignored) land cover classes is

$$\varrho_{\text{veg}}(x, y) = \sum_{\text{PFT}} \varrho_{\text{PFT}}(x, y). \tag{2.3}$$

Table 2.1— SYNMAP (Jung et al., 2006) land cover classification and its aggregation into seven major PFTs. See table 2.2 for the descriptive abbreviations used for the PFTs.

SYNMAP (Jung et al., 2006)				7 major PFT's
Class	Life forms	Tree leaf type	Tree leaf longevity	PFT(index)
1	Trees	Needle	Evergreen	ENF (1)
2	Trees	Needle	Deciduous	DxF (3)
3	Trees	Needle	Mixed	DxF (3)
4	Trees	Broad	Evergreen	EBF (2)
5	Trees	Broad	Deciduous	DxF (3)
6	Trees	Broad	Mixed	DxF (3)
7	Trees	Mixed	Evergreen	DxF (3)
8	Trees	Mixed	Deciduous	DxF (3)
9	Trees	Mixed	Mixed	DxF (3)
10	Trees & Shrubs	Needle	Evergreen	ENF (1)
11	Trees & Shrubs	Needle	Deciduous	DxF (3)
12	Trees & Shrubs	Needle	Mixed	DxF (3)
13	Trees & Shrubs	Broad	Evergreen	SAV (5)
14	Trees & Shrubs	Broad	Deciduous	SAV (5)
15	Trees & Shrubs	Broad	Mixed	SAV (5)
16	Trees & Shrubs	Mixed	Evergreen	SAV (5)
17	Trees & Shrubs	Mixed	Deciduous	SAV (5)
18	Trees & Shrubs	Mixed	Mixed	DxF (3)
19	Trees & Grasses	Needle	Evergreen	ENF (1)
20	Trees & Grasses	Needle	Deciduous	DxF (3)
21	Trees & Grasses	Needle	Mixed	DxF (3)
22	Trees & Grasses	Broad	Evergreen	EBF (2)
23	Trees & Grasses	Broad	Deciduous	SAV (5)
24	Trees & Grasses	Broad	Mixed	SAV (5)
25	Trees & Grasses	Mixed	Evergreen	DxF (3)
26	Trees & Grasses	Mixed	Deciduous	DxF (3)
27	Trees & Grasses	Mixed	Mixed	SAV (5)
28	Trees & Crops	Needle	Evergreen	CRO (7)
29	Trees & Crops	Needle	Deciduous	CRO (7)
30	Trees & Crops	Needle	Mixed	CRO (7)
31	Trees & Crops	Broad	Evergreen	CRO (7)
32	Trees & Crops	Broad	Deciduous	CRO (7)
33	Trees & Crops	Broad	Mixed	CRO (7)
34	Trees & Crops	Mixed	Evergreen	CRO (7)
35	Trees & Crops	Mixed	Deciduous	CRO (7)
36	Trees & Crops	Mixed	Mixed	CRO (7)
37	Shrubs	-	-	SHR (4)
38	Shrubs & Grasses	-	-	SHR (4)
39	Shrubs & Crops	-	-	SHR (4)
40	Shrubs & Barren	-	-	SHR (4)
41	Grasses	-	-	GRS (6)
42	Grasses & Crops	-	-	GRS (6)
43	Grasses & Barren	-	-	GRS (6)
44	Crops	-	-	CRO (7)
45	Barren	-	-	(ignored) (8)
46	Urban	-	-	(ignored) (8)
47	Snow & Ice	-	-	(ignored) (8)

Table 2.2— Descriptive abbreviations used for PFTs.

Abbreviation (index)	Full name
ENF (1)	Evergreen needle
EBF (2)	Evergreen broadleaf
DxF (3)	Deciduous/mixed forest
SHR (4)	Shrubland
SAV (5)	Savanna
GRS (6)	Grassland
CRO (7)	Cropland

2.2.3 fAPAR

fAPAR is calculated following the approach described in Goward and Huemmrich (1992) and Sellers et al. (1996a) and further adapted by Los et al. (2000). Two linear equations between fAPAR and NDVI are described, referred to as the $fAPAR_{NDVI}$ and $fAPAR_{SR}$ models. In the $fAPAR_{NDVI}$ model, maximum and minimum NDVI values for each vegetation type are related to maximum and minimum fAPAR according to:

$$fAPAR_{NDVI} = \frac{NDVI - NDVI_{min}}{NDVI_{max} - NDVI_{min}} \cdot (fAPAR_{max} - fAPAR_{min}) + fAPAR_{min}$$

(2.4)

where $NDVI_{min}$ and $NDVI_{max}$ are the 2nd and 98th percentiles, respectively, of the NDVI frequency distribution estimated per PFT (see Table 2.3). $fAPAR_{min}$ and $fAPAR_{max}$ are parameters: 0.01 and 0.95, respectively.

Table 2.3— Lower (2nd) and upper (98th) NDVI percentiles estimated per PFT.

PFT(class)	$NDVI_{min}$	$NDVI_{max}$
ENF (1)	0	0.83
EBF (2)	0	0.90
DxF (3)	0	0.75
SHR (4)	0	0.81
SAV (5)	0	0.74
GRS (6)	0	0.80
CRO (7)	0	0.27

In the $fAPAR_{SR}$ model, fAPAR is linearly related to the simple ratio (SR) which can be expressed as a transformation of NDVI:

$$SR = \frac{1 + NDVI}{1 - NDVI} \tag{2.5}$$

$$fAPAR_{SR} = \frac{SR - SR_{min}}{SR_{max} - SR_{min}} \cdot (fAPAR_{max} - fAPAR_{min}) + fAPAR_{min} \tag{2.6}$$

where SR_{min} and SR_{max} respectively correspond to $NDVI_{min}$ and $NDVI_{max}$.

According to Los et al. (2000), an intermediate model, calculating the average fAPAR of the $fAPAR_{NDVI}$ and $fAPAR_{SR}$ models, performed better by giving the smallest bias in fAPAR estimates. Accordingly, fAPAR is calculated using the following relationship:

$$fAPAR = \frac{fAPAR_{SR} + fAPAR_{NDVI}}{2} \tag{2.7}$$

These calculations are done on a pixel basis with 8 km × 8 km spatial resolution. After that, the fAPAR data have been aggregated to a spatial resolution of 4° latitude × 5° longitude to match the atmospheric transport model (TM3) (Heimann and Körner, 2003) that is used in the inverse model (see chapter 3). Then, a separate dataset, $fAPAR_{PFT}$, is created for each PFT.

The full temporal variability and the interannual variability of the calculated fAPAR from GIMMS NDVI data are shown in figure 2.2. The time series is aggregated over three latitudinal bands (for a map of the regions see figure 2.4). The interannual variability (IAV) is obtained by subtracting the mean seasonal cycle and most variations faster than 1 year (Gaussian spectral weights, as in Rödenbeck (2005)). In the northern hemisphere, fAPAR has striking seasonal changes, i.e., small values in winter and high values in summer, reflecting the vegetation phenology of the region. Over the tropics and the southern hemisphere bands, the interannual variability has more variations. This was expected since the NDVI dataset is most affected by satellite orbit drift and changes to the magnitude of the solar zenith angle in tropics and the southern hemisphere. Also, the natural variability in atmospheric aerosols and column water vapor may have created surface-independent variations in the GIMMS NDVI record (Tucker et al., 2005). As a consequence, fAPAR inherited these variations that may not be caused by vegetation variation. In June 1991, a major volcanic eruption occurred (the Pinatubo eruption), injecting large quantities of aerosols into the Earth's stratosphere. These aerosols and subsequent cooling can explain the decline in the interannual variability of fAPAR during the period from 1991-1993 over the tropics.

Consequently, by using satellite-derived fAPAR dataset to drive the photosynthesis model,

simulated GPP will be affected by a substantial variability in fAPAR that is not related to actual changes in vegetation function. Therefore, simulated GPP should be interpreted with caution.

2.2.4 Meteorological Data

Climate data are one of the inputs needed to drive SDPRM. Therefore, the improved reanalysis dataset from the National Center for Environmental Prediction/National Center for Atmospheric Research Reanalysis (NCEP/NCAR) (Kalnay et al., 1996) has been obtained for the period 1982-2006. The NCEP/NCAR dataset consists of a reanalysis of the global observational network of meteorological variables (wind, temperature, pressure, humidity). Data are produced on a $2.5° \times 2.5°$ grid box with temporal resolution of 6 hours or daily. NCEP/NCAR dataset has been aggregated to the TM3 resolution of $4°$ latitude $\times 5°$ longitude.
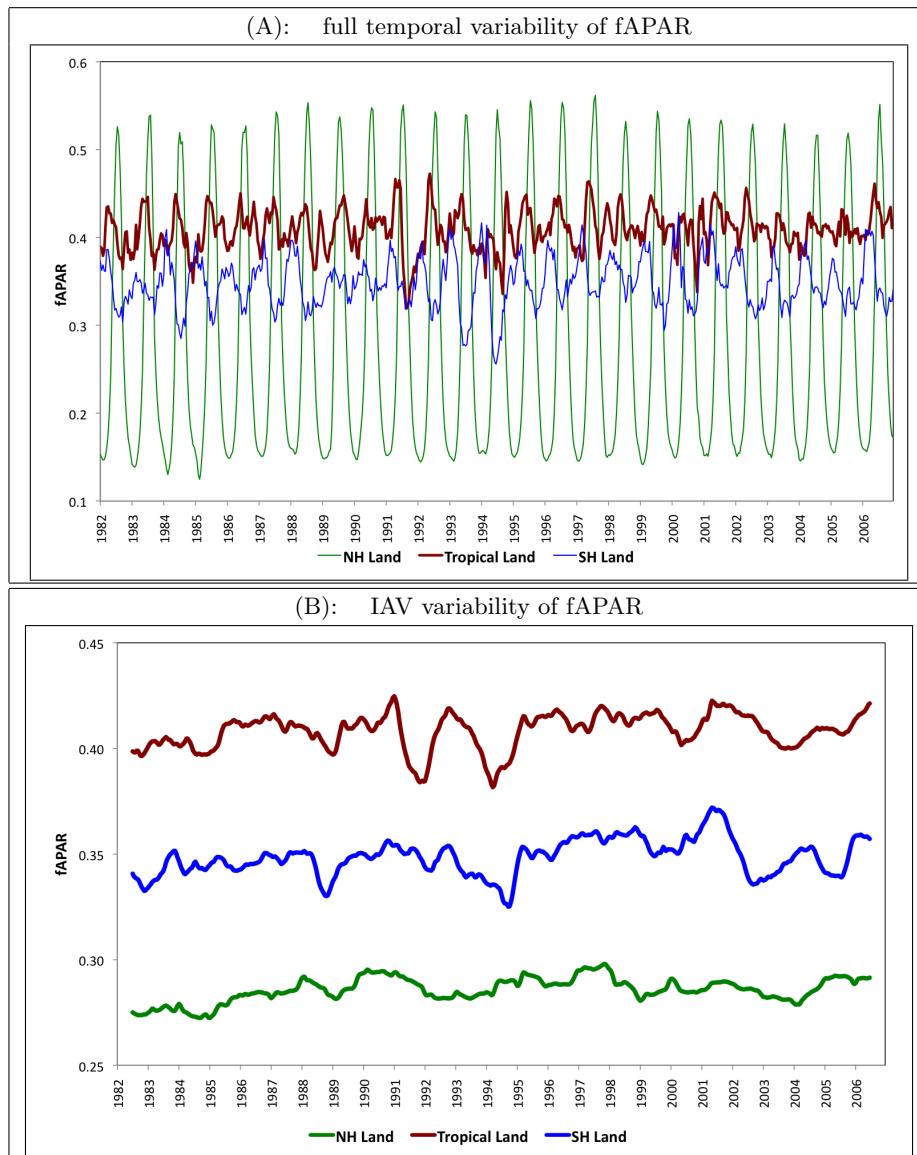
Figure 2.2— Integrated fAPAR time series calculated from GIMMS NDVI across three latitudinal bands: (A) time series of the full temporal variability of fAPAR, (B) time series of the interannual variability of fAPAR (subtracting the mean seasonal cycle and most variations faster than 1 year (Gaussian spectral weights, as in Rödenbeck (2005)). For a map of the regions see figure 2.4.

2.3 Ecosystem Respiration Model

2.3.1 Background

Several approaches have been used in the global modeling of soil respiration. On the one hand, there are a number of mechanistically based models that integrate knowledge of physiological and ecological processes to model the response of the system to environmental changes (Cramer et al., 2001; Schimel et al., 2000; McGuire et al., 2001). On the other hand, there are simple statistical models that implement empirical relations between soil respiration and important environmental factors (e.g. Lloyd and Taylor (1994)).

Many studies have highlighted important drivers influencing soil respiration which include (1) soil temperature (Lloyd and Taylor, 1994; Reichstein et al., 2003), (2) soil water status (Carlyle and Than, 1988; Howard and Howard, 1993), (3) net primary or net ecosystem productivity (Norman et al., 1992; Raich and S., 1995; Janssens et al., 2001), (4) substrate quality (Raich and Schlesinger, 1992), (5) land-use and disturbance regimes (Ewel et al., 1987), and (6) population and community dynamics of the above- and below-ground flora and fauna (Raich and Schlesinger, 1992). Modeling of all these complex interactions is unfeasible particularly at larger spatial scales. Therefore, models have to employ simpler relations empirically derived from field studies. Thus, soil respiration is often modeled as a simple Q_{10} (a parameter that represents the increase in respiration for every 10 °C rise in temperature) or Arhennius-type function of temperature. For example, Lloyd and Taylor (1994) used the exponential regression model to relate Ecosystem Respiration (R_{eco}) to either air or soil temperature as follows:

$$R_{eco} = R_{ref} \; e^{E_0 \left(\frac{1}{T_{ref} - T_0} - \frac{1}{T - T_0} \right)} \tag{2.8}$$

where the regression parameter T_0 is -46.0 °C, E_0 is the activation energy, and R_{ref} is the soil respiration at the reference temperature T_{ref} (10 °C).

Likewise, Raich et al. (2002) predict soil respiration from monthly average air temperature (T_a) and precipitation (P) summed over the preceding 30 days as follows:

$$R_{month} = R_0 \cdot e^{Q \cdot T_a} \cdot \frac{P}{P + K} \tag{2.9}$$

where R_{month} refers to the mean monthly soil respiration (gC m^{-2} day^{-1}), R_0 (gC m^{-2} day^{-1}) is the soil respiration at 0°C without moisture limitation, Q (K^{-1}) determines the exponential relationship between soil respiration and temperature, and K (cm) is the half-saturation constant of the hyperbolic relationship of soil respiration with

monthly precipitation.

Further, Reichstein et al. (2003) introduced new parameters into the model proposed by Raich et al. (2002) (equation 2.9) to account for the importance of drought effects on soil respiration as

$$R_{month} = (R_{LAI=0} + S_{LAI} \cdot LAI) \cdot e^{Q \cdot T_a} \cdot \frac{P + P_0}{P + P_0 + K} \tag{2.10}$$

where the term $(R_{LAI=0} + S_{LAI}.LAI)$ describes a linear dependency of the basal rate of soil respiration on site peak Leaf Area Index (LAI), while Q, T_a, P, and K are as in equation (2.9). The parameter P_0 is a simple representation of the fact that there can be soil respiration in months without rain, amounting to the fraction $P_0/(K + P_0)$ of non-water-limited soil respiration. Also, according to the assumption made by Reichstein et al. (2003) that soil respiration is proportional to site productivity, the term $R_{LAI=0} + S_{LAI}.LAI$ can be written as an exponential relationship of the form $R_0 + R_{LAI}.(1 - e^{-k\ LAI}$.

2.3.2   Model Equations

Following the formulations introduced by Lloyd and Taylor (1994) and Raich et al. (2002) and the modification made by Reichstein et al. (2003), the Ecosystem Respiration (R_{eco}) can be simulated using the following equations

$$
\begin{aligned}
R(x,y,t) &= \Big(R_0(x,y) + R_{LAI}(x,y) \cdot r_{LAI}[k, LAI(x,y,t)] \Big) & (2.11)\\
&\cdot\quad r_T[E(x,y), T(x,y,t)] & (2.12)\\
&\cdot\quad r_P[P_0(x,y), K(x,y), P(x,y,t)] & (2.13)
\end{aligned}
$$

where R_{LAI} is the dependency of the respiration rate on maximum leaf area index (LAI_{max}), and the leaf area index (LAI) dependence is calculated as

$$r_{LAI}[k, LAI] = (1 - e^{-k \cdot LAI_{max}}) \tag{2.14}$$

and the temperature dependence is calculated as

$$r_T[E, T] = \exp\left(-E\left[\frac{1}{T - T_0} - \frac{1}{T_{ref} - T_0}\right]\right) \tag{2.15}$$

where E is the activation energy , $T_0 = -46°C$ (minimum temperature) as in Lloyd and Taylor (1994) and $T_{ref} = 13°C$ (reference temperature, taken from the 1901-2002 mean of the CRU dataset over land [13.1°C]).

The precipitation dependence is written as

$$r_P[P_0, K, P] = \frac{P + P_0}{P + P_0 + K} \tag{2.16}$$

The respiration model comprises both autotrophic and heterotrophic respiration, because, due to similar dependencies on driving data, it is not expected that the signals from both can be separated from the atmospheric CO_2 measurements (by using the inverse model - see chapter 3). This model involves the adjustable parameters $R_0(x,y)$, $R_{LAI}(x,y)$, k, $E(x,y)$, P_0, and K. It is driven by leaf area index $LAI(x,y,t)$ and the meteorological fields from NCEP (daily mean temperature at 2 m $T(x,y,t)$, and precipitation summed over the previous 30 days $P(x,y,t)$). The model is simplified by the following assumptions:

- LAI dependence can be replaced by the average of the yearly maximum $fAPAR$ value (Los et al., 2000),

$$r_{LAI}(x,y) = \overline{\max(fAPAR(x,y,t))} \tag{2.17}$$

- The parameters R_0 and R_{LAI} are assumed constant over all PFTs, because there is no solid information on how to break them down spatially. Since the two patterns $r_{LAI}(x,y)$ and $\varrho_{\text{veg}}(x,y)$ turn out to be very similar, the atmospheric information is not expected to be able to distinguish them. Therefore, the parameters R_0 and R_{LAI} are written as

$$R_0(x,y) = R_0 \cdot \varrho_{\text{veg}}(x,y), \tag{2.18}$$

$$R_{LAI}(x,y) = R_{LAI} \cdot \varrho_{\text{veg}}(x,y), \tag{2.19}$$

- Likewise, the parameters E and K are assumed to be global.

- The parameter P_0 is fixed to the global value $P_0^{\text{pri}} = 1.55$ mm/month (95% confidence interval: [0.2,2.5]) taken from Reichstein et al. (2003).

The model then reads

$$
\begin{align}
R(x,y,t) &= \Big(R_0 + R_{LAI} \cdot r_{LAI}(x,y)\Big)\varrho_{\text{veg}}(x,y) \tag{2.20}\\
&\quad \cdot \quad r_T[E, T(x,y,t)] \tag{2.21}\\
&\quad \cdot \quad r_P[P_0^{\text{pri}}, K, P(x,y,t)] \tag{2.22}
\end{align}
$$

For the a-priori best-guess values and uncertainties of the original parameters, the following values are chosen from the soil-respiration values of Reichstein et al. (2003) assuming that soil respiration accounts for 60% of ecosystem respiration.

- $R_0^{pri} = 0.8$ gC/m^2/day

- $R_{LAI}^{pri} = 2.5$ gC/m^2/day

- $K^{pri} = 2.15$ mm/month

- $E^{pri} = 135$ K

E^{pri} corresponds to $Q_{10} = 1.47$ (Reichstein et al., 2003), which is a relatively low value, reflecting the fact that the present model is formulated in terms of air temperature (rather than the more usual soil temperature) which has more temporal variability than the temperature of the soil and most of the plant tissue that drive ecosystem respiration.

In chapter 3, the model will be coupled to STD-inv in order to optimize the model parameters by fitting the atmospheric measurements of CO_2.

2.4   Photosynthesis model

2.4.1   Background

Gross primary production (GPP), the photosynthetic uptake of carbon, is defined as the total carbon fixed by plants through photosynthesis. The relationship between GPP and the fraction of Absorbed Photosynthetically Active Radiation (fAPAR) was first proposed by Monteith (1977). Based on that, GPP is commonly modeled as a function of climatic and soil variables, and uses satellite-derived estimates of the vegetation's light-absorbing properties (e.g. Randerson et al. (1996); Sellers et al. (1996b); Kaminski et al. (2002); van der Werf et al. (2004)). In general, these models are known as light use efficiency (LUE) models.

Here, we present the algorithm used in this thesis to provide estimates of GPP using satellite-derived variables. The algorithm is similar to the radiation conversion efficiency concept presented in the MODIS17 user's guide (Heinsch et al., 2003) (MODIS17 - Global GPP and NPP User's Guide is available at http://www.ntsg.umt.edu/modis/MOD17UsersGuide.pdf). The initial parameter values of the GPP model are taken from the MODIS17 Biome Property Look-Up Table (BPLUT) (Heinsch et al., 2003). The parameters in BPLUT are based on the synthesized NPP data and observed GPP derived from some flux tower measurements (Heinsch et al., 2003).

The model is driven by fAPAR data calculated from GIMMS NDVI data (see section 2.2.3), and meteorological fields (from NCEP). GPP is calculated for 7 Plant Functional Types (PFTs) (see section 2.2.2 and 2.2.3).

2.4.2   Model Equations

The MODIS17 algorithm (LUE algorithm) calculates GPP as the product of Absorbed Photosynthetically Active Radiation (APAR) and light use efficiency (ε):

$$GPP = \varepsilon \cdot APAR \tag{2.23}$$

where ε is calculated by attenuating maximum light use efficiency (mass of assimilated carbon per unit energy of absorbed radiation) (ε_{max}) via the effect of temperature (g_T) and vapor pressure deficit (g_{VPD}) factors:

$$\varepsilon = \varepsilon_{max} \cdot g_T \cdot g_{VPD} \tag{2.24}$$

APAR is calculated by the product of the amount of Photosynthetically Active Solar

Radiation (PAR) and the fraction of incident PAR absorbed by vegetation (fAPAR):

$$APAR = PAR \cdot fAPAR \tag{2.25}$$

The attenuation factors (g_T) (g_{VPD}) in equation 2.24 are simple ramp functions of daily minimum temperature T_{min} and vapor pressure deficit VPD (see figure 2.3). Based on that, the dependence on daytime mean VPD can be defined as:

$$g_{VPD}[VPD_1, VPD_0, VPD] = \begin{cases} 1, & VPD < VPD_1 \\ \frac{VPD_0 - VPD}{VPD_0 - VPD_1}, & VPD_1 < VPD < VPD_0 \\ 0, & VPD > VPD_0 \end{cases} \tag{2.26}$$

and the dependence on daily minimum temperature can be defined as:

$$g_T[T_{\min,0}, T_{\min,1}, T_{\min}] = \begin{cases} 0, & T_{\min} < T_{\min,0} \\ \frac{T_{\min} - T_{\min,0}}{T_{\min,1} - T_{\min,0}}, & T_{\min,0} < T_{\min} < T_{\min,1} \\ 1, & T_{\min} > T_{\min,1} \end{cases} \tag{2.27}$$

with $T_{\min,0} = $ -8°C/. The values of $T_{\min,1}$, VPD_1 and VPD_0 are given in table 2.4.

In this study, GPP calculation focuses on seven major Plant Functional Types (PFTs). Thus, the GPP formula can be written as:

$$
\begin{aligned}
GPP(x,y,t) \quad = \sum_{\text{PFT}} \quad & \varepsilon_{max\text{PFT}} \cdot \varrho_{\text{PFT}}(x,y) \cdot fAPAR_{\text{PFT}}(x,y,t) \cdot PAR(x,y,t) \\
\times \quad & g_{VPD}[VPD_1(\text{PFT}), VPD_0(\text{PFT}), VPD(x,y,t)] \\
\times \quad & g_T[T_{\min,0}(\text{PFT}), T_{\min,1}(\text{PFT}), T_{\min}(x,y,t)]
\end{aligned}
\tag{2.28}
$$

with $\varepsilon_{max\text{PFT}}$: Maximum light use efficiencies per PFT(see table 2.4), $fAPAR_{\text{PFT}}(x,y,t)$: fraction of Absorbed Photosynthetically Active Radiation per PFT, $VPD(x,y,t)$: Daytime mean vapor pressure deficit of the air, $T_{\min}(x,y,t)$: Daily minimum air temperature, and Photosynthetically Active Radiation (PAR) is calculated as approximately 45% of incident solar radiation I, as

$$PAR(x,y,t) = 0.45 \cdot I(x,y,t) \tag{2.29}$$

Table 2.4— Definition of plant functional types, and values of PFT-dependent parameters of the photosynthesis model.

Class	$\varepsilon_{\text{PFT}}^{\text{pri}}$ (gC/MJ)	$T_{\text{min},1\text{PFT}}^{\text{pri}}$ (°C)	$VPD1_{\text{PFT}}^{\text{pri}}$ (Pa)	$VPD0_{\text{PFT}}^{\text{pri}}$ (Pa)
ENF	1.0	8.3	650	3100
EBF	1.0	9.1	1100	3600
DxF	1.2	9.5	935	3350
SHR	0.8	8.7	970	4100
SAV	0.8	11.4	1100	5000
GRS	0.6	12.0	1000	5000
CRO	1.1	12.0	930	4100

The a-priori GPP fields given for each PFT can be written as

$$
\begin{aligned}
GPP_{\text{PFT}}^{\text{pri}}(x,y,t) &= \varepsilon_{max\text{PFT}}^{\text{pri}} \cdot \varrho_{\text{PFT}}(x,y) \cdot fAPAR_{\text{PFT}}(x,y,t) \cdot I(x,y,t) \cdot 0.45 \\
&\cdot\ g_{VPD}[VPD_1, VPD_0, VPD(x,y,t)] \\
&\cdot\ g_T[T_{\text{min},0}, T_{\text{min},1}, T_{\text{min}}(x,y,t)]
\end{aligned}
$$

(2.30)
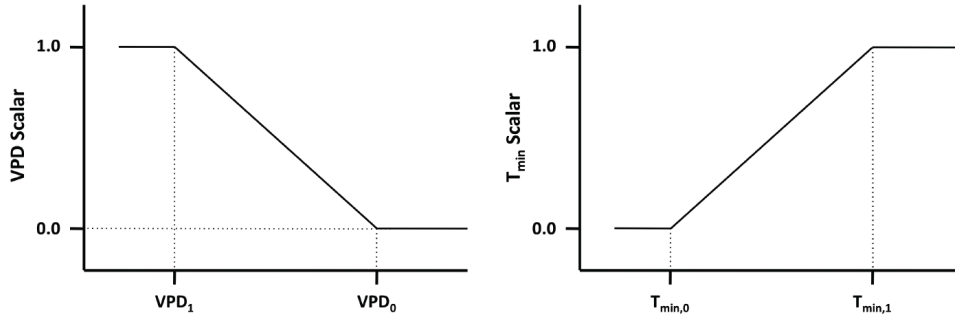
Figure 2.3— The VPD and TMIN attenuation scalars are simple linear ramp functions of daily T_{min} and VPD.

Incident radiation $I(x,y,t)$ is calculated from the downward shortwave radiation $I_{\text{SW}}(x,y,t)$ from NCEP meteorological reanalysis, which should contain both the seasonal and synoptic variability, while the diurnal variation is only coarsely represented in the 6-hourly fields. Therefore, incident radiation is calculated by

$$I(x, y, t) = j(x, y, t) \cdot I_0(x, y, t) \tag{2.31}$$

from the purely geometrical clear-sky radiation

$$I_0(x, y, t) = \max(0, \ \sin(y) \cdot \sin(x_\Delta) + \cos(y) \cdot \cos(x_\Delta) \cdot \cos(x_h)) \tag{2.32}$$

with

$$x_h = 360° r_{\text{day}}(t) + x - 180° \tag{2.33}$$

$$x_\Delta = -23.4° \cdot \cos(360° r_{\text{year}}(t) + 10°) \tag{2.34}$$

where $r_{\text{day}}(t)$ and $r_{\text{year}}(t)$ give the fractions of the day (since 00Z UTC) and of the year (since Jan 1) at time t, and x and y are taken to represent longitude and latitude. The cloud factor $j(x, y, t)$ is obtained by the following equation at the 6-hourly meteorological intervals, and linearly interpolated in between.

$$j(x, y, t) = \frac{I_{\text{SW}}(x, y, t)}{I_0(x, y, t)} \tag{2.35}$$

$VPD(x, y, t)$ is calculated as a daytime mean from specific humidity q (kg/kg), surface pressure p (Pa) $\approx 101300\,\text{Pa}$, air temperature at 2 m height T (°C , and the ratio $\kappa = 0.62197$ of the molar masses of water vs. air as

$$VPD = 611\,\text{Pa} \cdot \exp\left(\frac{17.26938818 \cdot T}{237.3 + T}\right) - \frac{q \cdot p}{\kappa - q(\kappa - 1)} \tag{2.36}$$

(difference between actual partial pressure of water vapor and saturation water vapor pressure in Pa). The daytime average was done using $I_0(x, y, t)$ from equation 2.32 as weighting, and applying a triangular filter to de-diurnalize.

GPP from the photosynthesis model, like R_{eco}, is used as a-priori fields in STD-inv (more details in chapter 3). The results of both the respiration and photosynthesis models are presented in the following sections.

2.5   Implementation Details and Results

SDPRM calculates 3-hourly GPP for seven major PFTs and daily R_{eco}. The calculations for GPP and R_{eco} are conducted independently based on equations 2.20 and 2.30, respectively. Then, daily NEE is calculated as the difference of the two fluxes at each $4°$ latitude $\times 5°$ longitude land grid cell as

$$NEE = R_{eco} - GPP \tag{2.37}$$

As climatic input, we used daily mean and minimum temperature, daily precipitation, and 6-hourly incoming surface solar radiation. In addition, other inputs are used: (1) daytime VPD calculated from reanalyzed specific humidity, surface pressure, and temperature using equation 2.36 and (2) fAPAR calculated from GIMMS NDVI data (section 2.2.3). The a-priori values of the model's parameter are shown in table 2.4 and section 2.3.

Kaminski and Heimann (2001) showed that using incorrect a-priori fluxes could seriously distort the inversion calculations. Therefore, we have performed several experiments to test the performance of the model and its ability to produce realistic a-priori fields for the inverse model. The estimates of NEE from SDPRM are compared with the land flux inferred from the atmospheric measurements of CO_2 using STD-inv. This is in order to justify that the a-priori land fluxes from SDPRM can, to some extent, capture some of the variability inferred from the atmospheric measurements.

Furthermore, the simulated carbon cycle components (NEE, GPP, and R_{eco}) from SDPRM were compared with the results of the BIOME-BGCv1 process-based model provided by the Max-Planck Institute for Biogeochemistry (Trusilova and Churkina, 2008). BIOME-BGCv1 is based on the core of the BIOME-BGC version 4.1.1 (Thornton et al., 2005) point-based model. BIOME-BGC prognostically simulates the states and fluxes of carbon, nitrogen, and water within the vegetation, litter, and soil components of a terrestrial ecosystem. BIOME-BGC Version 4.1.1 was developed by the Numerical Terradynamic Simulation Group, School of Forestry, The University of Montana, Missoula, Montana, USA. Additional information can be found at http://www.ntsg.umt.edu/. The flux estimates from BIOME-BGC depend strongly on daily weather conditions. The model behavior over time depends on the history of these weather conditions (Climate). The BIOME-BGCv1 model uses the NCEP/NCAR meteorological fields as driving data. The model uses a daily time-step, hence each flux is estimated for a one-day period.

In BIOME-BGCv1, the total ecosystem respiration (R_{eco}) includes three components: maintenance respiration (MR), growth respiration (GR), and heterotrophic respiration

(HR). MR of each plant compartment is computed as a function of compartment nitrogen content and temperature. GR is calculated on the basis of construction costs by plant compartment. Different construction costs are applied to woody and non-woody plant tissues. HR includes decomposition of both litter and soil. It is related to their chemical composition (cellulose, lignin, and humus), to their carbon to nitrogen ratios, to soil mineral nitrogen availability and to soil moisture and temperature. The Gross Photosynthetic Production (GPP) is calculated based on absorbed photosynthetically active radiation, atmospheric carbon dioxide concentration, air temperature, vapor pressure deficit, soil water content, atmospheric nitrogen deposition, the leaf area index, and available nitrogen content in soil. For the comparison, the BIOME-BGCv1 results were aggregated to the spatial resolution of $4° \times 5°$ to be the same as the spatial resolution of both SDPRM and STD-inv. Further details about the structure of BIOME-BGCv1 are described in Trusilova et al. (2009).

The comparison between SDPRM, BIOME-BGCv1, and STD-inv is referred to as Experiment-1. In addition, we performed another analysis, Experiment-2, to understand the controlling mechanisms of GPP and R_{eco} by evaluating the contribution of each climate variable to the interannual variations in GPP and R_{eco}.

Several studies have shown that most ecosystem models can easily capture the general seasonality of ecosystem productivity because temperature and solar radiation dominate seasonal phenology (White et al., 1997; Leuning et al., 2005). But on the other hand, comparison between the interannual variations (IAV) in ecosystem productivity simulated by different ecosystem models show large differences. This is because different models have different formulations representing ecosystem processes and environmental stresses (McGuire et al., 2001). Therefore, the focus of the analyses is mainly on the interannual variability and to a lesser extent on the full temporal variability of the results (seasonal cycle). To obtain the interannual variability from the daily fluxes, the estimated fluxes are filtered by subtracting the mean seasonal cycle and most variations faster than 1 year (Gaussian spectral weights, as in Rödenbeck (2005)). This filter essentially retains annual averages. Likewise for the spatial resolution of the results, the estimated fluxes are integrated either into three latitudinal bands (90°S - 20°S, 20°S - 20°N and 20°N - 90°N) or into regions as defined in the TransCom3 project (Gurney et al., 2002) (see figure 2.4).

Before we present Experiment-1 and Experiment-2, it is useful to show the spatial pattern of annual GPP and R_{eco} estimated by SDPRM for the period 1982-2006. In addition, the standard deviation (σ) of the seasonal cycle and the interannual variability of the estimated fluxes (GPP and R_{eco}) have been calculated for each grid cell (see figures 2.5 and 2.6).

Based on the flux estimates from SDPRM, the long-term mean of R_{eco} and GPP are 74.5 and 75.5 PgC/year, respectively (1 Petagram = 1 x 10^{15} g). These values are smaller in comparison to earlier estimates presented in the IPCC AR4 (2007) (GPP = 120 PgC/year, R_{eco} = 119.6 PgC/year). There are two possibilities to adjust the long-term mean of GPP and R_{eco} from SDPRM. One possibility is to change the model parameters manually until they reach long-term values that match earlier estimates. The other possibility, which is the aim of this thesis, is to use a systematic method for optimizing parameters by coupling the biosphere model to the atmospheric inversion (see chapter 3).

Figure 2.5-A and 2.6-A show that GPP and R_{eco} have high values (global annual) in areas covered by forests and woody savannas, especially in the tropical regions. Low GPP and R_{eco} occur in areas dominated by adverse environments, such as high latitudes with short growing seasons constrained by low temperatures, and dry areas with limited water availability. The highest annual GPP and R_{eco} are found in Amazonia, central Africa, and temperate regions in northern and southern America where both temperature and moisture requirements are fully satisfied for photosynthesis and respiration. The lowest GPP and R_{eco} are found in cold or arid regions, where either temperature or precipitation are limiting (see section 2.5.2).

The spatial distribution of the standard deviation of the IAV of GPP and R_{eco} are shown in figure 2.5-B and 2.6-B, respectively. It is clear that the standard deviation of GPP and R_{eco} is large where their annual values are high and small where they are low. Similarly, figure 2.5-C and 2.6-C show the spatial distribution of the standard deviation of the seasonal cycle (full temporal variability) of GPP and R_{eco}. The figures show that the largest amplitude of the seasonal cycle of GPP occurs in the northern hemisphere. This reflects the vegetation phenology of the northern hemisphere regions, small GPP estimates in winter and high GPP estimates in summer. Similar behavior for the amplitude of the seasonal cycle of R_{eco} can be seen in figure 2.6-C. It is also clear that the amplitude of the seasonal cycle of GPP is higher than the amplitude of the seasonal cycle of R_{eco}, in particular in the northern hemisphere regions (see also figure 2.12 and 2.14).

2.5.1 Experiment-1

As an evaluation of the results of SDPRM, we present the inter-comparison between the IAV of the estimated fluxes from SDPRM, STD-inv, and BIOME-BGCv1 for the period from 1982 to 2006. As noted in section 2.2.3, the fAPAR dataset may contain some variations which are not related to actual changes in the vegetation. As a consequence, the simulated GPP will be affected by these variations in fAPAR (and hence NEE). Therefore, to remove the spurious trends in the fAPAR data, we performed a sensitivity simulation

(A):   Three latitudinal regions
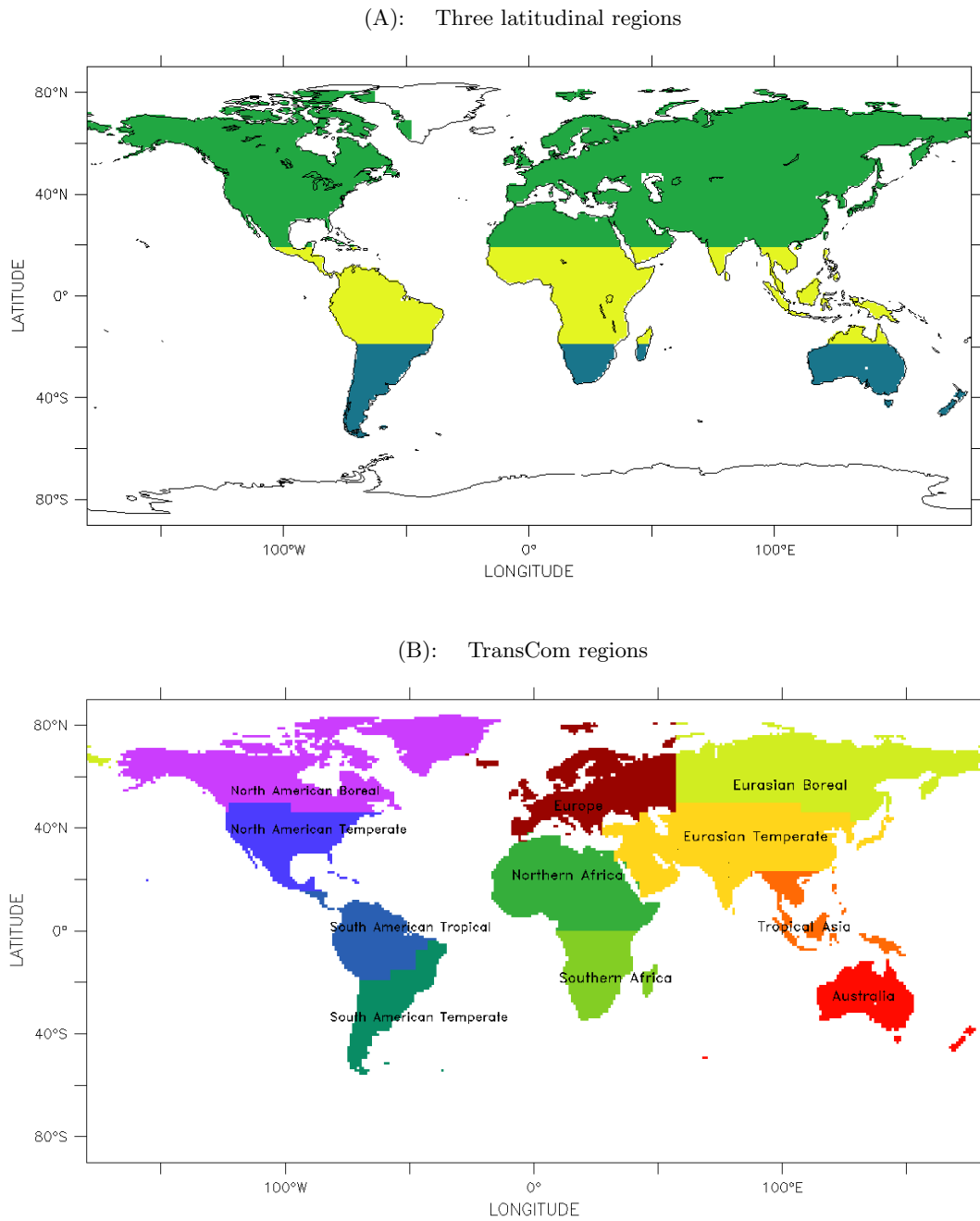
(B):   TransCom regions

Figure 2.4— Map of the land regions over which the estimated fluxes are integrated to obtain time series. (A) land regions for three latitudinal bands defined as (90°S - 20°S, 20°S - 20°N and 20°N - 90°N). (B) Land regions as defined in the TransCom3 project (Gurney et al., 2002).

(A):   Annual GPP (gC/m^2/year)

(B):   Standard deviation of the IAV of GPP (gC/m^2/year)

(C):   Standard deviation of the seasonal cycle of GPP (gC/m^2/year)
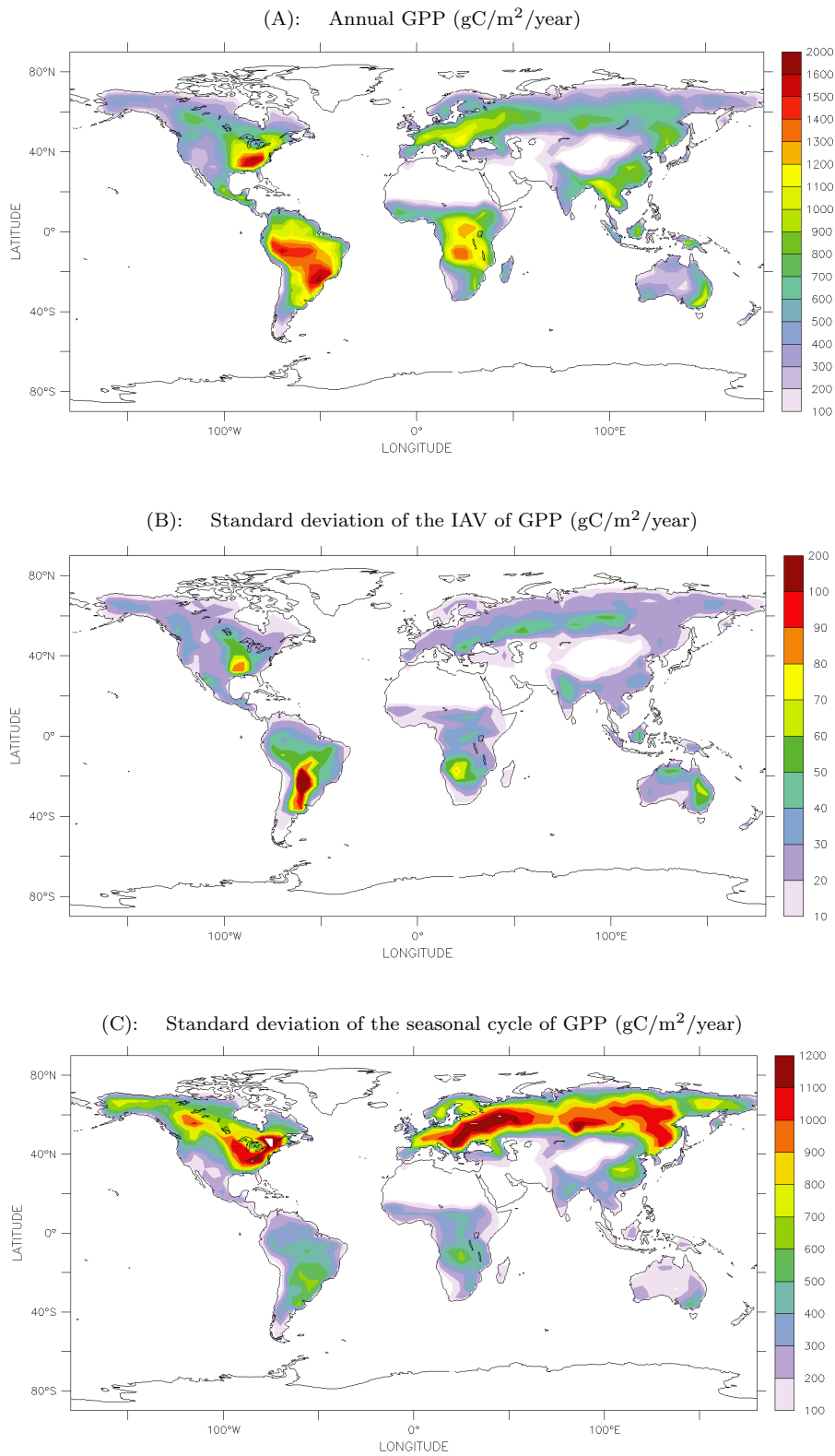
Figure 2.5— A: global map of annual GPP, B: standard deviation of the IAV of GPP, C: standard deviation of the seasonal cycle of GPP. The calculations are done for each grid cell for the period 1982-2006. Units are gC/m^2/year.
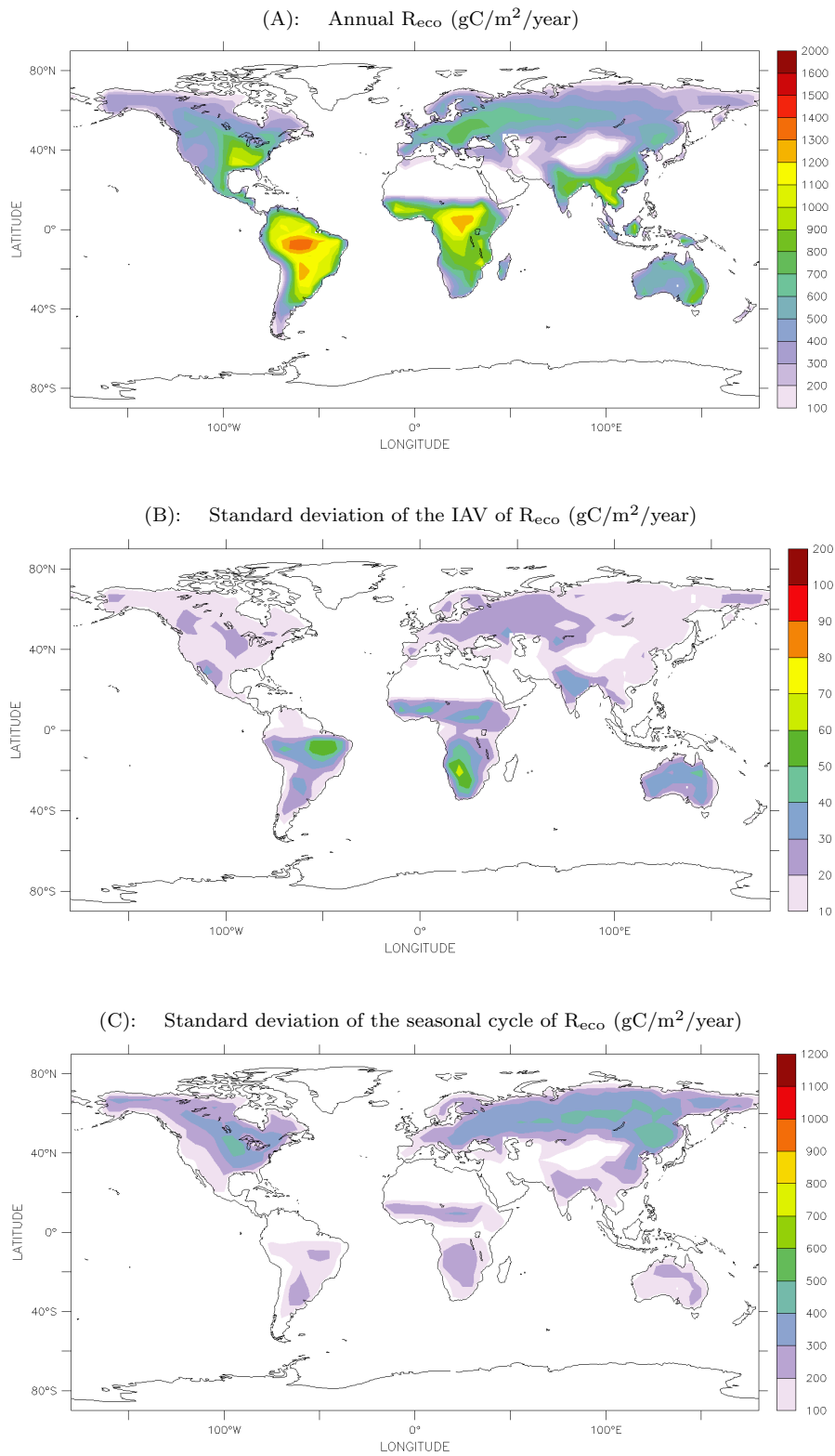
Figure 2.6— A: global map of annual R_{eco}, B: standard deviation of the IAV of R_{eco}, C: standard deviation of the seasonal cycle of R_{eco}. The calculations are done for each grid cell for the period 1982-2006. Units are gC/m^2/year.

assuming constant vegetation by using the mean seasonal cycle of the fAPAR time series for the period 1982-2006 (hereafter referred to as CfAPAR). Then the simulated NEE from the CfAPAR run is compared with the simulated NEE using the full temporal variability of fAPAR time series (referred to as VfAPAR). In both simulations, we used varying climate (daily NCEP/NCAR reanalysis data).

Table 2.5— Summary of the sensitivity runs (Experiment-1).

Acronym	Description
VfAPAR	full temporal variability of fAPAR + Climate varying
CfAPAR	Mean seasonal cycle of fAPAR + Climate varying

Figure 2.7 shows the comparison between the anomaly (subtracting the mean of 1982-2006) of the IAV of the simulated NEE from the two runs CfAPAR and VfAPAR and the estimated land flux from STD-inv. We can see that the IAV of the NEE from the VfAPAR case has some striking peaks, in particular over the tropics, during the period 1991-1993 compared to STD-inv. This can be explained by the variability in fAPAR (inherited from GIMMS NDVI) during the period from 1991-1993 over the tropical region due to the Pinatubo eruption, which injected large quantities of aerosols into the stratosphere. These aerosols, along with smoke from biomass burning and dust from soil erosion and other factors, can introduce significant variability in the AVHRR NDVI record (Tucker et al., 2005) and hence the fAPAR data. The correlation analysis shows that the correlation coefficient between the IAV of the global NEE time series from the VfAPAR run and the estimated global land flux from STD-inv is $r = 0.31$.

On the other hand, we can see that the IAV of NEE estimates from the CfAPAR run can capture a substantial fraction of the IAV of the land flux as inferred from the atmospheric information using STD-inv. The correlation coefficient between the two land estimates is higher compared to the estimates from the VfAPAR run ($r = 0.53$). This suggests that most of the IAV of NEE is dominated by the climate signal, not by the fAPAR. Or in other words, modeling ecosystem productivity using climatological fAPAR and varying climate date would produce a reasonable match to the inversion results. This also may indicate that the GIMMS NDVI data may not be accurate and may be problematic in certain regions/periods and should be used with caution (see also Nemani et al. (2003)).

Further comparison has been carried out between the simulated NEE from SDPRM using CfAPAR run and NEE simulated by BIOME-BGCv1, which is a process-based model. The comparison between the two models is illustrated in figure 2.9 for 3 latitudinal bands (see figure 2.4-A). The estimates of the land flux from STD-inv is shown in the same

figure. The comparison shows that the IAV of NEE from the CfAPAR run has a similar pattern compared to the NEE estimated by the BIOME-BGCv1 model, in particular over the tropics ($r = 0.63$). Similarly, figure 2.11 shows the same comparison but over smaller regions (see figure 2.4-B). There are two things we can see in this figure. First, SDPRM and BIOME-BGCv1 agree well but not perfectly over many regions, second. STD-inv has higher IAV of the land flux as well as a different pattern compared to SDPRM and BIOME-BGCv1. Due to the scarcity of the atmospheric CO_2 observations, the results of STD-inv might not be well constrained over smaller regions. Also, missing processes (e.g. fire) in the biosphere models can also be the reason for the differences between the flux variability shown in figure 2.11.

The seasonal cycle of the flux estimates from the three models are shown (in figures 2.8 and 2.10) for a selected period. The general phase of the seasonal cycle of NEE from the CfAPAR run is similar to the seasonal cycle of the land flux estimated from STD-inv over northern hemisphere land (NH). Furthermore, the amplitude is higher in our model but is fairly well simulated compared to the more sophisticated model (BIOME-BGCv1), which leads STD-inv by perhaps 2 months. The seasonality over the tropical and southern hemisphere (SH) regions is smaller compared to the NH land. This is because the high variations of major drivers of the carbon cycle (precipitation, temperature, fire, and nutrient availability) in tropical regions.

Additionally, the simulated carbon cycle components (GPP and R_{eco}) from SDPRM (CfAPAR run) are compared with the results from BIOME-BGCv1 for both the IAV and the seasonal cycle (figures 2.13 and 2.14). The comparisons show that GPP and R_{eco} from SDPRM agree well with those from BIOME-BGCv1 although both models are using different algorithms for calculating GPP and R_{eco}. GPP calculation in SDPRM is based on the MODIS17 algorithm which uses the light use efficiency logic suggested by Monteith (1977). In the MOD17 algorithm, VPD is the only variable directly related to environmental water stress, while both VPD and soil water content are used for water stress calculations in BIOME-BGCv1.

In figure 2.14, the seasonal cycles of R_{eco} from SDPRM and BIOME-BGCv1 are presented. As mentioned earlier, the parameters and the structure of the respiration model in SDPRM were chosen from the soil-respiration model of Reichstein et al. (2003) which was calibrated using field measurements from Europe and North America. The comparison in figure 2.13 shows that there are some differences in the amplitude of the seasonal cycle between the two models over Europe, North American Temperate and Boreal and Eurasian Boreal, but they agree well over the other regions. The two models agree perfectly over Eurasian

Temperate and the tropical regions. This is encouraging because it implies that SDPRM can produce flux fields over different regions of the globe consistent with the process-based estimates.

Based on the inter-comparison between SDPRM, BIOME-BGCv1 and the STDinv, we can conclude that our model is capable of reproducing realistic flux patterns comparable to the ones inferred from the atmospheric measurements or inferred based on process understanding. SDPRM has very simple structure and few adjustable parameters, and hence it is much easier to modify than more sophisticated process-based models. Accordingly, we assume that SDPRM is suitable to be coupled into the inverse model for the optimization of some internal model parameters. However, we should keep in mind that the real world is more complex than the models. The limitation of SDPRM can arise from

- The simplification of our model structure,

- The global application of the adjustable parameters, the initial values of which were derived from field studies,

- Deficiencies in the climate data (NCEP/NCAR),

- The limited resolution of the land cover classification, and

- The lack of some important processes (e.g. fire)

However, by coupling that model into the inversion, we expect that some of the model parameter can be optimized by the atmospheric constraints. Accordingly, more direct process understanding can be achieved that current atmospheric inversions do not provide.
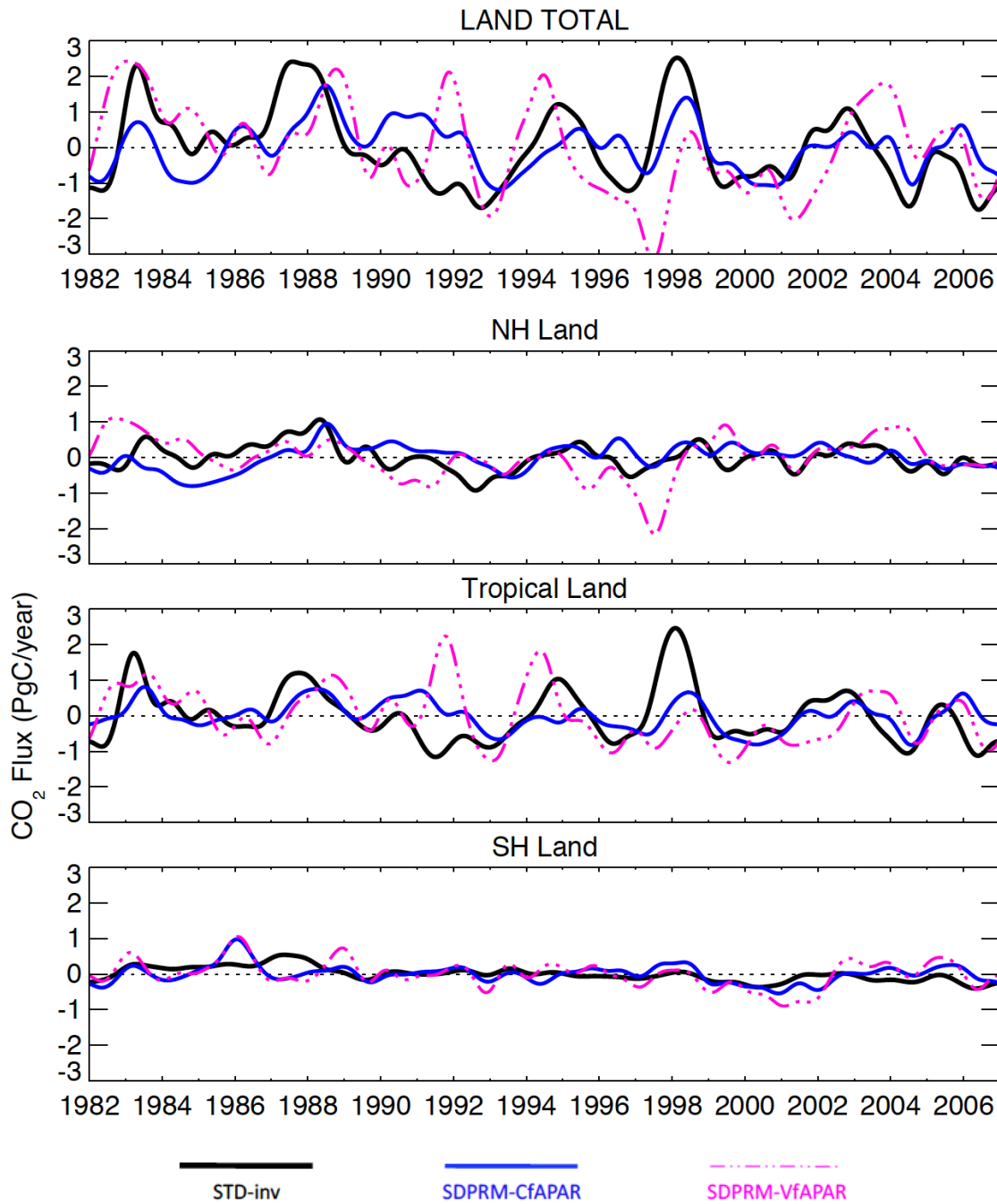
Figure 2.7— The comparison between the anomaly (subtracting the mean of 1982-2006) of the IAV of the simulated NEE from the two runs, CfAPAR (using the mean seasonal cycle of fAPAR) [Blue] and VfAPAR (using the full variability fAPAR) [Magenta dashed] and the total land flux simulated by STD-inv [Black]. The time series are integrated over three latitudinal bands (for the map of the regions see figure 2.4) and de-seasonalized and filtered for interannual variability (IAV) (as in Rödenbeck (2005)). The fossil fuel emissions have been subtracted for STD-inv line. Positive values denotes a net source of natural fluxes into the atmosphere.
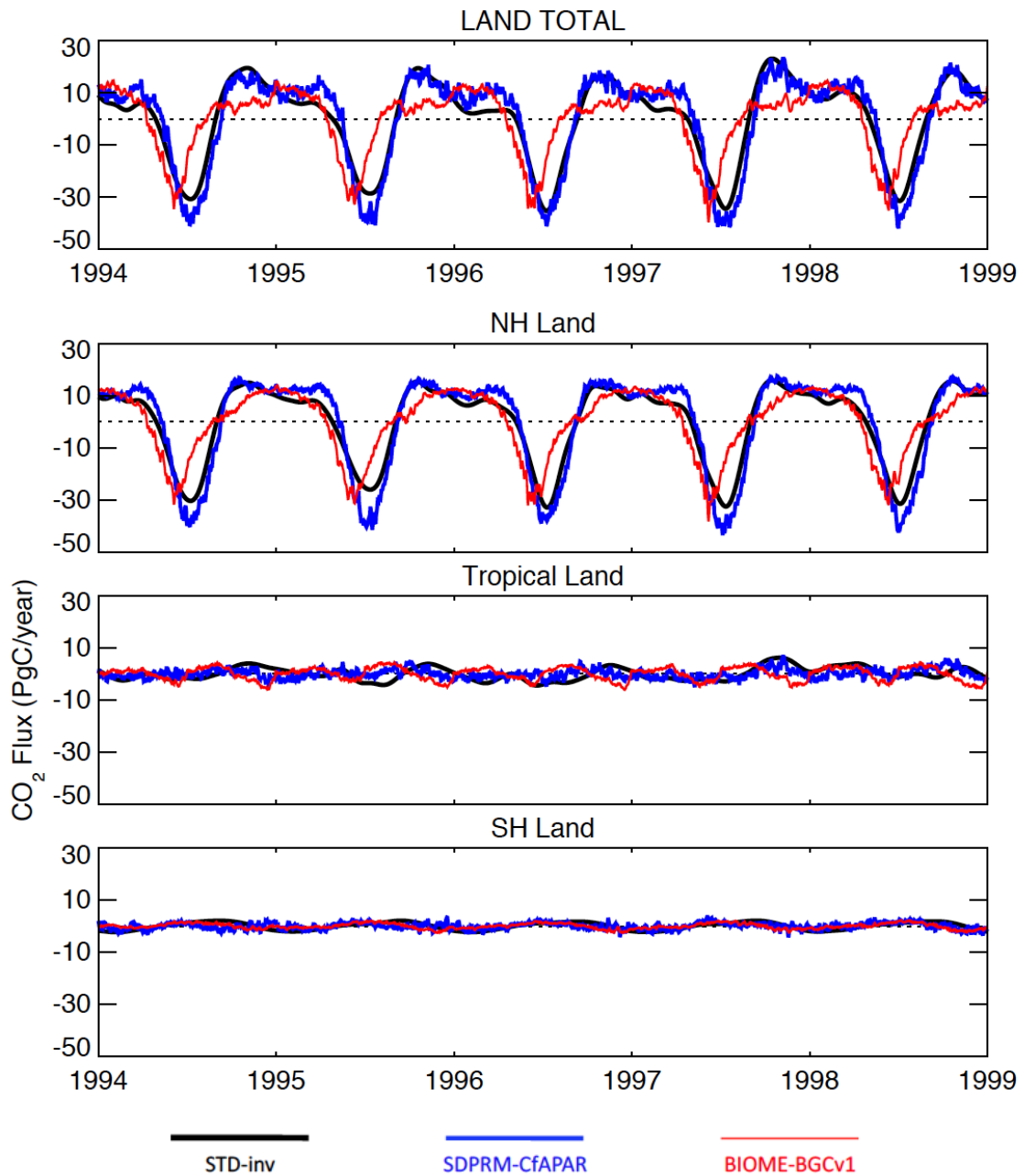
Figure 2.8— The comparison between the anomaly (subtracting the mean of 1982-2006) of the full variability of the simulated NEE from the CfAPAR run (using the mean seasonal cycle of fAPAR) [Blue], NEE estimates from BIOME-BGCv1 [Red] ,and the land flux simulated by STD-inv [Black]. The time series are integrated over three latitudinal bands (for the map of the regions see figure 2.4). The fossil fuel emissions have been subtracted from STD-inv line. Positive values denotes a net source of natural fluxes into the atmosphere.
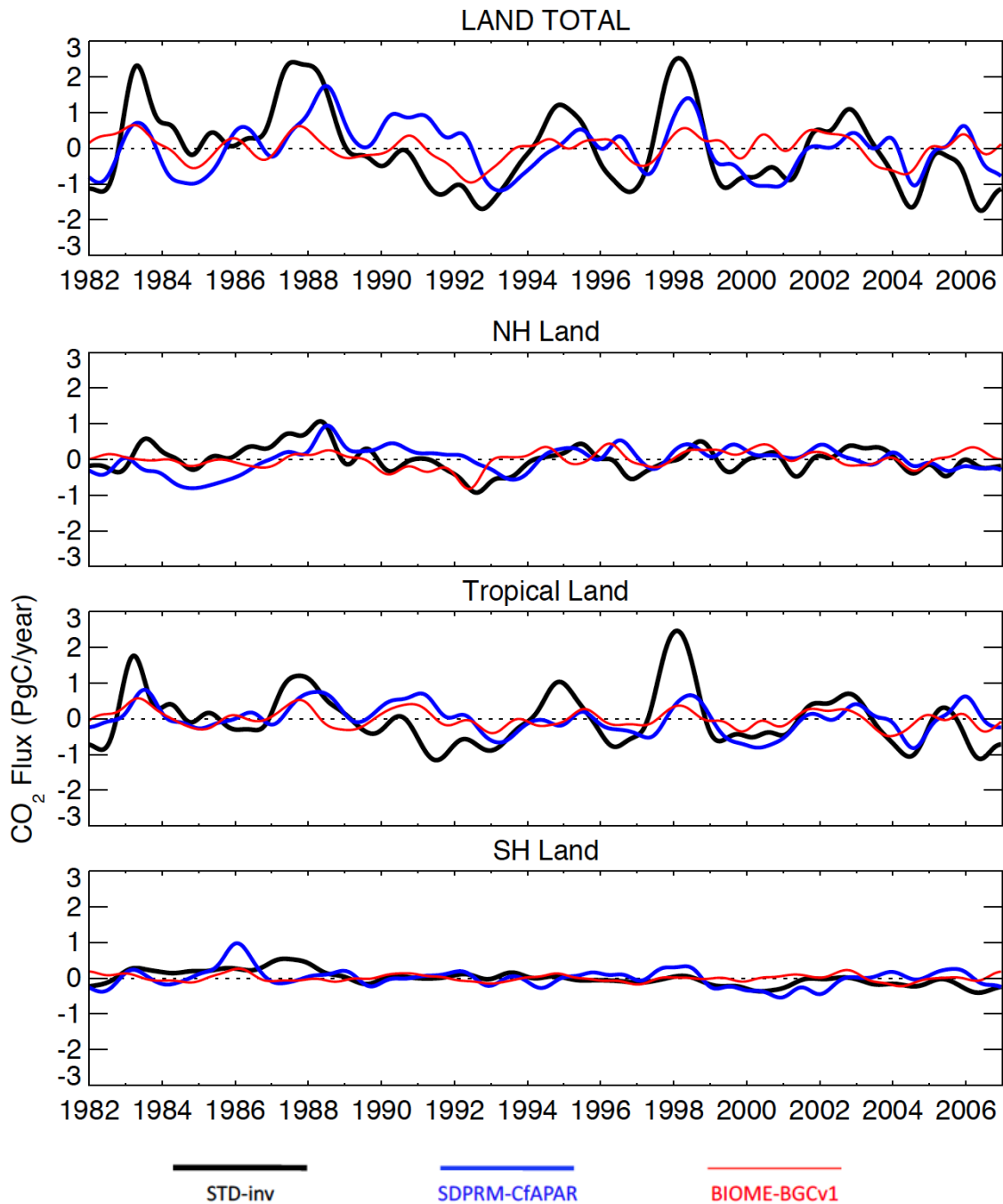
Figure 2.9— The same as figure 2.8 but for full variability of the land flux from STD-inv (Black), NEE from CfAPAR (Blue), and from BIOME-BGCv1 (red). The time series are de-seasonalized and filtered for interannual variability (IAV) (as in Rödenbeck (2005)). The fossil fuel emissions have been subtracted from STD-inv line. Positive values denotes a net source of natural fluxes into the atmosphere.
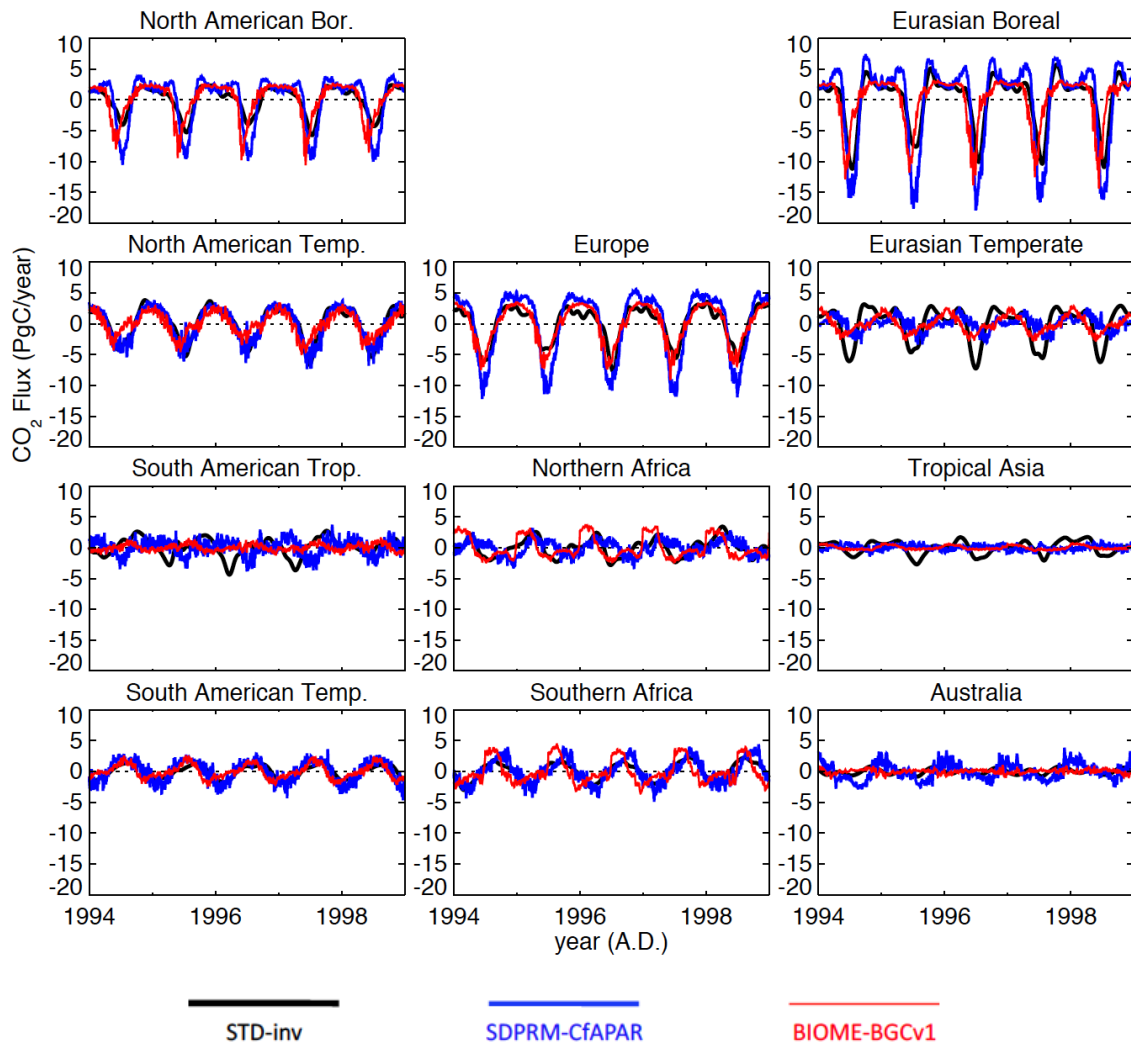
Figure 2.10— The same as figure 2.8 but the time series are integrated over 11 land regions (for the map of the regions see figure 2.4).
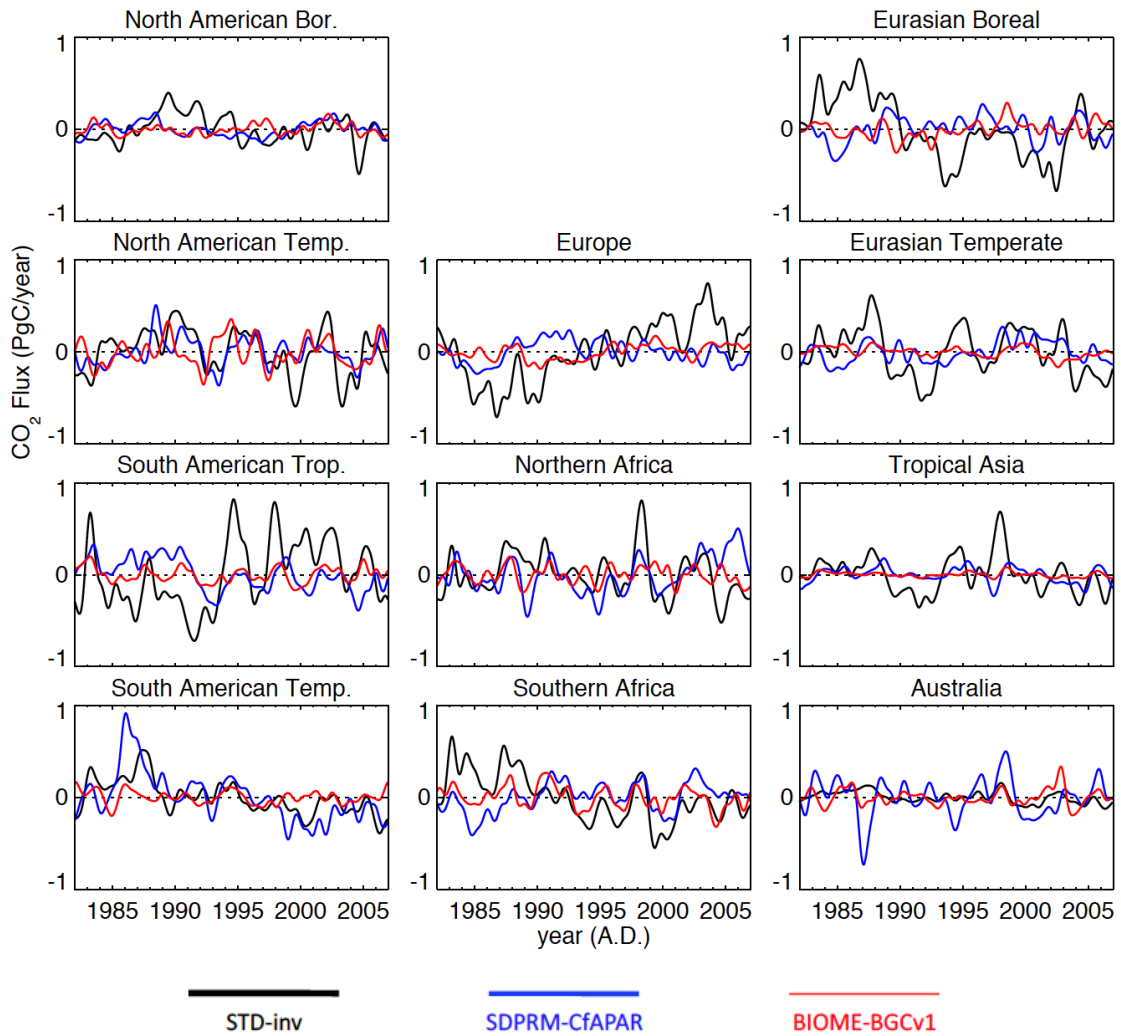
Figure 2.11—— The same as figure 2.9 but the time series are integrated over 11 land regions (for the map of the regions see figure 2.4).
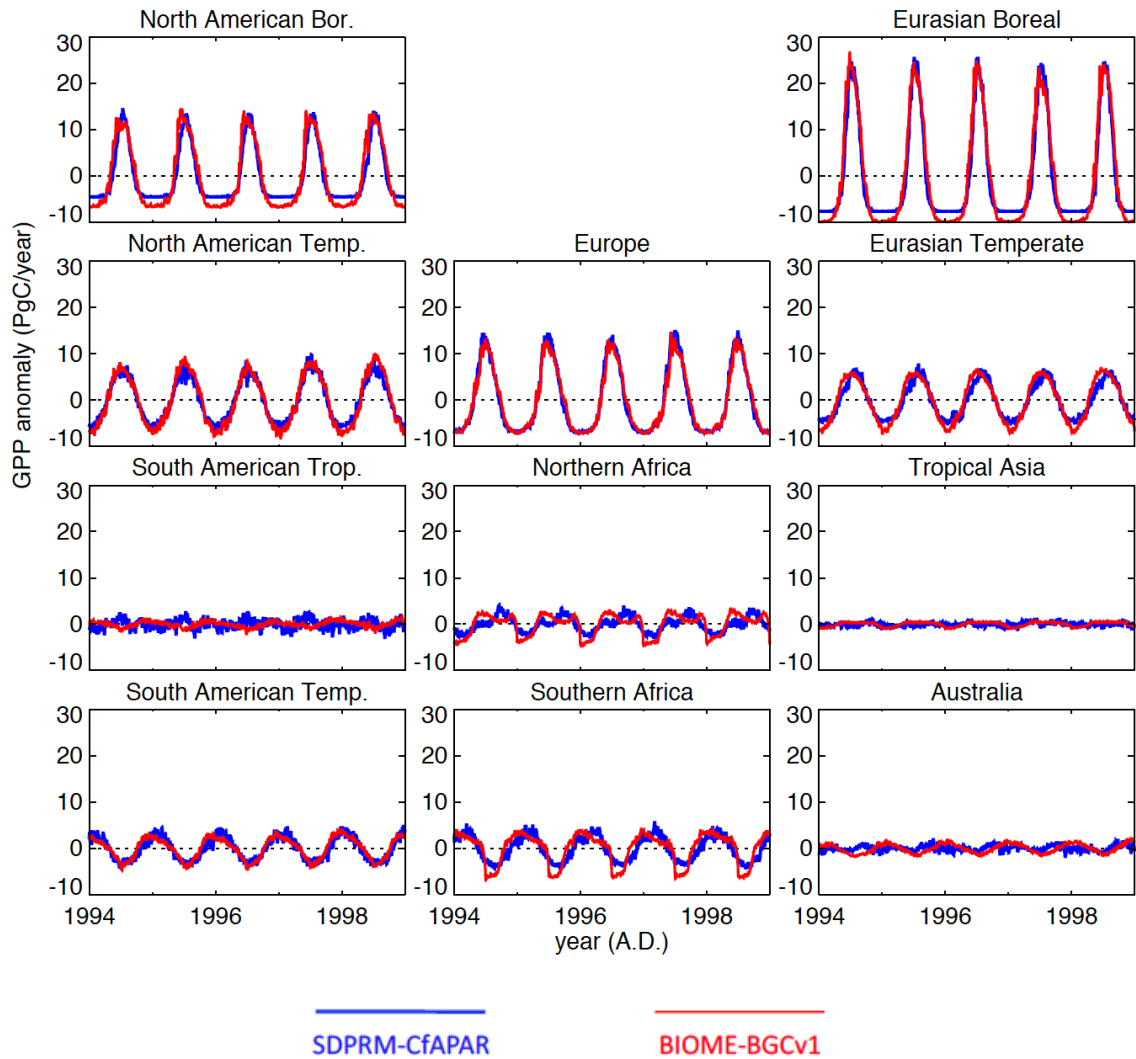
Figure 2.12— The comparison between the anomaly (subtracting the mean of 1982-2006) of the full variability of the simulated GPP from the CfAPAR run (using the mean seasonal cycle of fAPAR) [Blue], and from BIOME-BGCv1 [Red]. The time series are integrated over 11 land regions (for the map of the regions see figure 2.4).
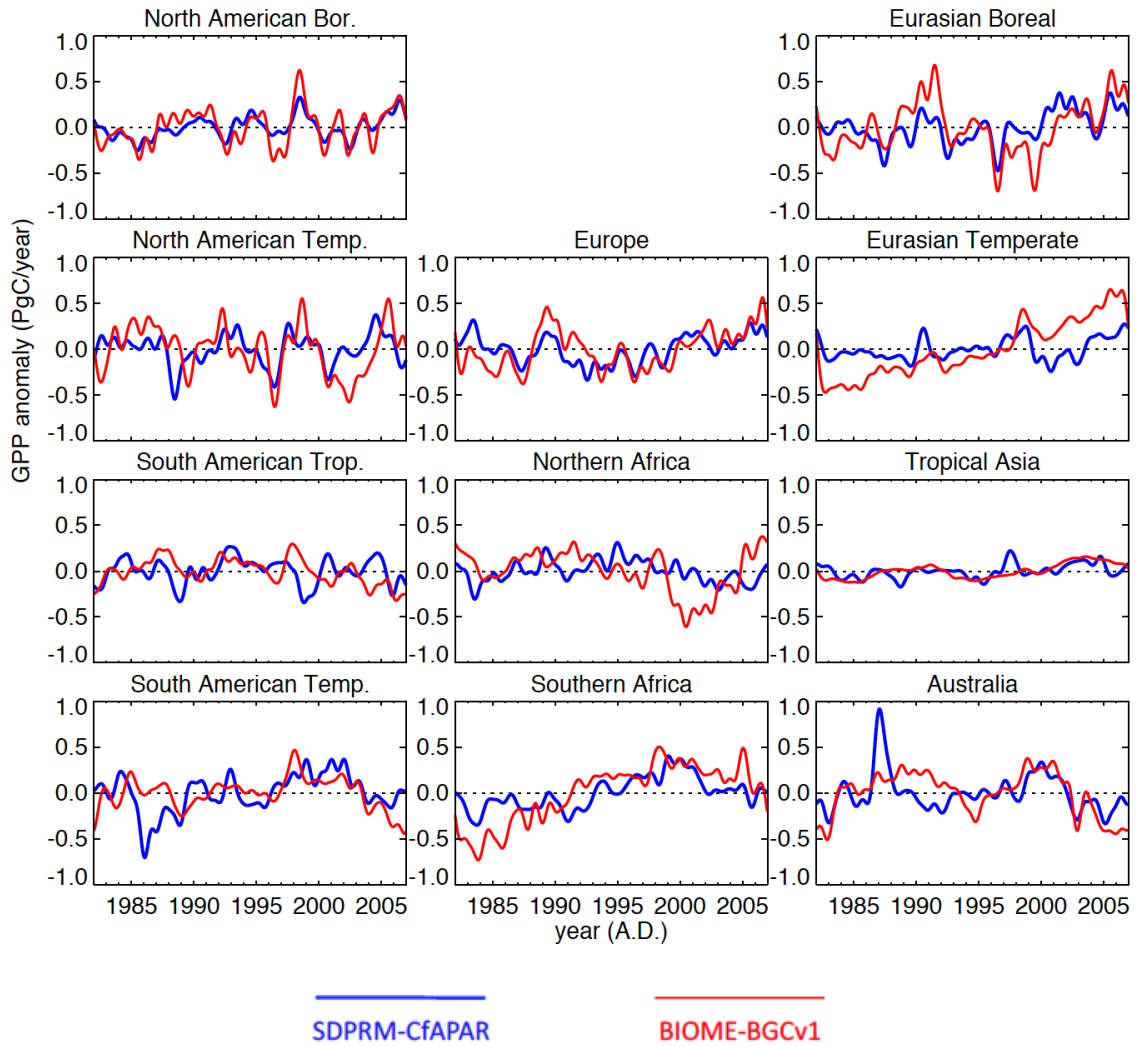
Figure 2.13— The comparison between the anomaly (subtracting the mean of 1982-2006) of the IAV of the simulated GPP from the CfAPAR run (using the mean seasonal cycle of fAPAR) [Blue], and from BIOME-BGCv1 [Red]. The time series are integrated over 11 land regions (for the map of the regions see figure 2.4) and de-seasonalized and filtered for interannual variability (IAV) (as in Rödenbeck (2005)).
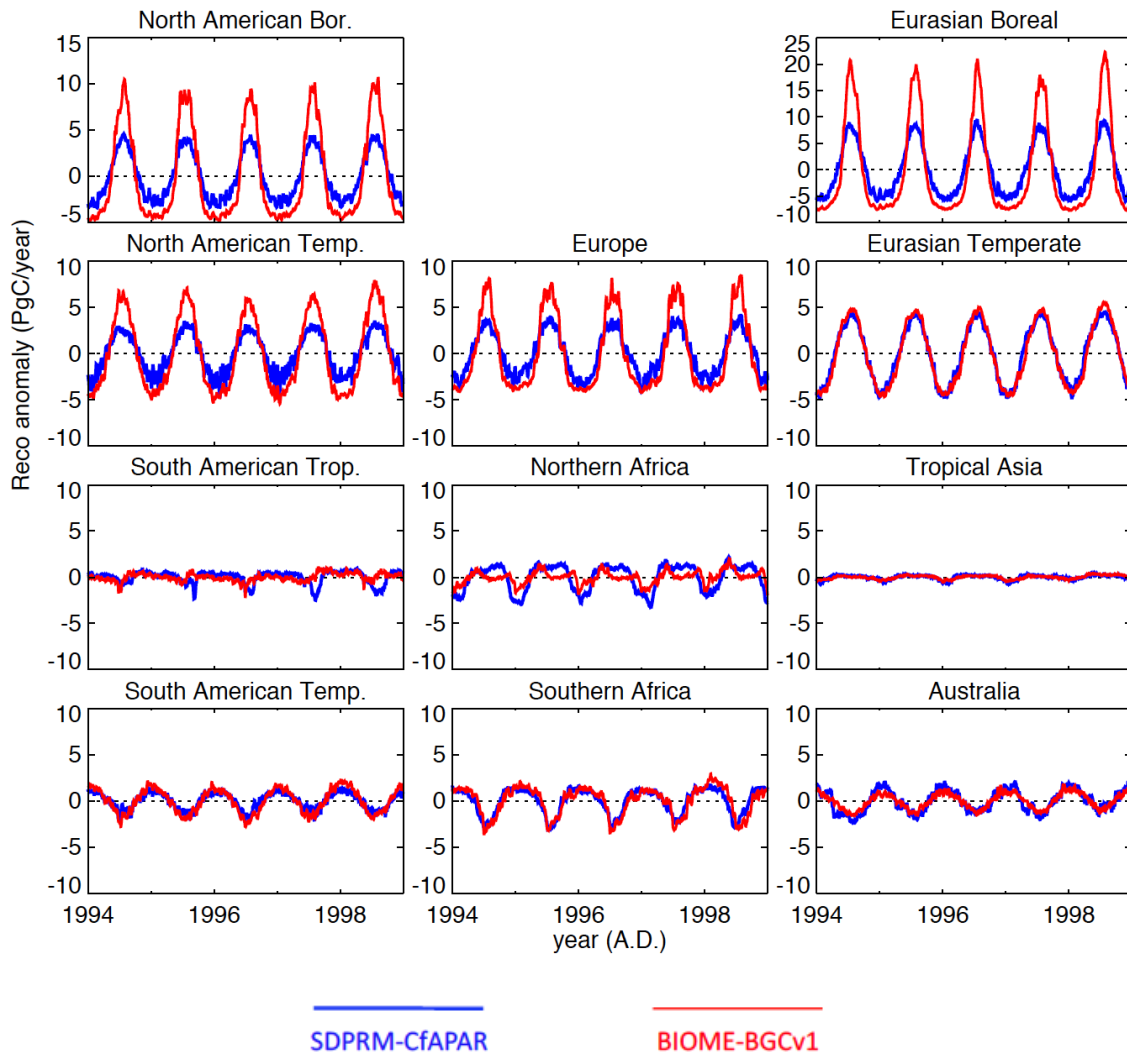
Figure 2.14— The comparison between the anomaly (subtracting the mean of 1982-2006) of the full variability of the simulated R_{eco} from the CfAPAR run (using the mean seasonal cycle of fAPAR) [Blue], and from BIOME-BGCv1 [Red]. The time series are integrated over 11 land regions (for the map of the regions see figure 2.4).
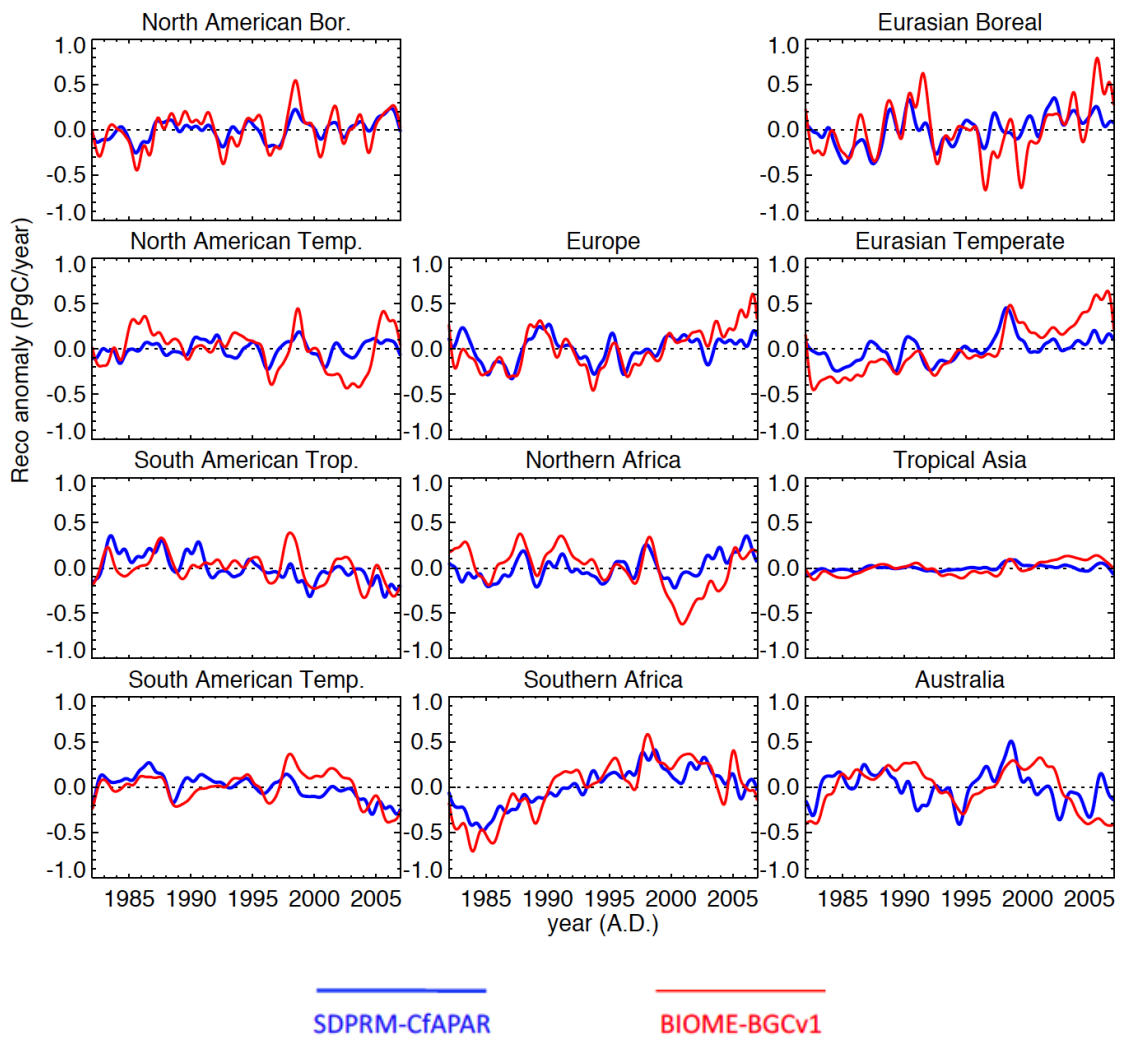
Figure 2.15— The comparison between the anomaly (subtracting the mean of 1982-2006) of the IAV of the simulated R_{eco} from the CfAPAR run (using the mean seasonal cycle of fAPAR) [Blue], and from BIOME-BGCv1 [Red]. The time series are integrated over 11 land regions (for the map of the regions see figure 2.4) and de-seasonalized and filtered for interannual variability (IAV) (as in Rödenbeck (2005)).

2.5.2 Experiment-2

Many studies have shown strong relationships between the annual climate (means) and vegetation distribution and ecosystem productivity (e.g Stephenson (1990) and others). They also show that any small variation in the annual climate can have a significant impact on the plant growth and biome stability. Thus, it seems reasonable to use the year-to-year variation (interannual variability (IAV)) of climate variables as indicators of the ecosystem productivity limitation.

In experiment-2, we tested the sensitivities of GPP and R_{eco} to the driving climate variables. This has been carried out by estimating the relative contribution of individual climate variables to the simulated interannual variability of GPP and R_{eco}.

We tested the effects of interannual variation in each climate variable by removing the IAV of the other climate variables (using only the mean seasonal cycle for the period 1982 to 2006) and using constant vegetation (mean seasonal cycle fAPAR). In the case of GPP, simulations allow for the isolation of the effects of daily minimum temperature (GT-only), vapor pressure deficit (GV-only), and downward short wave radiation (GS-only). In the case of R_{eco}, simulations allow isolation of the effects daily temperature (RT-only), and precipitation (RP-only). Then, the relative contribution of each independent climate variable on GPP and R_{eco} estimates (1982-2006) is calculated with a logic similar to the one suggested by Ichii et al. (2005) which can be expressed as:

$$GC_i = \frac{\sigma_i^2}{\sigma_{GT}^2 + \sigma_{GV}^2 + \sigma_{GS}^2} \tag{2.38}$$

$$RC_i = \frac{\sigma_i^2}{\sigma_{RT}^2 + \sigma_{RP}^2} \tag{2.39}$$

Here GC_i and RC_i are the proportional contribution of σ_i^2, the variance of anomalies in the simulated IAV of GPP and R_{eco} respectively, for each of the climate sensitivity simulations (i= GT-only, GV-only, GS-only, RT-only, or TP-only), to the sum of the variance of each of the climate sensitivity simulations . High/low GC_i or RC_i indicates large/small contribution of the climate simulation i on overall variance.

Based on the calculations of the squared correlation coefficient (R^2), we found that GPP and R_{eco} anomalies in the default simulation (CfAPAR – all climate variables are varying) were mostly explained by the sum of each climate sensitivity simulation (for GPP: GT-only + GV-only + GS-only and for R_{eco}: RT-only + RP-only) ($R^2 = 0.98$ for GPP and also for R_{eco}). This indicates that the main effects were essentially additive and that extensive

Table 2.6— Summary of the sensitivity runs (Experiment-2).

Acronym	Description
GPP-default	CfAPAR + Climate varying
GT-only	CfAPAR + Temperature only Varying + mean seasonal cycle of the other variables
GV-only	CfAPAR + VPD only Varying + mean seasonal cycle of the other variables
GS-only	CfAPAR + Radiation only Varying + mean seasonal cycle of the other variables
Reco-default	CfAPAR + Climate varying
RT-only	CfAPAR + Temperature only Varying + mean seasonal cycle of the other variables
RP-only	CfAPAR + Precipitation only Varying + mean seasonal cycle of the other variables

non-linear interactions do not exist. Therefore, non-linear responses of GPP and R_{eco} to interactions among climate variables (e.g. simultaneous increase in temperature and radiation) were not investigated.

Climate Controls on GPP

Based on equation 2.38, figure 2.20 shows the global distribution of the relative contribution of each climate variable (temperature, vapor pressure deficit, and radiation) to the IAV of GPP. Also, the time series of the integrated IAV of GPP for simulation in which all climate variables varied (GPP-default) and in which only a single climate variable (GT-only, GV-only, and GS-only) are shown in figures 2.16 and 2.17 and summarized in table 2.7 for different eco-regions . The results of the relative contribution of each climate factor to GPP are summarized as follow:

1. ***Temperature:***
   In the high latitudes, temperature is clearly the primary control on GPP (figure 2.20), in particular over the North American boreal forest and Eurasian boreal forest (77% and 63%, respectively) and to a lesser extent over Europe and the Eurasian temperate forest (27% and 13%, respectively, see table 2.7). On average, temperature limits GPP over the northern hemisphere by almost 43%. But on the other hand, the tropics and the southern hemisphere areas are not limited by low temperature (less than 2%). This can be explained by the fact that at low temperatures the enzymes responsible for photosynthesis have very little energy so the rate of photosynthesis is very slow. Thus, very low mean annual temperatures limit plant productivity as in the case of tundra and boreal forests in northern latitudes. Similar findings were presented by Nemani et al. (2003). In this study, they investigated vegetation responses to climatic changes by analyzing 18 years (1982 to 1999) of both climatic data and satellite observations of vegetation activity. According to their study, cold winter temperatures limit high-latitude Eurasian vegetation, while tropical areas

are never limited by low temperatures. Figures 2.16 and 2.17 show that over the northern hemisphere, in particular over the boreal regions, the IAV of GPP when only the temperature varied (GT-only) is similar to the IAV of GPP-default.

2. ***Vapor pressure deficit:***
As mentioned earlier, in the MOD17 algorithm for calculating GPP, VPD is the only variable directly related to environmental water stress. Therefore, VPD is used as an indicator of environment water stress.

It is clear from figure 2.20 that VPD is a dominant control on GPP over large areas of the globe where water is severely limited, mainly Australia (91%), North and South American temperate forest (77% and 76%, respectively), southern Africa (76%), southern Europe (56%), and the Sahara desert (58%) (see table 2.7). This also can be seen in figures 2.16 and 2.17 where the IAV of GPP when only the VPD varied (GV-only) is in good agreement with the IAV of GPP-default over different part of the globe, in particular in the water-limited regions (e.g. temperate forest in North America, Australia, and India). This is also consistent with the finding of Nemani et al. (2003) who estimated that water availability most strongly limits vegetation growth over 40% of the Earth's vegetated surface, and vapor pressure deficit (VPD) is a limiting factor of vegetation growth in water-limited ecosystems of Australia, Africa, and the Indian subcontinent.

3. ***Radiation:***
Radiation is another important limiting factor on GPP, because photosynthesis occurs only in the presence of a sufficient amount of light. Intense cloud cover could dramatically reduce the incoming solar radiation. According to that, we can see from figure 2.20 that radiation limits GPP by almost 56% over the area covered most of the year by cloud (tropical regions). But radiation is also a limiting control on GPP, over some areas in the northern hemisphere, such as Eurasian temperate (39%), Europe (17%), and north American temperate (14%), but with a lesser degree . Nemani et al. (2003) also found that radiation is a limiting factor in western Europe and the equatorial tropics regions.

Climate Controls on R_{eco}

Similarly, based on equation 2.39, figure 2.21 shows the global distribution of the relative contribution of each climate variable (temperature, precipitation) to the interannual variability of R_{eco}. Also, the time series of the integrated IAV of R_{eco} driven by fully-varying climate data (R_{eco}-default) and cases in which only one variable varied (RT-only

Table 2.7— Climatic contributions to the interannual variability of GPP and R_{eco} over different land regions. The contribution was calculated using equations 2.38 and 2.39

.

	GPP			R_{eco}	
Land Regions	VPD	Radiation	Temperature	Precipitation	Temperature
Land Total	0.43	0.39	0.18	0.32	0.68
Northern Hemisphere	0.47	0.10	0.43	0.13	0.87
Tropical Land	0.44	0.56	0.00	0.51	0.49
Southern Hemisphere	0.89	0.09	0.02	0.83	0.17
North American Bor.	0.17	0.05	0.77	0.02	0.98
North American Temp.	0.77	0.14	0.09	0.40	0.60
South American Trop.	0.46	0.53	0.00	0.74	0.26
South American Temp.	0.76	0.21	0.03	0.68	0.32
Europe	0.56	0.17	0.27	0.14	0.86
Northern Africa	0.58	0.42	0.00	0.62	0.38
Southern Africa	0.76	0.24	0.00	0.91	0.09
Eurasian Boreal	0.28	0.10	0.63	0.10	0.90
Eurasian Temperate	0.53	0.34	0.13	0.45	0.55
Tropical Asia	0.11	0.89	0.00	0.55	0.45
Australia	0.91	0.09	0.01	0.88	0.12

and RP-only) are shown in figures 2.18 and 2.19 for different eco-regions. Additionally, the calculated values based on equation 2.39 for different regions are shown in table 2.7. The results of the relative contribution of each climate factor to R_{eco} are summarized as follow:

1. **Temperature:**

   Similar to GPP, temperature partially determines the respiration rates of vegetation. Consequently, plants growing in cold regions are usually less productive. Thus, R_{eco} of plants from cold regions is primarily limited by temperature. Figure 2.21 shows that clearly, where temperature limits R_{eco} by almost 87% over the northern hemisphere and by a lower rate over tropical regions (49%). This is also clear in figures 2.18 and 2.19 where the time series of the IAV of R_{eco} simulated by RT-only and R_{eco}-default are shown.

2. **Precipitation:**

   Figure 2.21 shows that precipitation is a dominant control on R_{eco} over large areas of the globe where water is severely limiting, in particular the tropics and southern hemisphere regions (51% and 83% respectively).
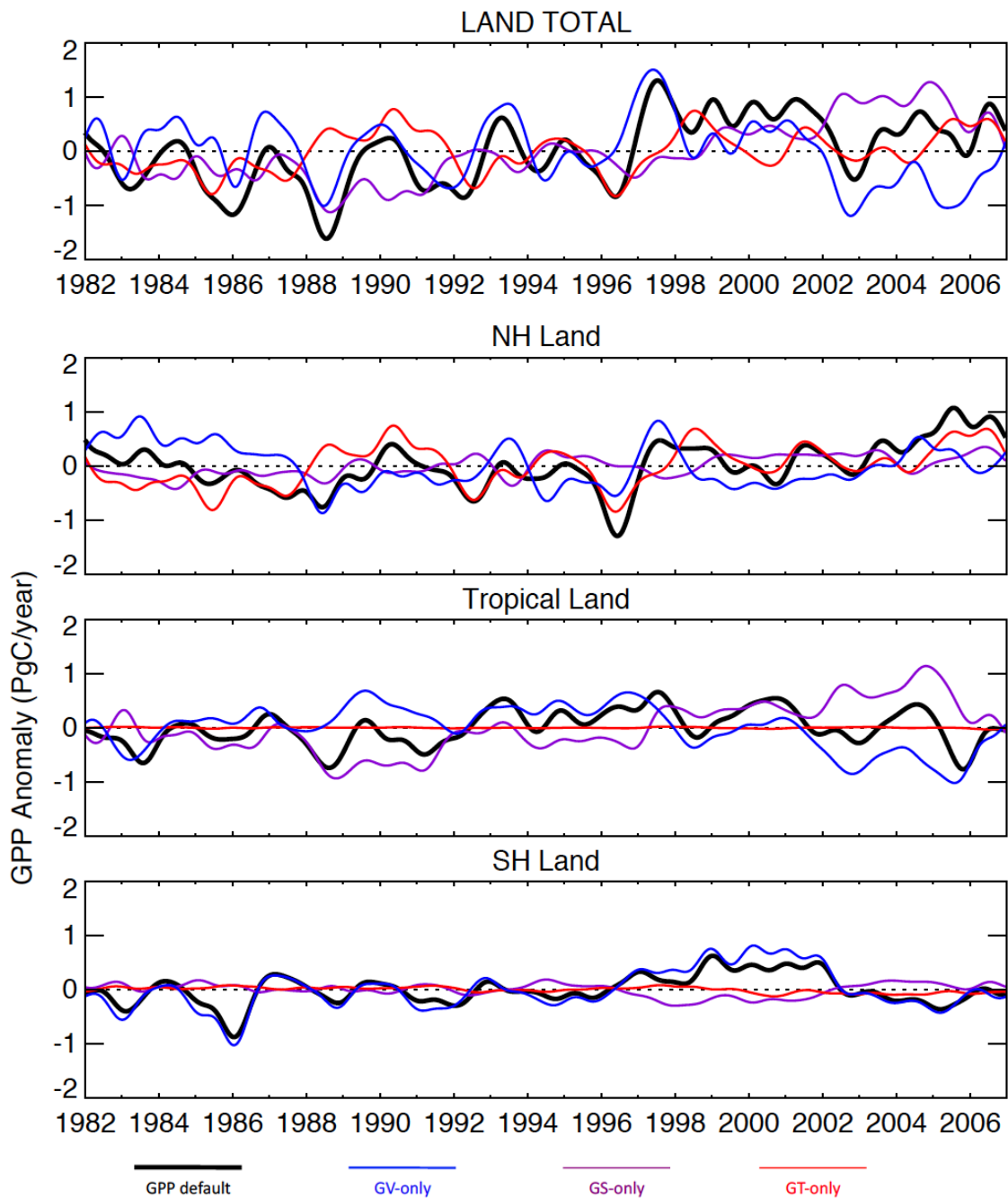
Figure 2.16— The comparison between the anomalies (subtracting the mean of 1982-2006) of the IAV of the simulated GPP: GPP-default (Black), GV-only (Blue), GT-only (Red), and GS-only (violet) (see table 2.6) . The time series are integrated over three latitudinal bands (for the map of the regions see figure 2.4) and de-seasonalized and filtered for interannual variability (IAV) (as in Rödenbeck (2005)).
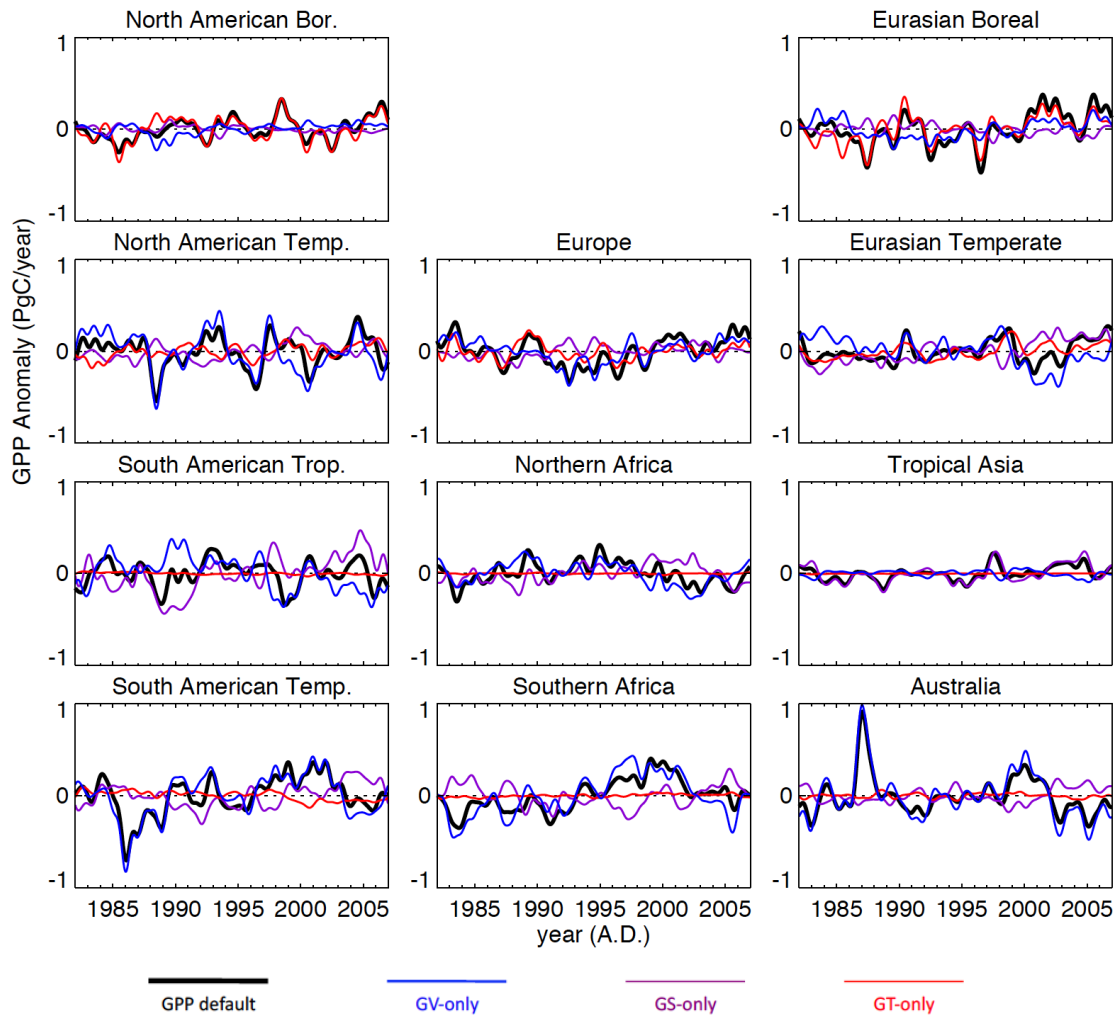
Figure 2.17— As in figure 2.16, but the time series are integrated over 11 land regions (for the map of the regions see figure 2.4)
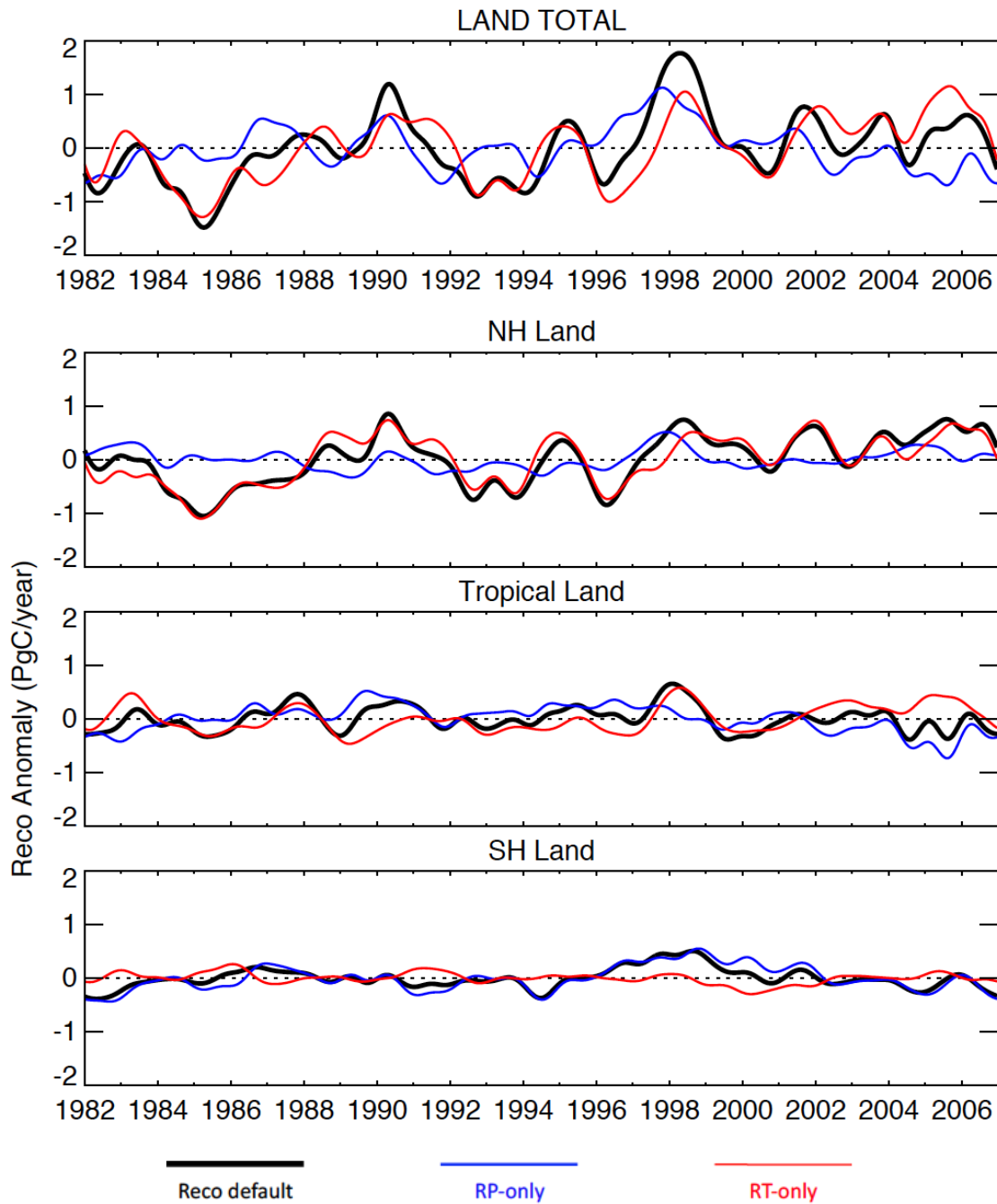
Figure 2.18— The comparison between the anomalies (subtracting the mean of 1982-2006) of the IAV of the simulated R_{eco} fluxes : R_{eco}-default (Black), RP-only (Blue), and RT-only (Red)(see table 2.6). The time series are integrated over three latitudinal bands (for the map of the regions see figure 2.4) and de-seasonalized and filtered for interannual variability (IAV) (as in Rödenbeck (2005)).
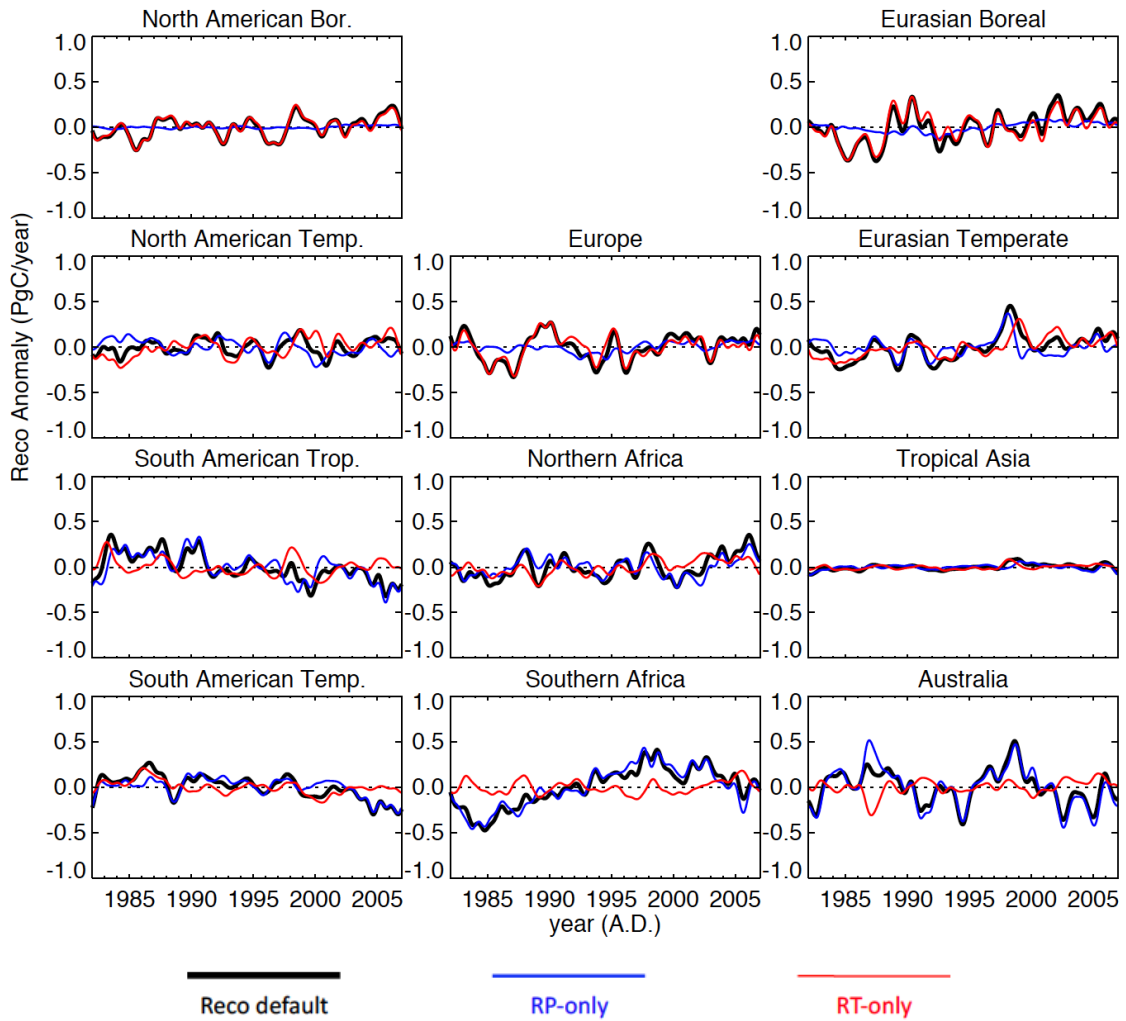
Figure 2.19— As in figure 2.16, but the time series are integrated over 11 land regions (for the map of the regions see figure 2.4)
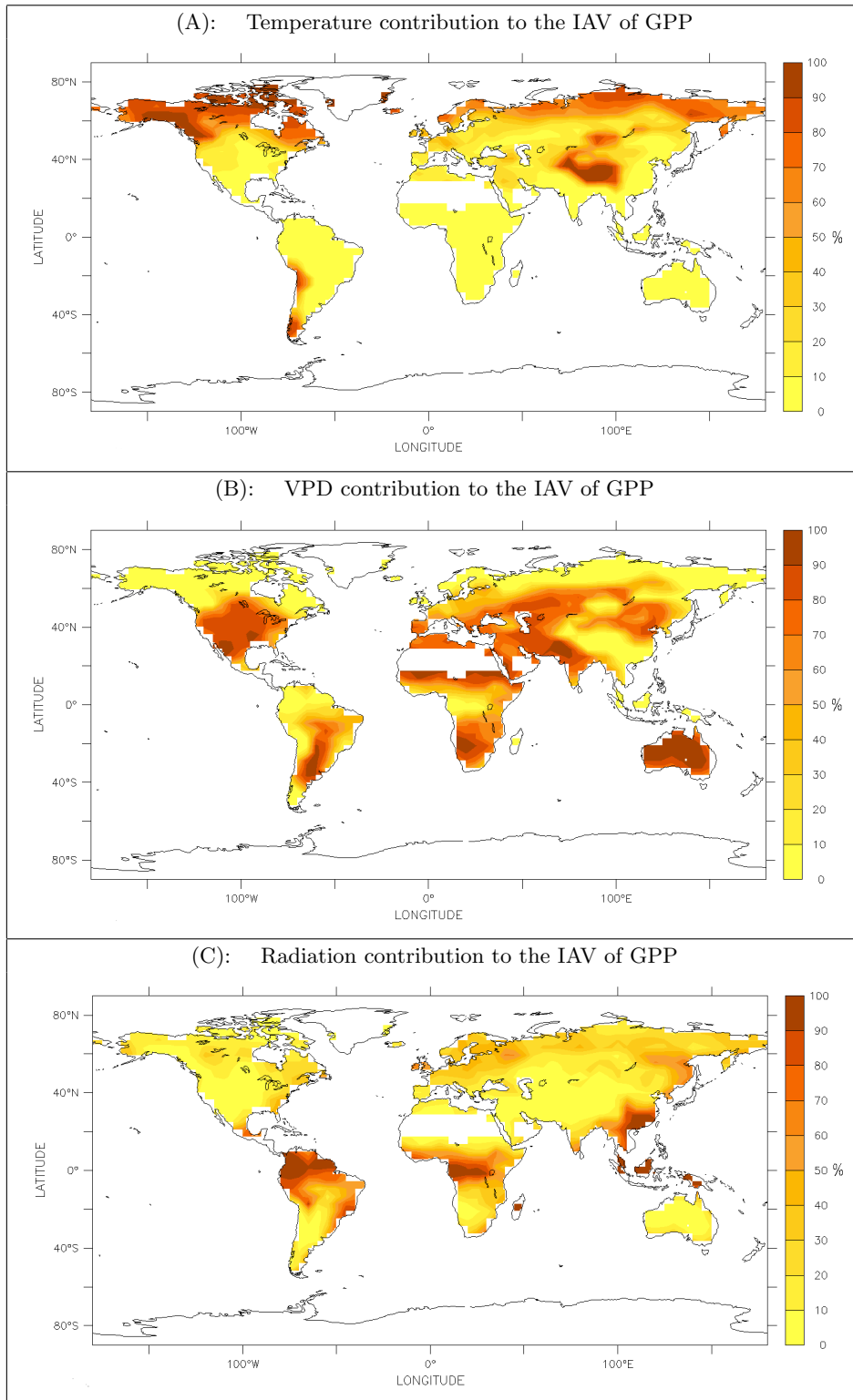
Figure 2.20— The global distribution of the relative contribution of each climate variable (temperature (A), vapor pressure deficit (B), and radiation (C)) to the IAV of GPP.
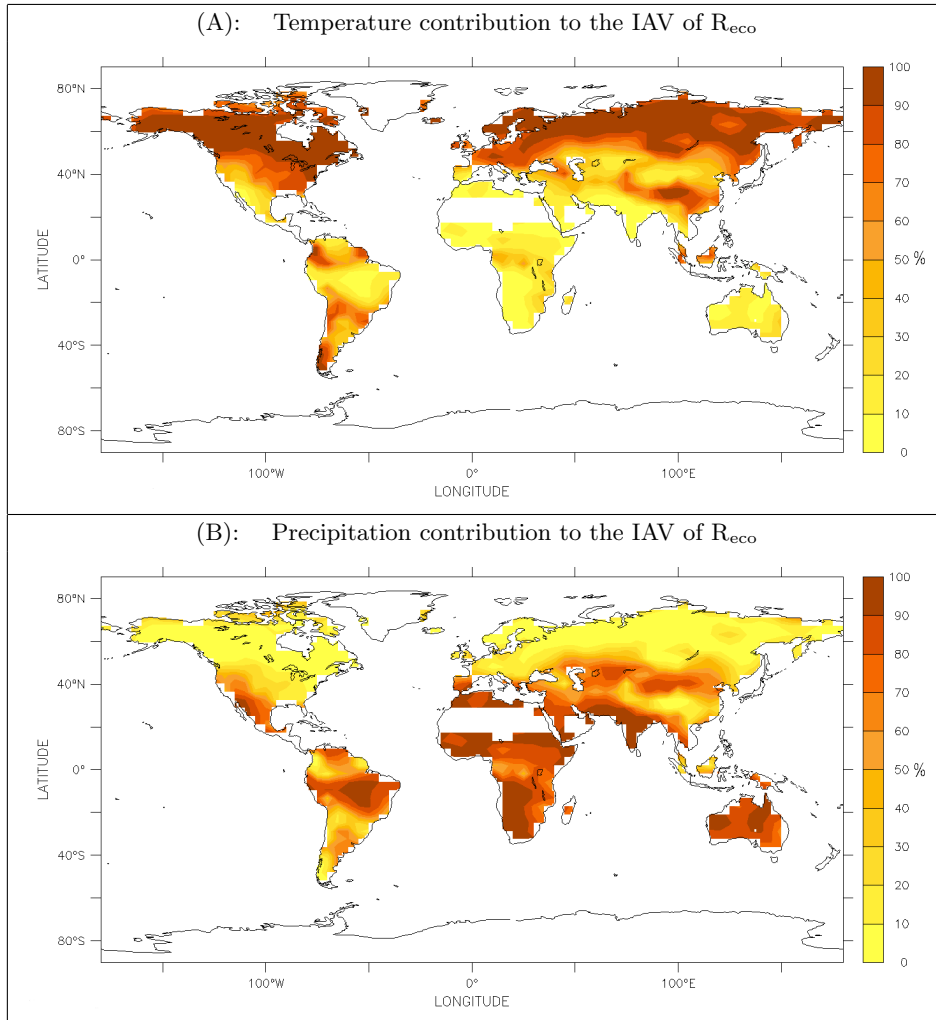
Figure 2.21— The global distribution of the relative contribution of each climate variable (temperature (A), precipitation (B)) to the IAV of R_{eco}.

2.5.3 Summary and Conclusion

In this chapter, we presented the algorithm that is used to implement the Simple Diagnostic Photosynthesis and Respiration Model (SDPRM). The model estimates 3-hourly values of Gross Primary Production (GPP) and daily values of ecosystem respiration (R_{eco}) . The spatial resolution of the model is $4°$ latitude $\times$ $5°$ longitude. The model is driven by climate data from NCEP/NCAR and satellite-derived fAPAR data.

To test the performance of the model, we compared simulated carbon flux components with two different approaches for estimating the land fluxes. One approach is the process-understanding approach presented by the BIOME-BGCv1 model. The second approach is the atmospheric CO_2 inversion in which the land fluxes are inferred from the atmospheric information. We used the results of an updated version of the standard inversion (STD-inv) presented by Rödenbeck (2005).

The main conclusions are:

- The interannual variability of NEE is mainly driven by climate. That means modeling ecosystem productivity using climatological fAPAR and varying climate data would produce a reasonable match to the inversion results and to the process-based models.

- SDPRM is capable of reproducing realistic flux patterns comparable to the ones inferred from the atmospheric measurements or inferred based on process understanding.

- Accordingly, we assume that SDPRM is suitable to be coupled into the inverse model in order to optimize some selected model parameters.

Furthermore, we have tested the sensitivities of GPP and R_{eco} to the driving climate variables. This has been carried out by estimating the relative contribution of individual climate variables to the simulated interannual variability of GPP and R_{eco}. The results of the sensitivity analyses were consistent with the finding of Nemani et al. (2003). The main conclusions are:

- Temperature controls the IAV of GPP over cold boreal forest.

- VPD controls the IAV of GPP in water-limited ecosystems.

- Radiation is the main control of the IAV of GPP over the tropical regions.

- Temperature controls the IAV of R_{eco} over large areas of the globe, in particular over northern hemisphere regions.

- Also, precipitation controls the IAV of R_{eco} over large areas of the globe, in particular over the tropics and southern hemisphere regions.

By coupling SDPRM to the inverse model, we expect that some of the model parameters can be optimized by the atmospheric measurements. Accordingly, more direct process understanding can be achieved, which currently STD-inv does not provide.

Chapter 3

Atmospheric CO_2 Inversion

For the purpose of this chapter, it is useful to recall briefly what has been achieved in chapter 2. As described in chapter 2, SDPRM calculates the Gross Primary Production (GPP) and the Ecosystem Respiration (R_{eco}) independently. The model is driven by the fraction of Absorbed Photosynthetically Active Radiation (fAPAR) and climate data and uses few adjustable parameters. To test the performance of the model, the simulated fluxes have been compared with the flux estimates from two different approaches; a process-based modeling approach represented by BIOME-BGCv1 and the atmospheric inversion approach represented by the inverse model introduced by Rödenbeck et al. (2003) and its extension, described by Rödenbeck (2005) (referred to as STD-inv introduced in this chapter). Based on the comparisons, SDPRM shows its capability to produce flux estimates consistent with the estimates from the other two approaches, suggesting that SDPRM can provide reasonable a-priori CO_2 fluxes for the inverse model application.

In this chapter, we aim to infer carbon sources and sinks of the land biosphere using different modeling approaches and data constraints. Therefore, SDPRM is coupled to STD-inv (referred to as SDPRM-inv). SDPRM replaces the simple statistical linear flux model of STD-inv (described in section 3.1.1) for different aims: first, to provide reasonable a-priori CO_2 fluxes with high spatio-temporal resolution to STD-inv, second, to optimize some internal physiological and interpretable parameters of SDPRM in order to fit the atmospheric measurements of CO_2. For the coupling, SDPRM is linearized around the adjustable parameters (see section 3.2) in order for the minimization algorithm to work more efficiently. From the coupled system, we can learn which of these parameters can be constrained by the CO_2 measurements. Accordingly, we can understand the model behavior and define strategies for further assimilation experiments.

In STD-inv, special care has been taken to overcome of the shortcoming of previous studies:

(1) avoiding spurious variability due to data gaps by selecting homogeneous data records, (2) avoiding spatial rectification biases by solving for higher-resolved fluxes correlated in time and space (this problem will not be relevant in the coupled system, see remark in section 3.2.3), (3) reducing model errors by using time-varying meteorological drivers and consistent representation of data sampling in the model (i.e., sampling of the model at the same time and location as the observations) rather than monthly mean concentrations as in many inversion studies (e.g. Kaminski et al. (2002)). Also, the time resolution of the fluxes was increased to daily flux values.

In the following sections, we briefly describe: (1) the mathematical algorithm of STD-inv, in particular the construction of the statistical linear flux model, (2) the atmospheric CO_2 data and atmospheric transport model used in this study and (3) the implementation details of the coupled system (SDPRM-inv).

3.1   Overview of STD-inv

In principle, the inverse modeling technique is used to estimate CO_2 fluxes at a variety of spatial and temporal scales using a combination of various sources of information. The primary source of information is observed atmospheric CO_2 concentrations at a set of sites. Global observational networks provide concentration measurements of atmospheric CO_2 at only around 100 sites. However, they accurately measure gradients in CO_2 concentrations between two different points of the globe, reflecting the distribution of the surface fluxes dispersed by transport in the atmosphere (Keeling et al., 1989; Tans et al., 1990). Atmospheric tracer transport is linear, therefore a model of atmospheric transport can be used in an inverse mode if the source and sink distribution are to be inferred from observed concentrations. The transport model simulates how the atmospheric circulation moves the trace gas by advection, diffusion and convection. Therefore the modeled atmospheric CO_2 concentrations, $\mathbf{c_{mod}}$, that arise from a given temporally and spatially varying discretized flux field, $\mathbf{f}$, are computed by an atmospheric transport model as:

$$\mathbf{c}_{\mathrm{mod}} = \mathbf{A}\mathbf{f} + \mathbf{c}_{\mathrm{ini}} \tag{3.1}$$

with an initial concentration, $\mathbf{c}_{\mathrm{ini}}$, which is assumed fixed and corresponds to a well-mixed atmosphere (i.e., all elements of the vector $\mathbf{c}_{\mathrm{ini}}$ are equal. A is a transport operator that maps fluxes onto atmospheric concentrations. The dimensions of the matrix A are the number of flux components times the number of observables. The values in $\mathbf{c}_{\mathrm{mod}}$ are sampled in the model for every individual time and location where there is a measured value in $\mathbf{c}_{\mathrm{meas}}$.

The inversion calculation seeks those fluxes $\mathbf{f}$ that lead to modeled concentration values that should be as close as possible to the actual measured concentrations, taking into account measurement and model errors. The desired result, the so-called a posteriori flux estimate, is then obtained by minimizing the following cost function:

$$J_c = \frac{1}{2}(\mathbf{c}_{\mathrm{meas}} - \mathbf{c}_{\mathrm{mod}})^T \mathbf{Q}_\mathrm{c}^{-1}(\mathbf{c}_{\mathrm{meas}} - \mathbf{c}_{\mathrm{mod}}) \tag{3.2}$$

where the covariance matrix $\mathbf{Q}_\mathrm{c}$ introduces a weighting among the concentration values.

Since the number of sampling sites is limited, the matrix A becomes a rectangular matrix with a much larger number of columns than rows. In this case the inverse problem is highly underdetermined which means that there are many flux fields yielding the same modeled concentrations at the observational sites (Kaminski and Heimann, 2001). This problem can be partially solved by using a Bayesian approach that includes a-priori information about land and ocean fluxes in the inversion calculation. Both atmospheric CO_2 observations and a-priori fluxes are described in terms of Gaussian probability densities. Following the inversion algorithm introduced by Rödenbeck et al. (2003) and Rödenbeck (2005), the deviation from the a-priori fluxes are structured by introducing a linear statistical flux model (more details in the next section). Briefly, this flux model defines the a-priori probability distribution of the fluxes $\mathbf{f}$ around the mean $\mathbf{f}_{\mathrm{fix}}$ (the first-guess) according to:

$$\mathbf{f} = \mathbf{f}_{\mathrm{fix}} + \mathbf{F}\mathbf{p} \tag{3.3}$$

where the matrix $\mathbf{F}$ represent a series of spatial-temporal flux patterns composing the total flux. The vector $\mathbf{p}$ represents the set of adjustable parameters, each of which acts as a multiplier to one of the columns of the matrix $\mathbf{F}$. The a-priori covariance matrix of the fluxes is $\mathbf{Q}_{\mathbf{f}_{\mathrm{pri}}} = \mathbf{F}\mathbf{F}^{\mathrm{T}}$. By considering the a-priori information in equation 3.2, the cost function J, to be minimized with respect to $\mathbf{p}$, can be written as:

$$J = J_c + \frac{1}{2}\mathbf{p}^{\mathrm{T}}\mathbf{p} \tag{3.4}$$

where the a-priori parameters vector $\mathbf{p}$ has zero mean, unit variance and is uncorrelated. The minimization of the cost function J with respect to the parameters $\mathbf{p}$ has been done using a Conjugate Gradients algorithm with re-orthogonalization after each step (Rödenbeck, 2005).

3.1.1 The linear flux model of STD-inv

Referring to equation 3.3, the flux model introduces all a-priori information in the inversion calculation. The total flux, $\mathbf{f}$, is considered as the sum of N_{comp} different source and sink components (Rödenbeck, 2005):

$$\mathbf{f} = \sum_{i=1}^{N_{comp}} (\beta_i \mathbf{f}_{\text{fix},i} + \alpha_i \mathbf{F}_i \mathbf{p}_i) \tag{3.5}$$

where i is the index of source and sink components. In STD-inv, the individual flux components correspond to: (1) fossil fuel emission, (2) land-atmosphere carbon exchange and (3) ocean-atmosphere carbon fluxes. In general, the total flux can be expressed by fixed ($f_{fix,i}(x,y,t)$) and adjustable terms. The flux model can then be written in a 3D field $f(x,y,t)$ as:

$$f(x,y,t) = \sum_{i=1}^{N_{Comp}} \left(\underbrace{\beta_i f_{fix,i}(x,y,t)}_{fixed} + \underbrace{\alpha_i f_{sh,i}(x,y,t) \sum_{m_t}^{N_{t,i}} \sum_{m_s}^{N_{s,i}} g_{m_t,i}^{time}(t) g_{m_s,i}^{space}(x,y) p_{m_t,m_s,i}}_{\delta f_i(x,y,t)\ adjustable} \right) \tag{3.6}$$

where, $f_{sh,i}(x,y,t)$ represents a weighting in space and time that defines the domain of activity of the flux component, while $\{g_{m_t,i}^{time}(t)\}$ and $\{g_{m_s,i}^{space}(x,y)\}$ determine a temporal and spatial, respectively, decomposition into statistically independent elements. In other words, it introduces temporal and spatial correlations among source strengths. β and α are scaling factors. The individual adjustable parameters $p_{m_t,m_s,i}$ determine the relative strength of all combinations of elements. Detailed explanations of these various quantities are described in (Rödenbeck, 2005).

3.1.1.1 Fixed and adjustable terms of STD-inv

Under the framework of STD-inv the following settings are considered:

- The fixed terms, $f_{fix,i}(x,y,t)$, (a-priori flux fields) do not have year-to-year variations. That means the variability found in the estimated fluxes are explained by the atmospheric information. This is a slightly different view than the classical Bayesian interpretation of $f_{fix,i}(x,y,t)$ being an a-priori "best guess" flux estimate and the adjustable term just being its error. Therefore, in STD-inv, the adjustable term play

the role of the actual flux component, while $f_{fix,i}(x, y, t)$ just pre-subtracts some part of it that cannot be retrieved by the inversion.

- The flux components/processes can be split into different time scales, such as their long-term mean, mean seasonal cycle, interannual and short-term variability, each of which is treated a separate component in the flux model.

Taking into account the remarks above, the individual flux components in the STD-inv set-up (updated version of Rödenbeck (2005)) used in this thesis, are:

1. Land-atmosphere exchange:

   - Long-term:
     The long-term component has the fixed term $(f_{fix,nee,lt(x,y,t)})$ that equals the 1980-1992 mean NEE flux from the CCMLP-LPJ biosphere model (Sitch et al., 2000; McGuire et al., 2001) and the adjustable term has a spatial weighting $(f_{sh,nee,lt(x,y,t)})$ proportional to the mean NPP of CCMLP-LPJ. This NPP weighting is taken as a proxy for vegetation activity.

   - Seasonal:
     The seasonal cycle does not have a fixed term, because the fixed term already exists in the long-term component. The shape of the adjustable term $(f_{sh,nee,seas(x,y,t)})$ is constant in time and has a spatial structure that equals the amplitude of the mean seasonal cycle of NEE from CCMLP-LPJ.

   - Interannual:
     Also, there is no fixed term for the interannual variations, but the shape of the adjustable term $(f_{sh,nee,iav(x,y,t)})$ is NPP weighted, as in the long-term NEE-component.

   Based on that the land flux components in STD-inv have only the long-term mean in the fixed-term. However, the optimization algorithm in the model has the ability to adjust the flux for different time scales including the long-term mean, seasonal cycle, and interannual variability.

2. Ocean-atmosphere Exchange:
   The fixed term of the ocean flux is taken from the flux estimates by Takahashi et al. (2009) based on the net air-sea CO_2 flux that is estimated using the air-sea pCO_2 (partial pressure of CO_2) difference and an air-sea gas transfer rate that is parameterized as a function of wind speed. The fixed term of ocean flux from

Takahashi et al. (2009) contains the mean seasonal cycle and the long-term mean. There is no adjustable term for ocean fluxes, where the interannual variability is generally believed to be small compared to land (Prentice, 2001; Rödenbeck et al., 2003).

3. Fossil Fuel emissions:
Fossil fuel emissions are generally considered to be better known than the land-atmosphere flux exchange or ocean fluxes. Moreover, they have a very peaked spatial structure, which cannot be resolved by the atmospheric data. Therefore, emission estimates are taken from fuel use statistics.

In STD-inv, the fixed term is based on the yearly totals and geographical distribution of the fossil fuel emissions that is taken from EDGAR (the Emission Database for Global Atmospheric Research) version 4.0 (EC-JRC/PBL, 2009) (source: http://edgar.jrc.ec.europa.eu/), which provides a complete gridded historical emission trend from 1970 until 2005 calculated based on energy production and consumption, industrial manufacturing, agricultural production, waste treatment, and disposal and burning of biomass. For 2006, the data have been extrapolated based on the global totals from PBL statistics (Netherlands Environmental Assessment Agency (PBL)). There is no adjustable term.

3.1.2   Atmospheric transport model

The global atmospheric transport model TM3 (Heimann and Körner, 2003) is used to calculate the transport matrix A. The TM3 model is a three dimensional Eulerian transport model that solves the continuity equation based on given time-dependent meteorological fields for an arbitrary number of atmospheric tracers (in our case CO_2). The model is driven by meteorological fields derived from the NCEP reanalysis (Kalnay et al., 1996) that cover the our simulation period (1982-2006). The meteorological input varies interannually according to the true year of the simulation (Rödenbeck et al., 2003). The spatial structure of the model is a regular latitude longitude grid and a sigma coordinate system in the vertical. In this study, the spatial resolution of the model is 4° latitude × 5° longitude × 19 vertical levels. Modeled concentration values are picked from the model grid box that contains the respective site. Each modeled value is taken at the same date and time at which the corresponding measured value has been sampled (Rödenbeck, 2005).

3.1.3 CO_2 concentration data

The CO_2 concentration data are provided by different institutions (e.g. flask data of NOAA/CMDL's sampling network, update of Conway et al. (1994)), Japan Meteoro-

logical Agency (JMA), Meteorological Service of Canada (MSC), and many others, see Rödenbeck (2005)). The choice of the CO_2 stations is a vital problem for many reasons: (1) The sampling at the different stations began at different times, so the dataset is not homogeneous with time, (2) some measurements may not be representative for large source areas or badly reproduced in the transport model (small scale features can not be captured due to the coarseness of the transport model), (3) some of these stations are affected by local emissions, (4) at some locations, two or more alternative records exist, measured by different institutions or using different experimental techniques, (5) varying temporal data density (flask records vs. continuous records). These factors are explained in more detail in Rödenbeck (2005).

In Rödenbeck (2005), automatic and manual section of the data has been done to solve some of these issues. For example, some data records are merged together where both flask records and continuous records exist by applying a data weighting density approach (explained in (Rödenbeck, 2005)) to compensate potentially varying temporal data density. Also, some "spikes" in some data records (suspected to be due to some local emission) are removed manually. For that, the dataset based on the updated version of Rödenbeck (2005) are used in our study here.

For codes, names, and locations of the sites see table 3.1 and figure 3.1. Figure 3.2 shows the data availability for each station used during our simulation period (1982-2006).

Remark: spurious flux variations

In the choice of CO_2 observing stations, there are some competing requirements. The more stations we use the better the constraint on the simulated fluxes and the lower the uncertainty on the optimized parameters and vice versa. In STD-inv (mainly constrained by the atmospheric information, section 3.1.1.1), changes in station density throughout the study period (1982-2006) can lead to spurious flux variations over the regions influenced by the new stations. This is due to changes from prior-constrained to data-constrained. Accordingly, the resulting time-series of the flux estimates may be misinterpreted as interannual variability in concentration (Rödenbeck et al., 2003; Rayner et al., 2005).

3.2 The coupled inversion system (SDPRM-inv)

Referring to equation 3.6, the flux field can be written in terms of a set of dimensionless adjustable parameters (vector **p**) as:

Table 3.1— Sites measuring CO_2 concentrations that were used in the inversion. The locations are shown in figure 3.1

Code	Name/Geographic location	Latitude (°)	Longitude (°)	height (m a.s.l.)
ALT	Alert, Canada	82.45	-62.52	210
ASC	Ascension Island, Atlantic	-7.92	-14.42	54
BAL	Baltic Sea, Poland	55.50	16.67	7
BHD	Baring Head, New Zealand	-41.42	174.87	85
BME	St. David's Head, Bermuda	32.37	-64.65	30
BMW	Southhampton, Bermuda	32.27	-64.88	30
BRW	Barrow, Alaska	71.32	-156.60	11
CBA	Cold Bay, Alaska	55.20	-162.72	25
CFA	Cape Ferguson, Australia	-19.28	147.05	2
CGO	Cape Grim, Tasmania	-40.68	144.68	94
CHR	Christmas Island, Pacific	1.70	-157.17	3
CMN	Monte Cimone	44.18	10.70	2165
ESP	Estevan Point, Canada	49.38	-126.53	39
HUN	Hegyhatsal, Hungary	46.95	16.65	344
ICE	Heimaey, Iceland	63.25	-20.15	100
IZO	Izana, Tenerife	28.30	-16.48	2360
KER	Kermadec Island	-29.03	-177.15	2
KEY	Key Biscayne, Florida	25.67	-80.20	3
KUM	Cape Kumukahi, Hawaii	19.52	-154.82	3
LJO	La Jolla Pier, California	32.87	-117.25	15
LMP	Lampedusa, Italy	35.51	12.61	50
MAA	Mawson, Australia	-67.62	62.87	32
MHD	Mace Head, Ireland	53.33	-9.90	25
MLO	Mauna Loa, Hawaii	19.53	-155.58	3397
MNM	Minamitorishima, Japan	24.30	153.97	8
MQA	Macquarie Island, s. ocean	-54.48	158.97	12
NWR	Niwot Ridge, USA	40.05	-105.58	3475
PSA	Palmer Station, Antarctica	-64.92	-64.00	10
RPB	Ragged Point, Barbados	13.17	-59.43	3
RYO	Ryori, Japan	39.03	141.83	230
SCH	Schauinsland, Germany	47.92	7.92	1205
SHM	Shemya Island, Alaska	52.72	174.10	40
SIS	Shetland Islands, UK	60.17	-1.17	30
SMO	Tutuila, American Samoa, Pacific	-14.25	-170.57	42
SPO	South Pole	-89.98	-24.80	2810
STM	Station 'M', Atlantic	66.00	2.00	7
UTA	Wendover, Utah, USA	39.90	-113.72	1320
UUM	Ulaan Uul, Mongolia	44.45	111.10	914
SUR	Aircraft Measurements	61.00	73.00	
EOM	Aircraft Measurements	Between Japan and Australia		
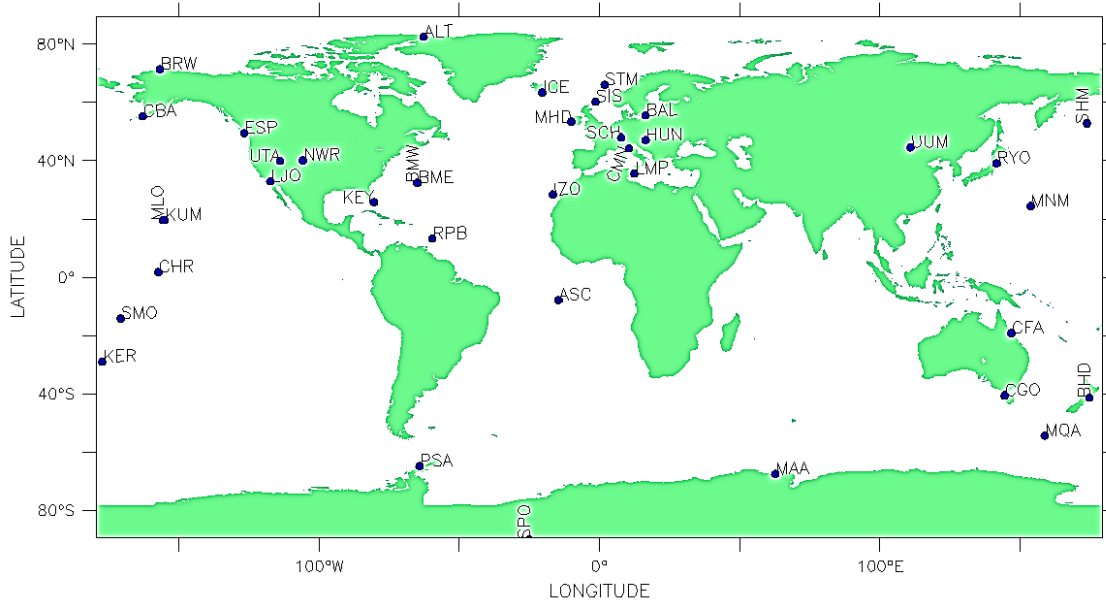
Figure 3.1— Locations of the stations measuring atmospheric CO_2 concentrations.

$$
\begin{aligned}
\mathbf{f(p)} &= \mathbf{f}_{\text{fix}} + \mathbf{f}_{\text{adj}} \\
&= \mathbf{f}_{\text{fix}} + \mathbf{Fp}
\end{aligned}
\tag{3.7}
$$

where $\mathbf{F}$ is the deviation term from the fixed term $\mathbf{f}_{\text{fix}}$ that will be scaled by adjusting $\mathbf{p}$ through the inversion calculation.

As mentioned earlier, the total flux $\mathbf{f}$ is considered as the sum of different source and sink components. These components are, (1) fossil fuel emission (ff), (2) land-atmosphere carbon exchange (nee) and (3) ocean-atmosphere carbon fluxes (oce). Therefore, the fixed term can be written as:

$$
\mathbf{f}_{\text{fix}} = \mathbf{f}_{\text{fix}}^{\text{ff}} + \mathbf{f}_{\text{fix}}^{\text{nee}} + \mathbf{f}_{\text{fix}}^{\text{oce}}
\tag{3.8}
$$

In this study, ocean and fossil fuel fluxes are considered to be known fluxes. Consequently, the adjustable term has only contributions from land fluxes as:

$$
\mathbf{f}_{\text{adj}} = \mathbf{f}_{\text{adj}}^{\text{nee}}
\tag{3.9}
$$

By replacing the land components by R_{eco} and GPP from SDPRM, we can rewrite the
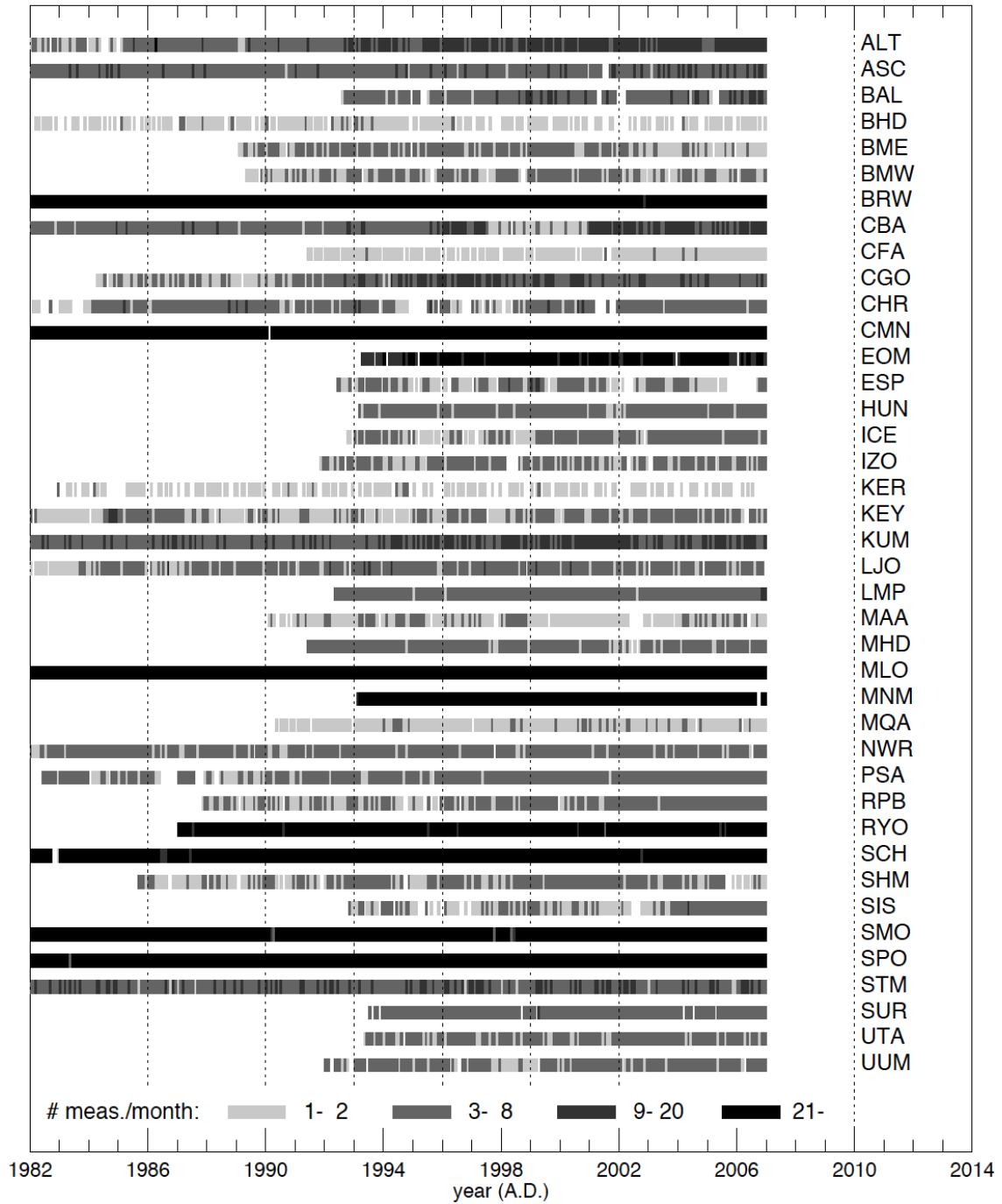
Figure 3.2— CO_2 concentration records. The left part shows the time coverage. The right part shows the list of the stations. F /or the full names and the location of each station see table 3.1, and figure 3.1, respectively.

fixed and adjustable terms as:

$$
\begin{aligned}
\mathbf{f}_{\text{fix}} &= (\mathbf{f}_{\text{fix}}^{\text{Reco}} - \mathbf{f}_{\text{fix}}^{\text{GPP}}) + \mathbf{f}_{\text{fix}}^{\text{ff}} + \mathbf{f}_{\text{fix}}^{\text{oce}} && (3.10) \\
\mathbf{f}_{\text{adj}} &= \mathbf{f}_{\text{adj}}^{\text{Reco}} - \mathbf{f}_{\text{adj}}^{\text{GPP}} && (3.11)
\end{aligned}
$$

where $\mathbf{f}_{\text{fix}}^{\text{Reco}}$ and $\mathbf{f}_{\text{fix}}^{\text{GPP}}$ are the a-priori fields from SDPRM. The fixed terms of the ocean and fossil fuel fluxes are the same as in STD-inv (see section 3.1.1.1).

The adjustable terms $\mathbf{f}_{\text{adj}}^{\text{Reco}}$ and $\mathbf{f}_{\text{adj}}^{\text{GPP}}$ are split into the contributions of their control parameters as:

$$
\begin{aligned}
\mathbf{f}_{\text{adj}}^{\text{Reco}} &= \sum_i \frac{\partial \text{Reco}}{\partial \text{p}_i} \sigma_i \text{p}_i && (3.12) \\
\mathbf{f}_{\text{adj}}^{\text{GPP}} &= \sum_j \frac{\partial \text{GPP}}{\partial \text{p}_j} \sigma_j \text{p}_j && (3.13)
\end{aligned}
$$

where p_i and p_j are the adjustable parameters of R_{eco} and GPP, respectively, which will be optimized and σ_i and σ_j are their a-priori uncertainties. Therefore, GPP and R_{eco} need to be linearized around the adjustable parameter. This is explained in the next sub-sections.

3.2.1 Linearization of R_{eco}

Referring to equations 2.20, 2.21, and 2.22 from chapter 2, the respiration model is written as:

$$
\begin{aligned}
R(x,y,t) &= \Big(R_0 + R_{LAI} \cdot r_{LAI}(x,y)\Big)\varrho_{\text{veg}}(x,y) && (3.14) \\
&\times \ \exp\left(-E\left[\frac{1}{T-T_0} - \frac{1}{T_{ref}-T_0}\right]\right) && (3.15) \\
&\times \ \frac{P+P_0}{P+P_0+K} && (3.16)
\end{aligned}
$$

where E is the activation energy, $T_0 = -46°\text{C}$ (minimum temperature) as in Lloyd and Taylor (1994) and $T_{ref} = 13°\text{C}$ (reference temperature, taken from the 1901-2002 mean of the CRU dataset over land [13.1°C]). P is the precipitation of the previous 30 days (mm), K (mm) is the half-saturation constant of the hyperbolic relationship of soil respiration with monthly precipitation, and P_0 is fixed to the global value 1.55 mm/month (95% confidence interval: [0.2,2.5]) taken from Reichstein et al. (2003).

For the normalization, the remaining adjustable parameters R_0, R_{LAI}, E, and K are normalized by writing them as:

$$R_0 = R_0^{\text{pri}} + \sigma_{R_0} p_{R_0} \tag{3.17}$$

$$R_{LAI} = R_{LAI}^{\text{pri}} + \sigma_{R_{LAI}} p_{R_{LAI}} \tag{3.18}$$

$$E = E^{\text{pri}} + \sigma_E p_E \tag{3.19}$$

$$K = K^{\text{pri}} + \sigma_K p_K \tag{3.20}$$

in terms of the dimensionless adjustable parameters p_{R_0}, $p_{R_{LAI}}$, p_E, and p_K with a-priori zero mean and unit variance. For the a-priori best-guess values and uncertainties of the original parameters, the values in table 3.5 are chosen from the soil-respiration values of Reichstein et al. (2003) assuming that soil respiration accounts for 60% of ecosystem respiration.

The simplified respiration model is linearized around $(p_{R_0}, p_{R_{LAI}}, p_E, p_K) = (0, 0, 0, 0)$ according to:

$$
\begin{aligned}
R(x,y,t)|_{(p_{R_0}, p_{R_{LAI}}, p_E, p_K)} &= \underbrace{R(x,y,t)|_{(0,0,0,0)}}_{R^{\text{pri}}(x,y,t)} \\
&+ \left. \frac{\partial R(x,y,t)}{\partial R_0} \right|_{(0,0,0,0)} p_{R_0} + \left. \frac{\partial R(x,y,t)}{\partial R_{LAI}} \right|_{(0,0,0,0)} p_{R_{LAI}} \\
&+ \left. \frac{\partial R(x,y,t)}{\partial E} \right|_{(0,0,0,0)} p_E + \left. \frac{\partial R(x,y,t)}{\partial K} \right|_{(0,0,0,0)} p_K \\
&+ \dots
\end{aligned}
\tag{3.21}
$$

where the dots represent all higher-order terms of the Taylor expansion which are omitted

in the following equations. This gives

$$R(x,y,t) = R^{\text{pri}}(x,y,t) \tag{3.22}$$

$$+ \quad R^{\text{pri}}(x,y,t)\frac{\sigma_{R_0}}{R_0^{\text{pri}} + R_{LAI}^{\text{pri}} \cdot r_{LAI}(x,y)}p_{R_0} \tag{3.23}$$

$$+ \quad R^{\text{pri}}(x,y,t)\frac{\sigma_{R_{LAI}} \cdot r_{LAI}(x,y)}{R_0^{\text{pri}} + R_{LAI}^{\text{pri}} \cdot r_{LAI}(x,y)}p_{R_{LAI}} \tag{3.24}$$

$$+ \quad R^{\text{pri}}(x,y,t)\left(-\sigma_E\left[\frac{1}{T(x,y,t) - T_0} - \frac{1}{T_{ref} - T_0}\right]\right)p_E \tag{3.25}$$

$$+ \quad R^{\text{pri}}(x,y,t)\frac{-\sigma_K}{P(x,y,t) + P_0^{\text{pri}} + K^{\text{pri}}}p_K \tag{3.26}$$

This linearization has approximately the same functional dependence on T as the non-linearized model $r_T[E,T]$ (see equation 3.15) over a temperature range of $T = -5\ldots30°\text{C}$ and a parameter range of $E = 70\ldots200$ K ($\approx 2\sigma$ range), as shown in figure 3.3. For parameter values p_E well outside the 2σ interval a non-monotonic temperature dependence occurs; therefore, if p_E should take such values a-posteriori, the sigma interval would need to be reduced in the later parameter optimization algorithm.
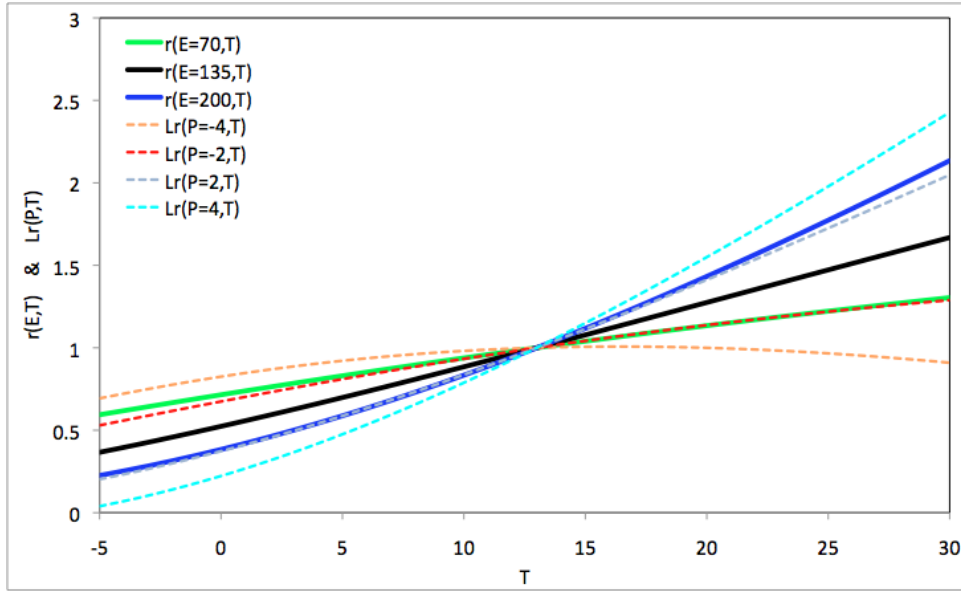
Figure 3.3— Temperature dependence of $r_T[E, T]$ for different values of E (lines) (equation 3.15), and temperature dependence of the linearized model $r_T[p, T]$ for different values of p (symbols) (equation 3.25).

Referring to equation 3.12, the adjustable term of R_{eco} can be written as:

$$\mathbf{f}_{\text{adj}}^{\text{R}_{\text{eco}}} \quad = \quad \mathbf{f}_{\text{adj}}^{\text{R}_{0\text{PFT}}} + \mathbf{f}_{\text{adj}}^{\text{R}_{\text{LAI}}} + \mathbf{f}_{\text{adj}}^{\text{K}} + \mathbf{f}_{\text{adj}}^{\text{E}} \tag{3.27}$$

where the terms in the right hand side "r.h.s." of equation 3.27 are the r.h.s. of equations 3.23 to 3.26, respectively. The parameters $(\mathbf{p_{R_0}}, \mathbf{p_{R_{LAI}}}, \mathbf{p_k}, \mathbf{p_E})$ shown in the r.h.s. of equations 3.23 to 3.26 will be adjusted by minimizing the cost function (equation 3.4).

3.2.2 Linearization of GPP

Referring to equation 2.30 in chapter 2, GPP fields are given for each PFT by:

$$\begin{aligned}
GPP_{\text{PFT}}^{\text{pri}}(x,y,t) \quad = \quad & \varepsilon_{max\text{PFT}}^{\text{pri}} \cdot \varrho_{\text{PFT}}(x,y) \cdot fAPAR_{\text{PFT}}(x,y,t) \cdot I(x,y,t) \cdot 0.45 \\
\cdot \quad & g_{VPD}[VPD_1, VPD_0, VPD(x,y,t)] \\
\cdot \quad & g_T[T_{\min,0}, T_{\min,1}, T_{\min}(x,y,t)]
\end{aligned}$$
$$\tag{3.28}$$

with $\varepsilon_{max\text{PFT}}$: Maximum light use efficiencies per PFT, $fAPAR_{\text{PFT}}(x,y,t)$: fraction of Absorbed Photosynthetically Active Radiation per PFT, I: incident radiation. The functions g_{VPD} and g_T (between 0 and 1) describe the influence of meteorological conditions on ε with $VPD(x,y,t)$ being daytime mean vapor pressure deficit of the air, and $T_{\min}(x,y,t)$ being the daily minimum air temperature (see figure 2.3 and equations 2.26 and 2.27 in chapter 2).

For the linearization, the adjustable parameter ε_{PFT} is normalized as:

$$\varepsilon_{\text{PFT}} = \varepsilon_{\text{PFT}}^{\text{pri}} + \sigma_{\varepsilon_{\text{PFT}}} p_{\varepsilon_{\text{PFT}}} \tag{3.29}$$

and relative errors

$$\frac{\sigma_{\varepsilon_{\text{PFT}}}}{\varepsilon_{\text{PFT}}^{\text{pri}}} = 0.3 \tag{3.30}$$

To adjust the upper limit of VPD_0 of the linear range (see figure 2.3), a linear combination of two VPD dependencies with different values of VPD_0 per PFT are introduced. Similarly, VPD_1 and $T_{\min,1}$ can be adjusted in the same way, but are not shown in this thesis. The adjustable parameter VPD_0 is normalized as:

$$VPD_{0\text{PFT}} = VPD_{0\text{PFT}}^{\text{pri}} + \sigma_{VPD_{0\text{PFT}}} p_{VPD_{0\text{PFT}}} \tag{3.31}$$

The simplified photosynthesis model is linearized around the adjustable parameter VPD_0

by approximating the derivative by the symmetric difference quotient according to:

$$\frac{\partial GPP}{\partial VPD_0} \approx \frac{\triangle\, GPP}{\triangle\, VPD_0} = \frac{GPP_{VPD_0^H} - GPP_{VPD_0^L}}{VPD_0^H - VPD_0^L} \tag{3.32}$$

where H and L represent higher and lower values calculated by adding/subtracting 2σ (standard deviation) value of the a-priori values of VPD_0 for all PFTs (see table 2.4). The H/L values of VPD_0 for each PFT are given in table 3.2.

Table 3.2— Higher (H) and lower (L) limits of VPD_0 for each PFT used in equation 3.32.

PFT(class)	VPD_0^H (Pa)	VPD_0^L (Pa)
ENF (1)	954	346
EBF (2)	1404	796
DxF (3)	1239	631
SHR (4)	1274	666
SAV (5)	1404	796
GRS (6)	1304	696
CRO (7)	1234	626

Using equations 3.29 and 3.31 in terms of the dimensionless adjustable parameters $p_{\varepsilon_{\mathrm{PFT}}}$ and $p_{VPD_{0\mathrm{PFT}}}$, with a-priori zero mean and unit variance, the simplified photosynthesis model is linearized around $(p_{\varepsilon_{\mathrm{PFT}}}, p_{VPD_{0\mathrm{PFT}}}) = (0,0)$ according to:

$$
\begin{aligned}
GPP(x,y,t)|_{(p_{\varepsilon_{\mathrm{PFT}}})} =\ & \underbrace{GPP(x,y,t)|_{(0)}}_{GPP^{\mathrm{pri}}(x,y,t)} \\
& + \left.\frac{\partial GPP(x,y,t)}{\partial p_{\varepsilon_{\mathrm{PFT}}}}\right|_{(0)} p_{\varepsilon_{\mathrm{PFT}}} + \left.\frac{\partial GPP(x,y,t)}{\partial p_{VPD_{0\mathrm{PFT}}}}\right|_{(0)} p_{VPD_{0\mathrm{PFT}}} \\
& +\ \dots
\end{aligned}
\tag{3.33}
$$

where the dots represent all higher-order terms of the Taylor expansion, which are omitted in the following equations. The GPP model becomes

$$GPP(x, y, t) \;=\; \sum_{\text{PFT}} GPP_{\text{PFT}}^{\text{pri}}(x, y, t) \tag{3.34}$$

$$+ \sum_{\text{PFT}} GPP_{\text{PFT}}^{\text{pri}}(x, y, t) \frac{\sigma_{\varepsilon_{\text{PFT}}}}{\varepsilon_{\text{PFT}}^{\text{pri}}} p_{\varepsilon_{\text{PFT}}} \tag{3.35}$$

$$+ \sum_{\text{PFT}} \frac{GPP_{VPD_{0_{PFT}}^{H}} - GPP_{VPD_{0_{PFT}}^{L}}}{VPD_{0_{PFT}}^{H} - VPD_{0_{PFT}}^{L}} \sigma_{VPD_{0_{\text{PFT}}}} p_{VPD_{0_{\text{PFT}}}} \tag{3.36}$$

Referring to equation 3.13, the adjustable term of GPP can be written as:

$$\mathbf{f}_{\text{adj}}^{\text{GPP}} \;=\; \mathbf{f}_{\text{adj}}^{\text{GPP}\varepsilon_{\text{PFT}}} + \mathbf{f}_{\text{adj}}^{\text{GPP}_{\text{VPD}_{0}\text{PFT}}} \tag{3.37}$$

where $\mathbf{f}_{\text{adj}}^{\text{GPP}\varepsilon_{\text{PFT}}}$ and $\mathbf{f}_{\text{adj}}^{\text{GPP}_{\text{VPD}_{0}\text{PFT}}}$ are the r.h.s. of equations 3.35 and 3.36, respectively. The parameters $p_{\varepsilon_{\text{PFT}}}$, and $\mathbf{p_{VPD_{0}PFT}}$, shown in the r.h.s. of the equations 3.35 and 3.36, will be adjusted by minimizing the cost function (equation 3.4).

3.2.3   SDPRM-inv set-up

SDPRM-inv produces optimized daily fluxes of CO_2. The land fluxes can be split into their processes (e.g. GPP, R_{eco}). The spatial resolution of the model is $4°$ latitude $\times$ $5°$ longitude.

Based on the equations 3.27 and 3.37, there are ten controlling parameters for the respiration model: $\mathbf{R_{0_{PFT}}}$ is applied for the seven PFTs, while $\mathbf{R_{LAI}}$, $\mathbf{E}$, and $\mathbf{K}$ are applied globally. For the photosynthesis model, we have 14 controlling parameters: ε_{PFT}, and $\mathbf{VPD_{0PFT}}$ are applied for each PFT. The full list of the initial values of all parameters and their uncertainties is given in table 3.5.

Many other choices for the parameters are possible. Some parameters can be dropped off or assigned by other criteria (e.g. globally or per PFT) or some others can be added (e.g. VPD_1 and $T_{\min,1}$). In the preparation of this study, we have already tried using different sets of parameters with different descriptions, but results are not shown in this thesis. These parameters were not used either because they did not improve the flux estimates compared to the setup used here or because they produced unrealistic flux estimates compared to STD-inv or the process-based model (BIOME-BGCv1).

As mentioned before, respiration and photosynthesis are calculated independently in SD-

PRM. Based on the flux estimates from SDPRM, the long-term mean of R_{eco} and GPP are 74.5 and 75.5 PgC/year, respectively (1 Petagram = 1 x 10^{15} g). These values are smaller in comparison with the earlier estimates presented in the IPCC AR4 (2007) (GPP = 120 PgC/year, R_{eco} = 119.6 PgC/year). Therefore, several assumptions in the base set-up of the model are considered. First, we scaled the a-priori fluxes of R_{eco} in order to have net annual flux of R_{eco} similar to the estimate in the IPCC AR4 (2007). Second, we used the capability of the inversion system that allows the flux components to be split into different temporal variability. Thus, the temporal variability of R_{eco} is split into long-term (LT) and all other temporal variability (the anomaly (subtracting the LT) of the full time variability) components. The LT component of R_{eco} is kept fixed during the inversion calculation while the other temporal variability components of R_{eco} are free to be adjusted (e.g. the anomaly of IAV or the seasonal cycle) by optimizing the parameters controlling R_{eco}. For GPP, all temporal variability including the LT are adjustable.

Based on the assumptions made for the LT of R_{eco}, the a-posteriori estimate of the long-term mean of GPP is considered prescribed as well. This is because the inversion will try to balance the net annual fluxes by scaling up the mean annual value of GPP. However, this setup will help to identify the processes which can be constrained by atmospheric information. Also, based on the a-posteriori estimate of GPP, we can identify which regions act as sources or sinks of CO_2. In addition, the a-posteriori estimates of GPP for each PFT are compared with the estimates from the recent study by Beer et al. (2010) which presented an observation-based estimate of global terrestrial GPP for different biomes.

3.2.3.1 The main difference between STD-inv and SDPRM-inv

The main difference between STD-inv and the coupled system SDPRM-inv is that STD-inv is used to estimate CO_2 fluxes, while SDPRM-inv is used to optimize terrestrial model parameters (time-independent) using CO_2 measurements as a constraint. Therefore, SDPRM-inv combines the powerful constraints provided by SDPRM and the atmospheric data. Since SDPRM-inv is looking for the optimal time-independent parameters that fit the observations, such a system should not have the problem of spurious flux variations due to the appearance of new data records during the simulation (see the remark in section 3.1.3). Also, as mentioned, each PFT has its own set of parameters that provides a strong link between the various regions in which that PFT is found. Therefore, CO_2 observation over one region may help to constrain fluxes over another region (Rayner et al., 2005).

Another difference is that, in STD-inv, the aggregated affect, not the individual contributions, of different processes seen by the atmospheric CO_2 signal are reproduced in the total flux estimated by inversion simulation. Thus, STD-inv may account for all flux sources,

but without providing information about the underlying processes responsible for the estimated fluxes. On the other hand, in SDPRM-inv system, only the contribution from R_{eco} and GPP are accounted for. That means some other important processes are missing in the system (e.g. fire emission due to biomass burning). Consequently, the a-priori fluxes from SDPRM will probably not be sufficient to satisfy the atmospheric data. In this case, the adjustable components may be forced to account for these missing processes, and hence produce unrealistic results.

3.2.4   Results

In this section we summarize and show the results of the framework described in the previous sections. First, we show the time variation of the estimated fluxes as well as their totals. Next, we show the optimized parameters and their uncertainties compared to their a-priori values, along with the a-posteriori correlation matrix. After that, some examples of the fit to the concentration data used in the calculations are presented. Finally, we show the estimated quantities of GPP for different biomes compared to the findings of the recent study by Beer et al. (2010).

3.2.4.1   Time series of the estimated fluxes

Figure 3.5 shows the comparison between the time series of a-priori and a-posteriori land fluxes estimated from SDPRM-inv and a-posteriori land fluxes estimated from STD-inv. The time series are integrated over three latitudinal bands (see figure 2.4) and de-seasonalized and filtered for interannual variability (IAV) (as in Rödenbeck (2005)). We are comparing SDPRM-inv to STD-inv because the two models are not completely independent since both use the same atmospheric data as well as the background fluxes for fossil fuel and ocean.

In figure 3.5, the amplitude of the a-posteriori fluxes from SDPRM-inv are shifted from their a-priori estimates and become closer to the amplitude of the estimated fluxes from STD-inv, in particular over the tropics. This is more clear during El-Niño events (1982/1983, 1987/1988, and 1997/1998) which are associated with high concentration increase (Rödenbeck et al., 2003; Rayner et al., 2005; Baker et al., 2006). This indicates that the inversion is adding more information to the a-priori fluxes by adjusting some of the parameters controlling GPP and R_{eco} (to be discussed below).

Figure 3.6 shows a similar plot but the land fluxes are integrated over 11 land regions (TransCom regions, see figure 2.4). It can be seen that the a-posteriori fluxes are shifted from their a-priori estimates over many regions including regions where few or no observations are exist (e.g. Southern American tropical/temperate, Eurasian Boreal). This is interesting because it indicates that CO_2 observations over one region could adjust fluxes

over another region with the same type of vegetation (SDPRM divides the globe into seven major PFTs). However, figure 3.6 also shows some differences between the estimated fluxes from the two models, either because STD-inv is badly constrained in smaller regions or because SDPRM is too simple to produce accurate estimates of CO_2 fluxes over certain regions of the globe (e.g. Australia).

The study by van der Werf et al. (2006) shows a significant relationship between larger flux anomalies in the terrestrial tropics and fire emissions. Also, based on the study by van der Werf et al. (2006), roughly two thirds of the 1997 global carbon emissions due to fire were attributed to the Tropical Asia region. In figure 3.6, the monthly data from the Global Fire Emissions Database version 2 (GFEDv2) (van der Werf et al., 2010) integrated over the topical land regions is also plotted. This may explain part of the difference between SDPRM-inv and STD-inv in the Tropical Asia region in 1998, as SDPRM does not include the contribution from fire emission. Figure 3.4 shows the time series of the full time variability of the flux estimates integrated over different regions. In general, we can see that the amplitudes of the a-posteriori fluxes from SDPRM-inv are shifted from their a-priori estimates mainly in Eurasian Boreal/Temperate regions. During the growing season, the optimized fluxes have larger amplitude compared to the results from STD-inv for most of the regions. This might be consistent with the conclusion of Nemry et al. (1999) that most terrestrial biosphere models underestimate seasonality of concentrations at high latitudes. This could be true for the setting of the a-priori parameter in SDPRM, so the optimization increases some of the parameters that control R_{eco} and GPP to match the seasonal cycle of the atmospheric measurements.

Figure 3.8 shows the interannual variability of the a-priori and a-posteriori (optimized) GPP and R_{eco} integrated over three latitudinal bands. It can be seen that the optimized GPP and R_{eco} shifted from their a-priori estimates particularly during El-Niño events (1982/1983, 1987/1988, and 1997/1998) to match the high flux anomalies for NEE as shown in figure 3.5. The changes in the IAV of R_{eco} over the tropics during these periods are more striking than for GPP, suggesting that respiration is a major driver of the IAV of NEE. This is confirmed by the high correlation coefficient ($r = 0.85$) between the IAV of R_{eco} and the IAV of NEE. This is consistent with previous findings (IPCC AR4, 2007) that show the large amount of carbon release during the large El-Niño events is due to either increased heterotrophic respiration or increased biomass burning in the tropics.

Also figure 3.7 shows that the amplitudes of the seasonal cycle of the optimized GPP and R_{eco} are increased compared to the a-priori amplitudes, in particular for the northern hemisphere land which has a larger seasonal cycle compared to the tropical and southern

hemisphere land. This is encouraging because it indicates that both processes (GPP and R_{eco}) can be constrained by the atmospheric signals using the current system.
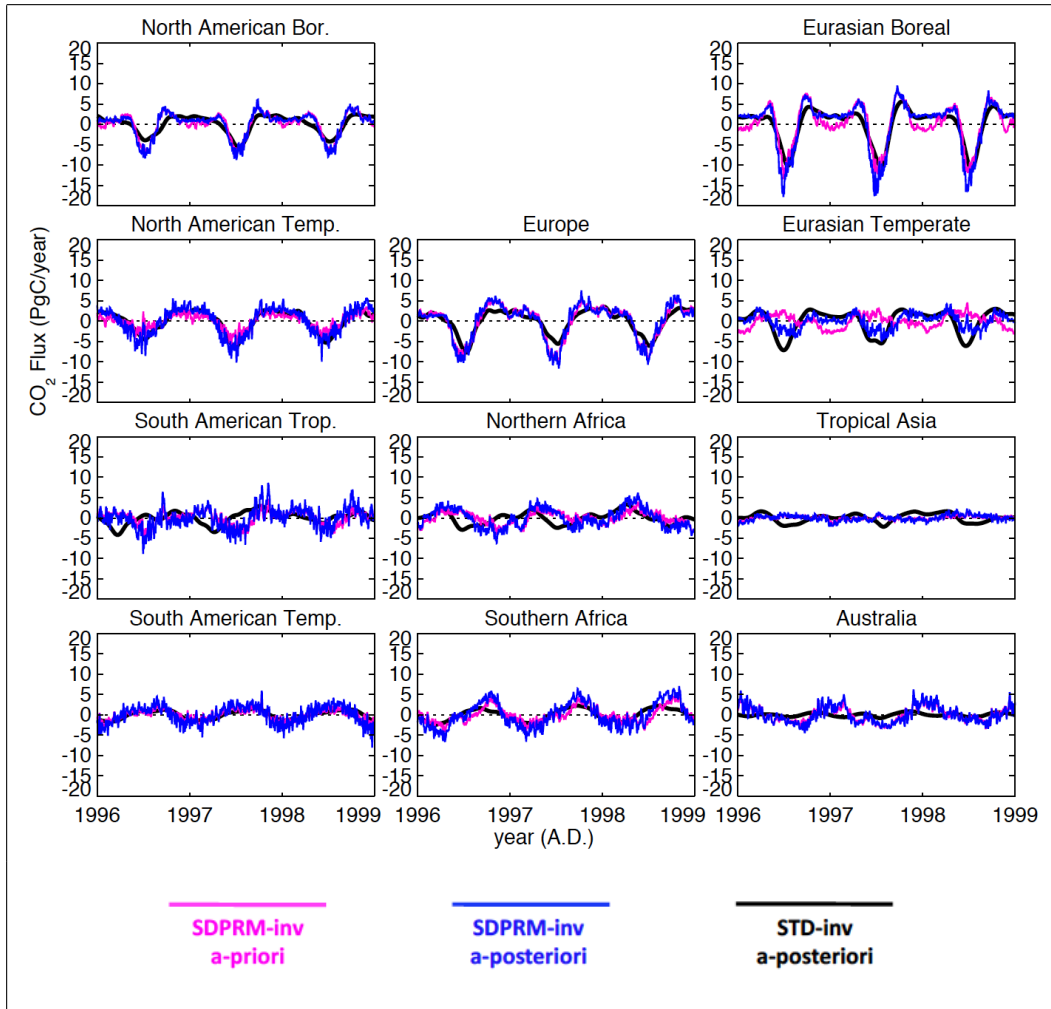
Figure 3.4— Time series of the anomaly of the full variability of the a-priori (Magenta) and a-posteriori (Blue) of the CO_2 fluxes as estimated by SDPRM-inv, and the a-posteriori (Black) of the land CO_2 fluxes as estimated by STD-inv. The time series are integrated over three latitudinal bands (for the map of the regions see figure 2.4).
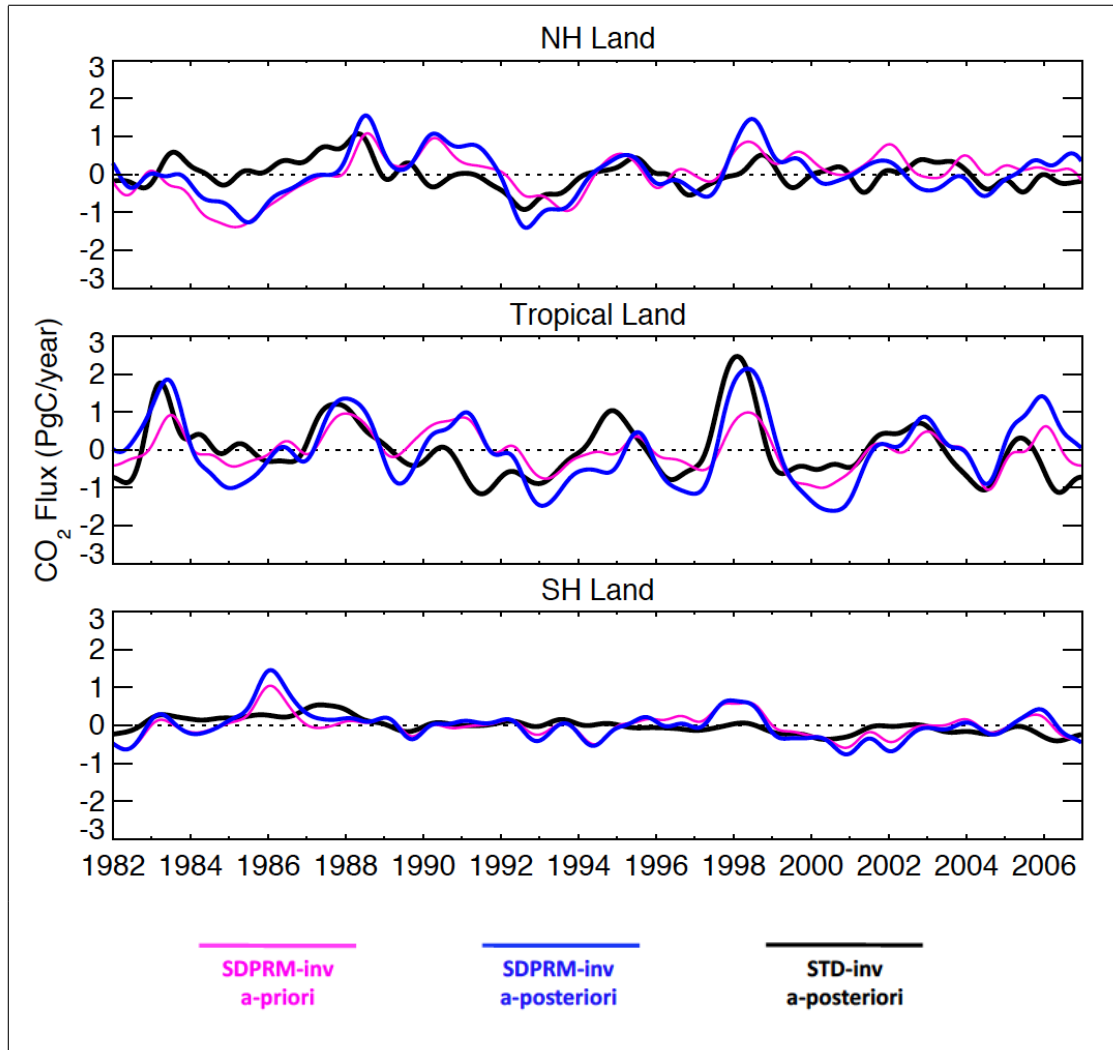
Figure 3.5— Time series of the anomaly of the interannual variability of the a-priori (Magenta) and a-posteriori (Blue) CO_2 fluxes as estimated by SDPRM-inv, and the a-posteriori (Black) of the land CO_2 fluxes as estimated by STD-inv. The time series are integrated over three latitudinal bands (for the map of the regions see figure 2.4) and de-seasonalized and filtered for interannual variability (IAV) (as in Rödenbeck (2005)). The fossil fuel emissions have been subtracted. Positive values denote a net source of natural fluxes (non-fossil-fuel) into the atmosphere.
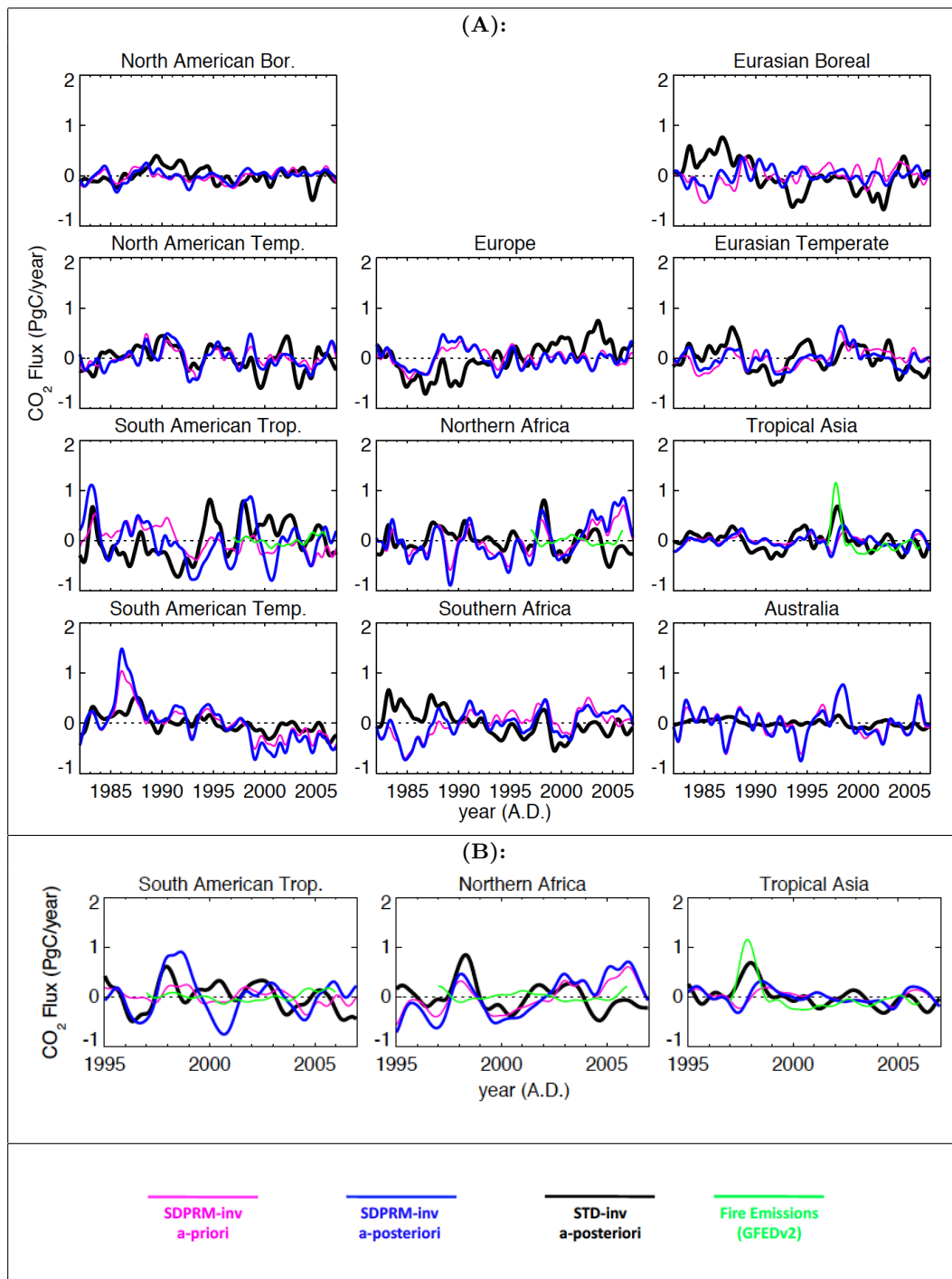
Figure 3.6— (A) is as figure 3.5 but the time series are integrated over 11 land regions (for the map of the regions see figure 2.4). Additionally, the data from the Global Fire Emissions Database version 2 (GFEDv2) (van der Werf et al., 2010) integrated over the tropics is also shown (Green line). (B) is only for the tropical land regions and for the period during which fire data are available.
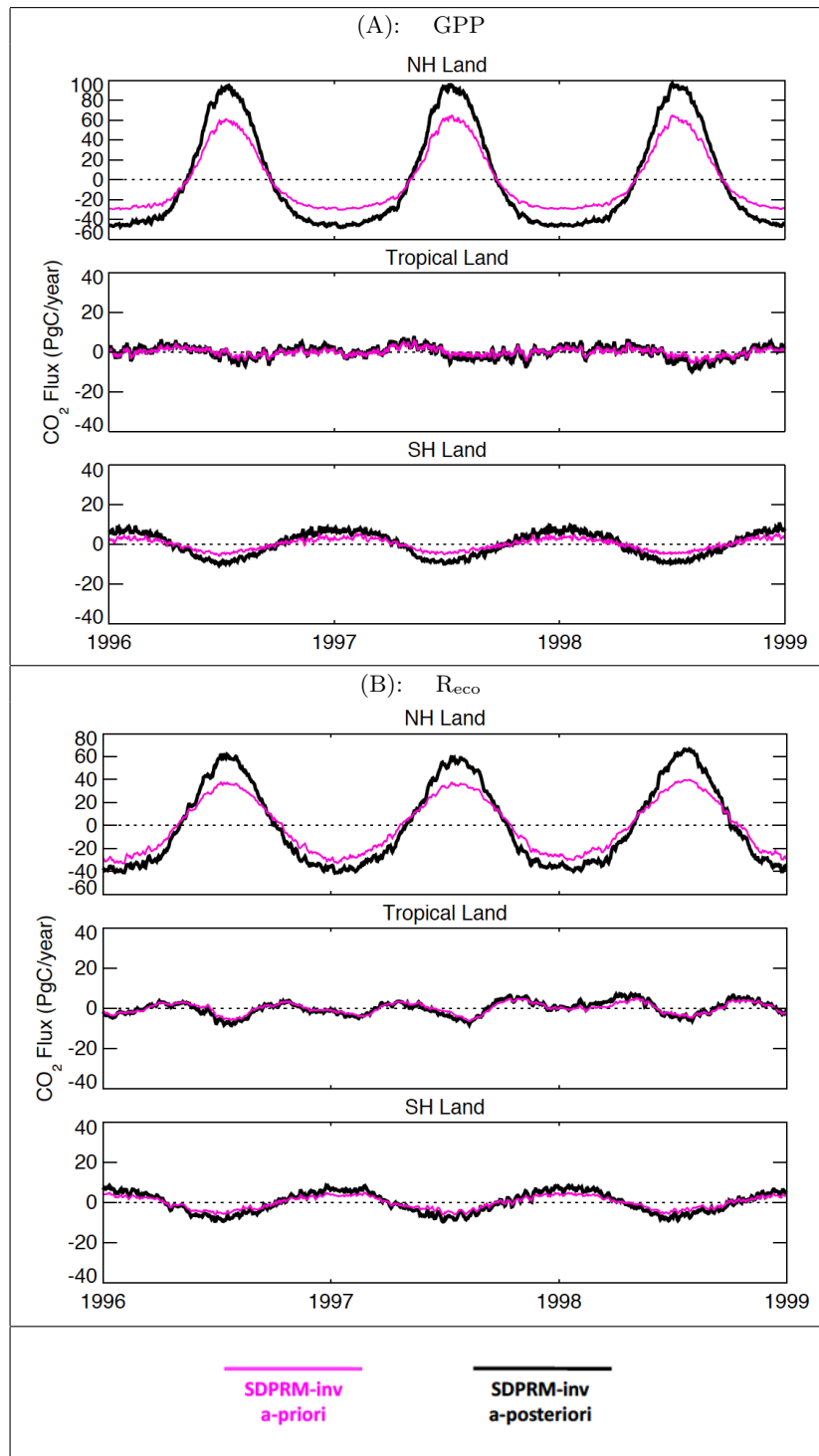
Figure 3.7— The time series of the anomaly of the full variability of the a-priori (Magenta) and the a-posteriori (Black) of (A) GPP and (B) R_{eco} as estimated by SDPRM-inv. The time series are integrated over three latitudinal bands (for the map of the regions see figure 2.4) .
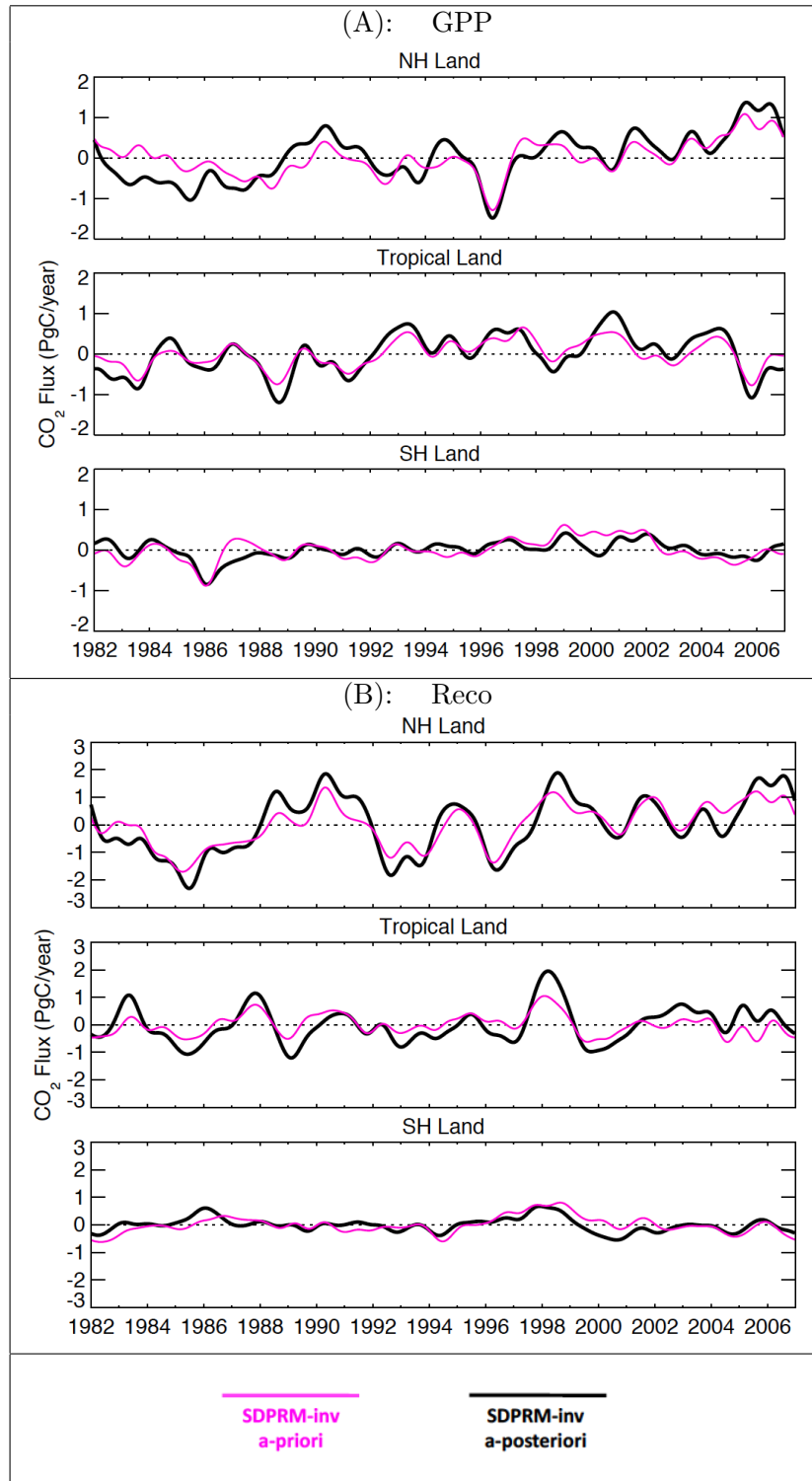
Figure 3.8— The time series of the anomaly of the interannual variability of the a-priori (Magenta) and the a-posteriori (Black) of (A) GPP and (B) R_{eco} as estimated by SDPRM-inv. The time series are integrated over three latitudinal bands (for the map of the regions see figure 2.4) and de-seasonalized and filtered for interannual variability (IAV) (as in Rödenbeck (2005)).

3.2.4.2 Fit to Data

One way to verify the quality of the results is to check how well the inversion is able to fit the measurements. Taylor diagrams are useful in this context since they provide a visual framework for comparing model results to observations and show how closely the simulated patterns match the observations. Basically, the diagram summarizes correlation coefficients, root mean squared errors, and standard deviations of several models in a single plot (Taylor, 2001). Therefore, the comparison between the simulated and observed CO_2 concentrations at the 40 stations (listed in table 3.1) used in this study are represented with Taylor diagrams.

In these Taylor diagrams, the position of each dot appearing on the plot quantifies how closely the modeled concentrations match the observations. The centered root-mean-square (RMS) difference between the simulated and observed patterns is proportional to the distance to the point on the x-axis identified as "1.0", which is the observations. It reflects the full agreement in shape and phasing. The normalized standard deviation of the simulated pattern (dividing the standard deviation of simulated by the standard deviation of the observed) is proportional to the radial distance from the origin and it represents the agreement in the amplitude of the variability between the modeled and observed concentrations. In general, simulated patterns that agree well with observations (have relatively high correlation and low RMS errors) will lie nearest the point marked "1.0" on the x-axis. Models lying on the same arc of the observation will have the correct standard deviation (which indicates that the pattern variations are of the right amplitude).

Figure 3.9 shows Taylor diagrams for the seasonal cycles (the data has been de-seasonalized and de-trended and filtered to remove only the short-term synoptic variations (less than 3 months) of the modeled CO_2 concentrations from SDPRM-inv (a-priori and a-posteriori) as well as from STD-inv (a-posteriori). Also, figure 3.10 shows similar diagrams but for the interannual variation (the data have been de-seasonalized and filtered for interannual variability (IAV) (as in Rödenbeck (2005)) of the modeled and the observed concentrations. The mean seasonal cycle and the long-term trend have been subtracted from the time series to highlight the short-term and interannual variations.

Based on that, in figure 3.9, it can be seen that the modeled concentrations using the a-posteriori flux estimates from SDPRM-STD-inv are shifted from their a-priori concentrations to be closer to the observations, in particular for the stations CBA, SIS, SHM, RYO, ALT, ICE, CMN, BRW, IZO, BAL, and LMP (for the full names and the location of each station see table 3.1, and figure 3.1)). Interestingly, for the station HUN (Hegyhat-sal, Hungary), the amplitude of the simulated concentrations from SDPRM-inv generally

agree very well with the observations in comparison with the simulation from STD-inv
(see table 3.3). This indicates that SDPRM is producing land fluxes (a-priori) that match
the atmospheric signal well. In addition, figure 3.11 shows the time series of the seasonal
cycle of the simulated and observed concentrations at three stations as examples (ALT:
Alert, Canada, CMN: Monte Cimone, Italy, and CGO:Cape Grim, Tasmania). The figure
shows that the modeled concentration from SDPRM-inv has been improved to match the
shape and the phase of the observations. This is also true for the station CGO, which has
a small seasonal cycle (see table 3.3).

Table 3.3— Statistics from Taylor diagrams for the seasonal cycles of modeled and observed CO_2
concentrations from SDPRM-inv and STD-inv at selected stations : HUN (Hegyhatsal, Hungary), ALT (Alert,
Canada), CMN (Monte Cimone, Italy), and CGO (Cape Grim, Tasmania).

Station		Correlation coefficients w.r.t. observation	Amplitudes (ppm)	Relative amplitudes w.r.t. observation
HUN	Observation	1.00	8.84	1.00
	STD-inv	0.97	5.85	0.66
	SDPRM-inv A-posteriori	0.97	7.51	0.85
	SDPRM-inv A-priori	0.98	8.33	0.94
ALT	Observation	1.00	4.90	1.00
	STD-inv	1.00	4.85	0.99
	SDPRM-inv A-posteriori	0.98	5.18	1.06
	SDPRM-inv A-priori	0.85	4.27	0.87
CMN	Observation	1.00	3.66	1.00
	STD-inv	0.99	3.37	0.92
	SDPRM-inv A-posteriori	0.99	4.11	1.12
	SDPRM-inv A-priori	0.91	2.92	0.80
CGO	Observation	1.00	0.35	1.00
	STD-inv	1.00	0.38	1.08
	SDPRM-inv A-posteriori	0.76	0.24	0.69
	SDPRM-inv A-priori	0.08	0.57	1.63

Modeled seasonal cycles of the CO_2 concentrations from SDPRM-inv for some coastal
stations, like CFA and BHD, have very low correlation and much larger variations than
observations. These sites are under oceanic control, which may explain this mismatch.
Similarly, some sites have a large response to the background fossil fuel fluxes (e.g. BAL,
HUN), and hence errors in these fluxes can explain the mismatches between the modeled
and observed concentrations. Moreover, as previously mentioned, R_{eco} and GPP are the
only processes included in the land fluxes in SDPRM-inv system. Therefore, some of the
missing processes (e.g. biomass burning) which have some impact on the atmospheric
CO_2 concentrations may also explain the differences between the modeled and observed
concentrations. Furthermore, the atmospheric transport model can produce large errors
in the modeled concentrations (Gurney et al., 2002).

The Taylor diagrams in figure 3.10 are similar to those in figure 3.9 but for the internnual variations of modeled and observed concentrations. In general, it can be seen that both the a-posteriori and a-priori concentrations from SDPRM-inv have low correlations with the observations. This is also clear in figure 3.12, which shows the time series of the interannual variability of the simulated and observed concentrations at three stations (ALT: Alert, Canada, CMN: Monte Cimone, Italy, and CGO:Cape Grim, Tasmania) (see also table 3.4 for the statistics). This indicates that the minimization algorithm has more capability to adjust the seasonal cycle compared to the interannual variability in the SDPRM-inv. This could be for many reasons. One reason is that SDPRM does not provide sufficient degrees of freedom (only 24 parameters to be adjusted), and hence the minimization algorithm cannot satisfy all temporal variability in the data. Another possibility is that the impacts of the processes that may affect the internnual variability are not included in the model. One possibility to investigate this is to use different degrees of freedom (to be adjusted independently) that have different effect on the seasonal cycle and the interannual variability.

Table 3.4— Statistics from Taylor diagrams for the interannual variability of modeled and observed CO_2 concentrations from SDPRM-inv and STD-inv at selected stations : HUN (Hegyhatsal, Hungary), ALT (Alert, Canada), CMN (Monte Cimone, Italy), and CGO (Cape Grim, Tasmania).

Station		Correlation coefficients w.r.t. observation	Amplitudes (ppm)	Relative amplitudes w.r.t. observation
HUN	Observation	1.00	1.25	1.00
	STD-inv	0.80	0.62	0.49
	SDPRM-inv A-posteriori	0.28	1.02	0.82
	SDPRM-inv A-priori	0.52	1.06	0.85
ALT	Observation	1.00	1.04	1.00
	STD-inv	0.99	1.08	1.03
	SDPRM-inv A-posteriori	0.74	1.05	1.01
	SDPRM-inv A-priori	0.76	1.04	1.00
CMN	Observation	1.00	0.85	1.00
	STD-inv	0.89	0.98	1.15
	SDPRM-inv A-posteriori	0.67	1.14	1.34
	SDPRM-inv A-priori	0.58	1.14	1.34
CGO	Observation	1.00	0.75	1.00
	STD-inv	1.00	0.80	1.06
	SDPRM-inv A-posteriori	0.76	0.91	1.21
	SDPRM-inv A-priori	0.75	0.77	1.02
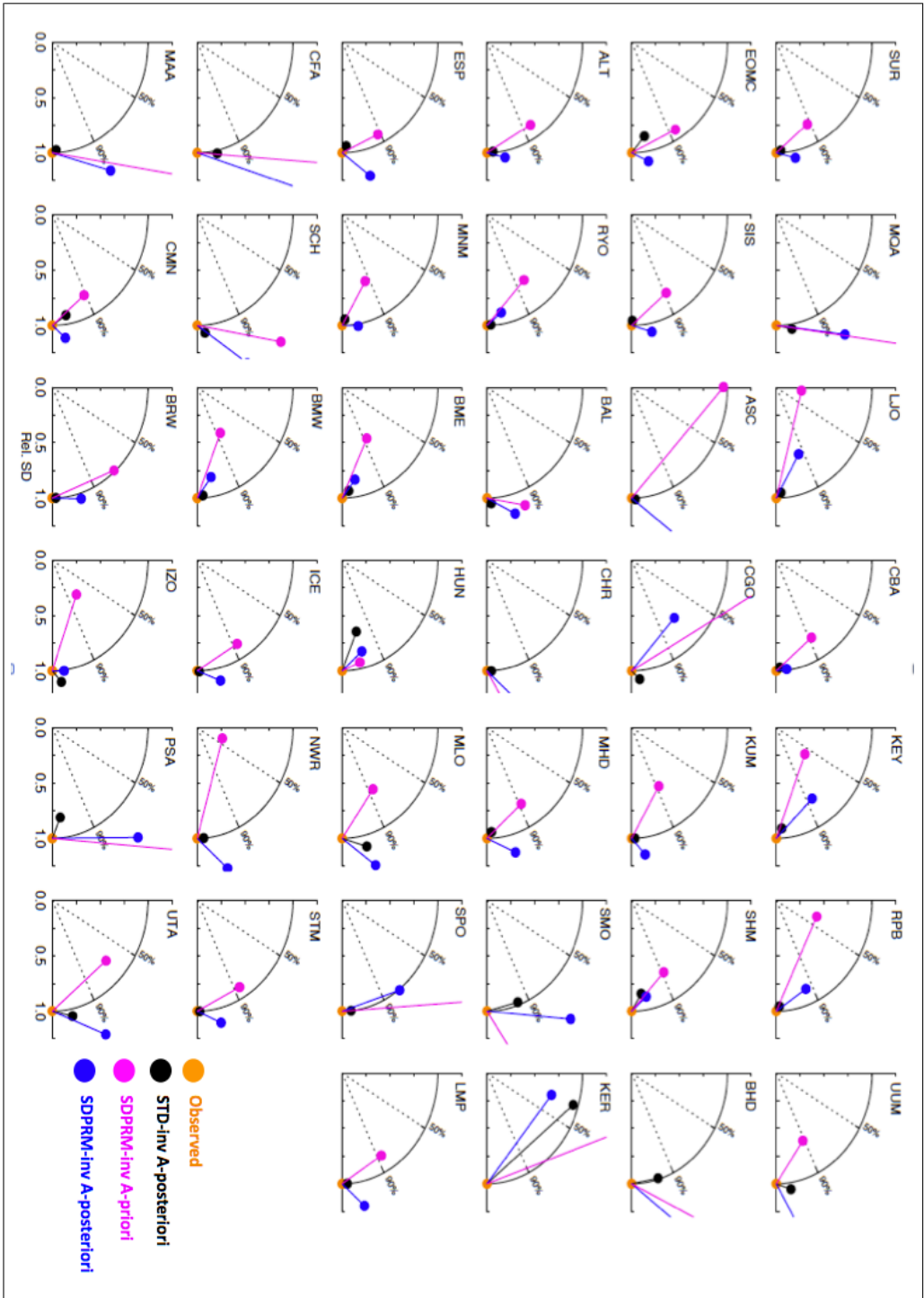
Figure 3.9 — Taylor diagrams for the mean seasonal cycle of the observed and simulated CO$_2$ concentrations for 40 observing sites used in this study. Orange: Observations, Blue and Magenta: a-posteriori and a-priori, respectively, from SDPRM-inv, STD-inv, and Black: a-posteriori from STD-inv. The data have been de-seasonalized, de-trended and filtered to remove only the short-term variations (less than 3 months).
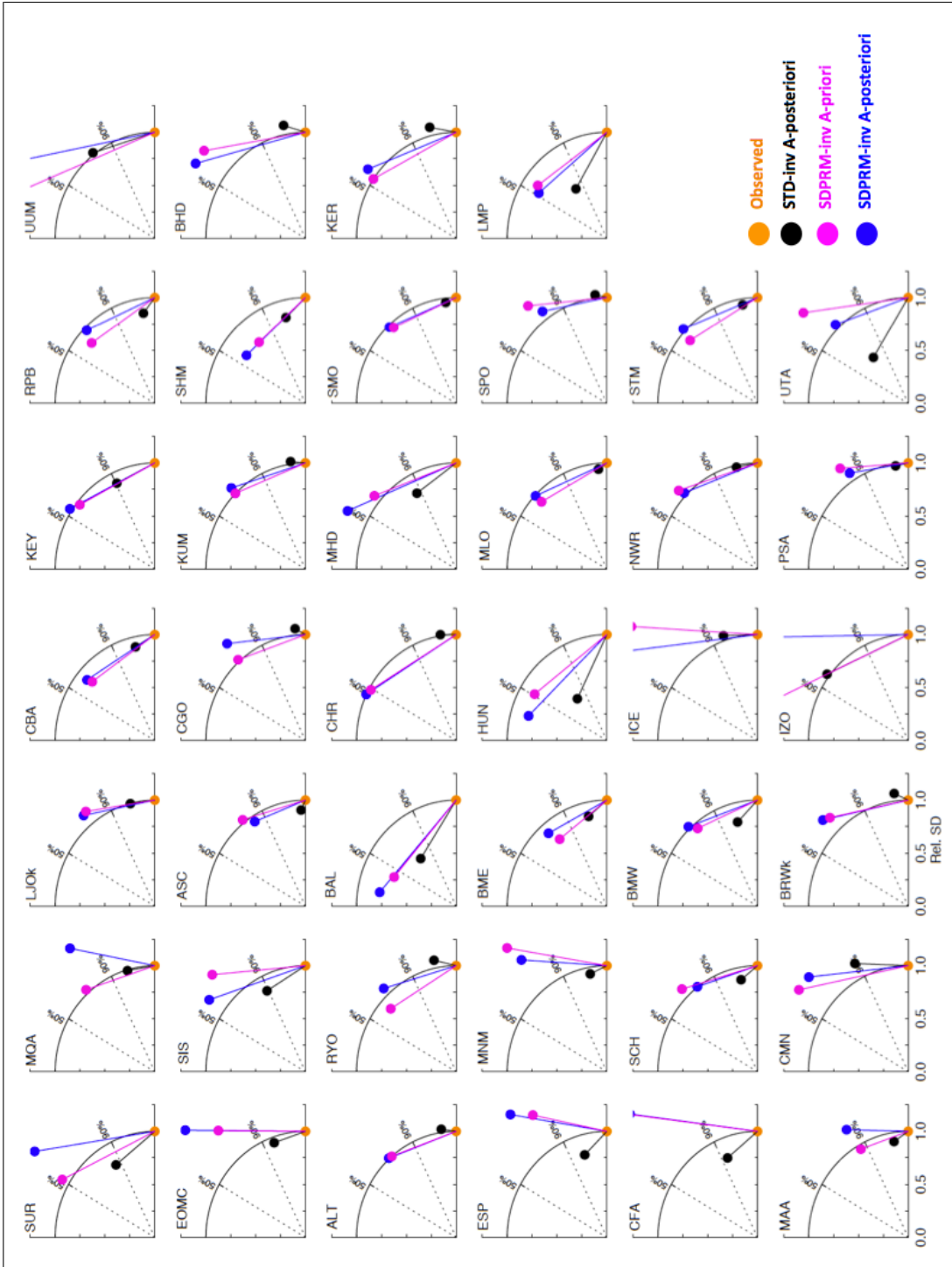
Figure 3.10— As figure 3.9 but for the interannual variability (IAV). The data have been de-seasonalized, de-trended and filtered to remove the short-term variations (less than 1 year).
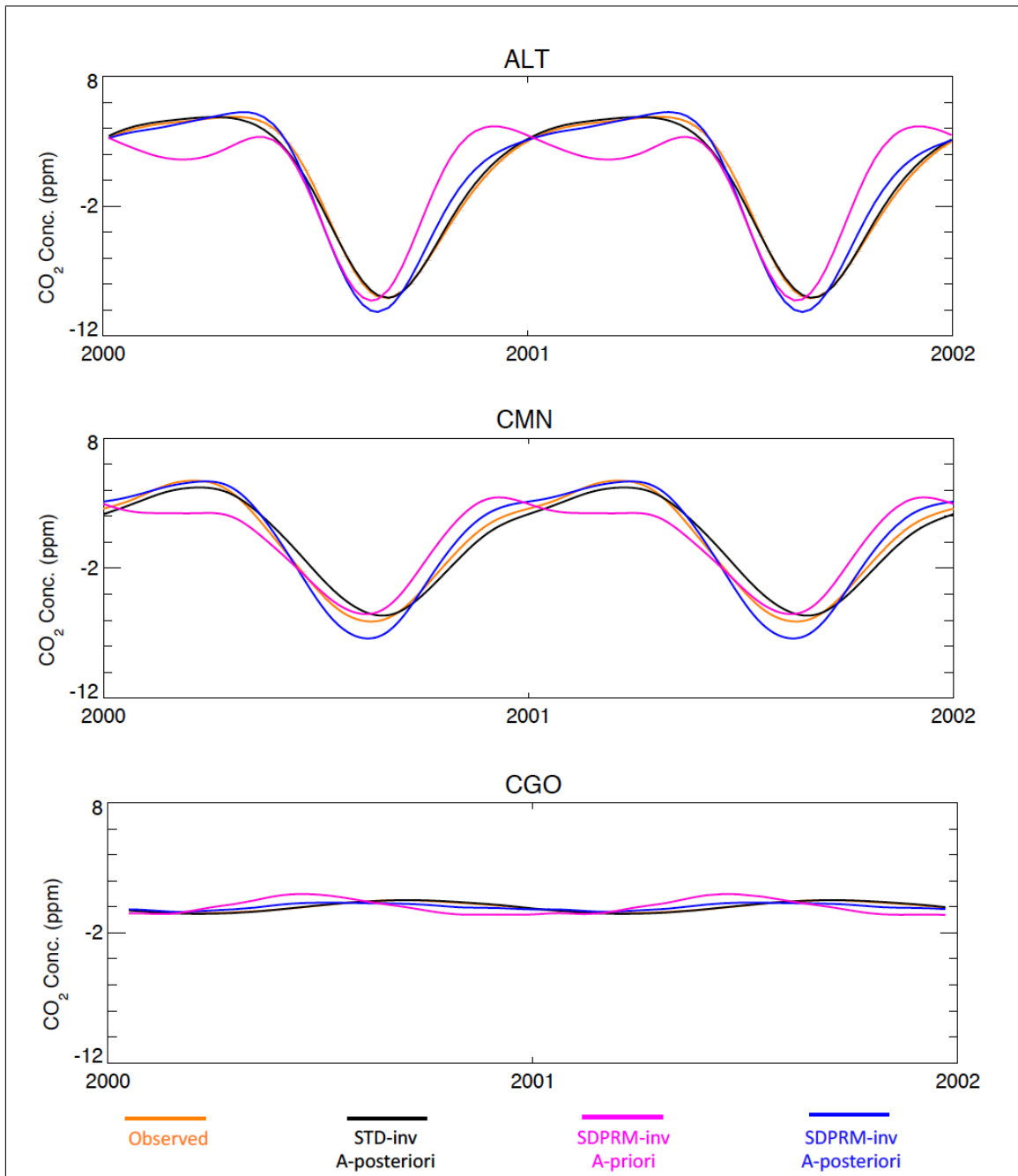
Figure 3.11— The mean seasonal cycle of the observed and simulated CO_2 concentrations for three observation sites (ALT: Alert, Canada, CMN: Monte Cimone, Italy, and CGO:Cape Grim, Tasmania) used in this study. The time series are plotted for two years for the demonstration. Orange: Observation, Blue and Magenta: a-posteriori and a-priori, respectively, from SDPRM-inv, and Black: a-posteriori from STD-inv. The data have been de-seasonalized and de-trended and filtered to remove the short-term variations (less than 3 months).
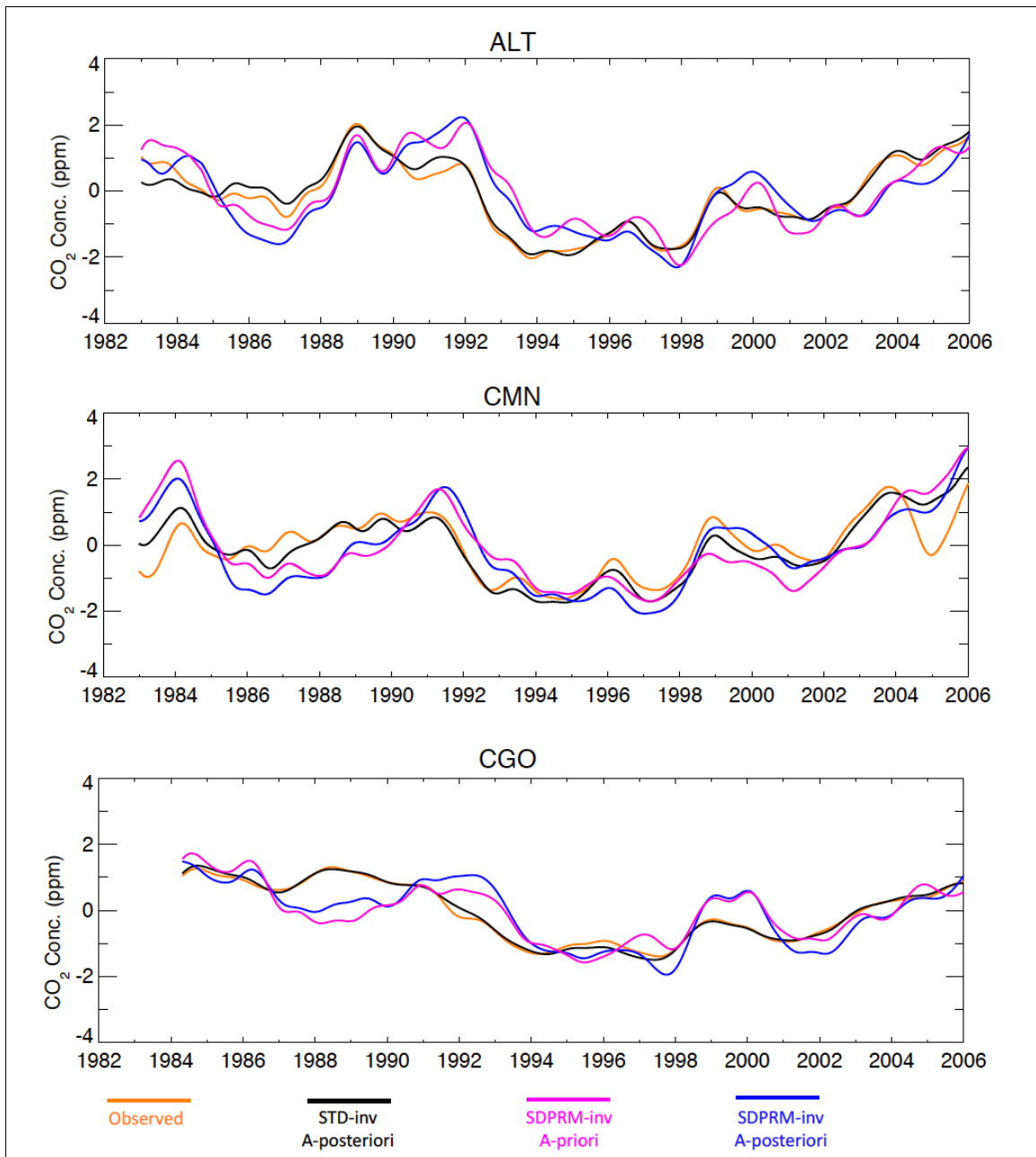
Figure 3.12— As figure 3.11 but for the interannual variability (IAV). The data has been de-seasonalized, de-trended and filtered to remove the short-term variations (less than 1 year).

3.2.4.3   Optimized parameters

Table 3.5 shows the a-priori and a-posteriori values as well as their uncertainties for all the adjustable parameters. Also, it shows the reduction of the uncertainty (RU) for all parameters, which is calculated based on the following formula:

$$\mathbf{RU} = 1 - \frac{\sigma_{post}}{\sigma_{pri}} \tag{3.38}$$

where, σ_{pri} and σ_{post} are the a-priori and a-posteriori uncertainty of the parameter. As mentioned in section 3.2.3, three parameters are adjusted globally ($\mathbf{R_{LAI}}$, $\mathbf{E}$, and $\mathbf{K}$), while the other parameters ($\mathbf{R_{0_{PFT}}}$, ε_{PFT}, and $\mathbf{VPD_{0_{PFT}}}$) are adjusted for each PFT. In table 3.5, it is clear that many of the adjustable parameters are given quite low a-priori uncertainties. This is because when we applied higher uncertainty values for the parameters, the minimization algorithm produced optimized parameters with negative values. This could be because the number of the adjustable parameters (24) is smaller than the number of the data points, and the minimization algorithm cannot satisfy all data. This problem has been explained by Rayner et al. (2005), who found that the optimization algorithm would sometimes search unphysical regions in parameter space. Another explanation could be that by using large uncertainties, the linearization is not a good approximation of the full parameter-dependence any more (as explained for figure 3.3) and hence the uncertainty should be reduced.

In principle, it is expected that the uncertainty of the global parameters should be reduced more compared to the other parameters, which are optimized for each PFT, because they are observed by a larger dataset. In our case, all parameters show a significant reduction of the uncertainties (more than 88%, see table 3.5), indicating that these parameters are well constrained by the data, even though they have relatively small a-priori uncertainties which make it difficult for the data to add more information.

For R_{eco} parameters, several things are apparent from this table. First, all the parameters are shifted from their a-priori values. Second, some parameters are increased, like $\mathbf{R_{0_{ENF}}}$, $\mathbf{R_{0_{SHR}}}$, which mainly represent high latitude biomes (see table 2.2 for the descriptive abbreviations used for each PFT and figure 2.1 for their locations). This is consistent with what is shown in figure 3.7-B where the amplitude of the seasonal cycle of the optimized R_{eco} increased in the northern hemisphere. This indicates that these parameters have been increased to match the seasonal cycle of the CO_2 concentrations. This also may be the case for $\mathbf{R_{LAI}}$ which consider with $\mathbf{R_0}$ as a scaling factor for the amplitude of the seasonal cycle of R_{eco} according to the governing equation 3.14. The other parameters of

R_{eco} decreased, but they mainly represent regions where the seasonal cycle of R_{eco} is small (in the tropics), and hence their impact is relatively small. Similarly, K, which decreased, may have only a small impact on the seasonal cycle of R_{eco}. This is because it represents the precipitation dependence, which is a limiting factor of R_{eco} for water-limited regions in the tropics and the southern hemisphere. The activation energy parameter E decreased while R_{eco} increased and this is also consistent with the equation 3.25.

The controlling parameters of GPP are also shifted from their a-priori values. In general, **VPD$_0$** increased for most of the biomes except for EBF and DxF in which **VPD$_0$** decreased compared to their a-priori values. The same is true for ε, which decreased for ENF, EBF, DxF, and GRS while increasing for SHR, SAV and CRO. Again, as the amplitude of the seasonal cycle of GPP in the northern hemisphere has been increased (shown in figure 3.7 (A)), we would expect that the ε values should increase for the biomes in the northern hemisphere (i.e. ENF), but actually they decreased. On the other hand, **VPD$_0$** has been increased, suggesting that the VPD is the main limiting factor of the seasonal cycle of GPP rather than ε.

Figure 3.13 gives an overview of the a-posterior covariance structure of the errors of the optimized parameters. The diagonal elements necessarily have the value 1. Negative values mean anti-correlation between the errors of the optimized parameters. The better situations are those with small correlation coefficients, indicating that the pair of parameters is constrained independently from one another by the data. A positive value of the correlation between two parameters means that both parameters depend on the same signals in the data and it is hard to distinguish between them.

Based on that, it can be seen in figure 3.13 that **R$_{LAI}$** is anti-correlated to the **R$_0$** parameters for different biomes, indicating that the atmospheric data cannot distinguish between them. This is not surprising since **R$_0$** and **R$_{LAI}$** have a similar impact on R_{eco} according to the governing equation 3.14. Similarly, the parameters ε of DxF and ENF are anti-correlated, also for SHR and ENF and for SAV and EBF. This can be explained by looking at figure 2.1 where these biomes are presented either to the same or to adjacent locations. This suggests that more atmospheric data are needed at these locations in order to distinguish between different sources of CO_2 fluxes.

Also, from figure 3.13, the parameters **R$_{LAI}$** and $\varepsilon_{\mathbf{PFT}}$ are anti-correlated but with relatively small correlation values. This might indicate that there is a chance that the atmospheric data can differentiate between them. Finally, the **VPD$_0$** parameters correlate positively with ε, indicating that information distinguishing them is missing. In general, this correlation matrix helps us to identify new structure of the model that can improve

the estimated fluxes that match the atmospheric signal.

Table 3.5— Controling parameters of GPP and R_{eco} and their initial and optmized values and uncertainities. The uncertainity reduction (%) calculated using equation 3.38 is also shown.

Process	Parameter (unit)	A-priori Value	A-priori Uncertainty	Optimized Value	Optimized Uncertainty	Uncertainty Reduction (%)
R_{eco}	$R_{0_{ENF}}$	1.28	0.10	1.47	0.009	0.91
	$R_{0_{EBF}}$	1.28	0.10	1.14	0.011	0.89
	$R_{0_{DxF}}$	1.28	0.10	1.29	0.010	0.90
	$R_{0_{SHR}}$ (gC/m^2/day)	1.28	0.10	1.19	0.005	0.95
	$R_{0_{SAV}}$	1.28	0.10	0.98	0.011	0.89
	$R_{0_{GRS}}$	1.28	0.10	1.04	0.007	0.93
	$R_{0_{CRO}}$	1.28	0.10	1.17	0.007	0.93
	R_{LAI} (gC/m^2/day)	2.5	0.12	2.54	0.007	0.94
	E (K)	135.00	3.75	107.39	0.150	0.96
	K (mm/month)	2.15	0.13	2.30	0.0088	0.93
GPP	ε_{ENF}	1.0	0.08	0.93	0.0015	0.98
	ε_{EBF}	1.0	0.08	0.91	0.00075	0.99
	ε_{DxF}	1.2	0.09	1.12	0.0018	0.98
	ε_{SHR} (gC/MJ)	0.8	0.06	0.83	0.0006	0.99
	ε_{SAV}	0.8	0.06	0.81	0.0018	0.97
	ε_{GRS}	0.6	0.05	0.37	0.0018	0.96
	ε_{CRO}	1.1	0.08	1.12	0.0008	0.99
	$VPD_{0_{ENF}}$	650	45.6	739.93	2.28	0.95
	$VPD_{0_{EBF}}$	1100	45.6	1042.93	2.28	0.95
	$VPD_{0_{DxF}}$	935	45.6	927.01	2.74	0.94
	$VPD_{0_{SHR}}$ (Pa)	970	45.6	1095.97	2.28	0.95
	$VPD_{0_{SAV}}$	1100	45.6	1132.29	4.56	0.90
	$VPD_{0_{GRS}}$	1000	45.6	1140.33	5.01	0.89
	$VPD_{0_{CRO}}$	930	45.6	987.39	2.28	0.95
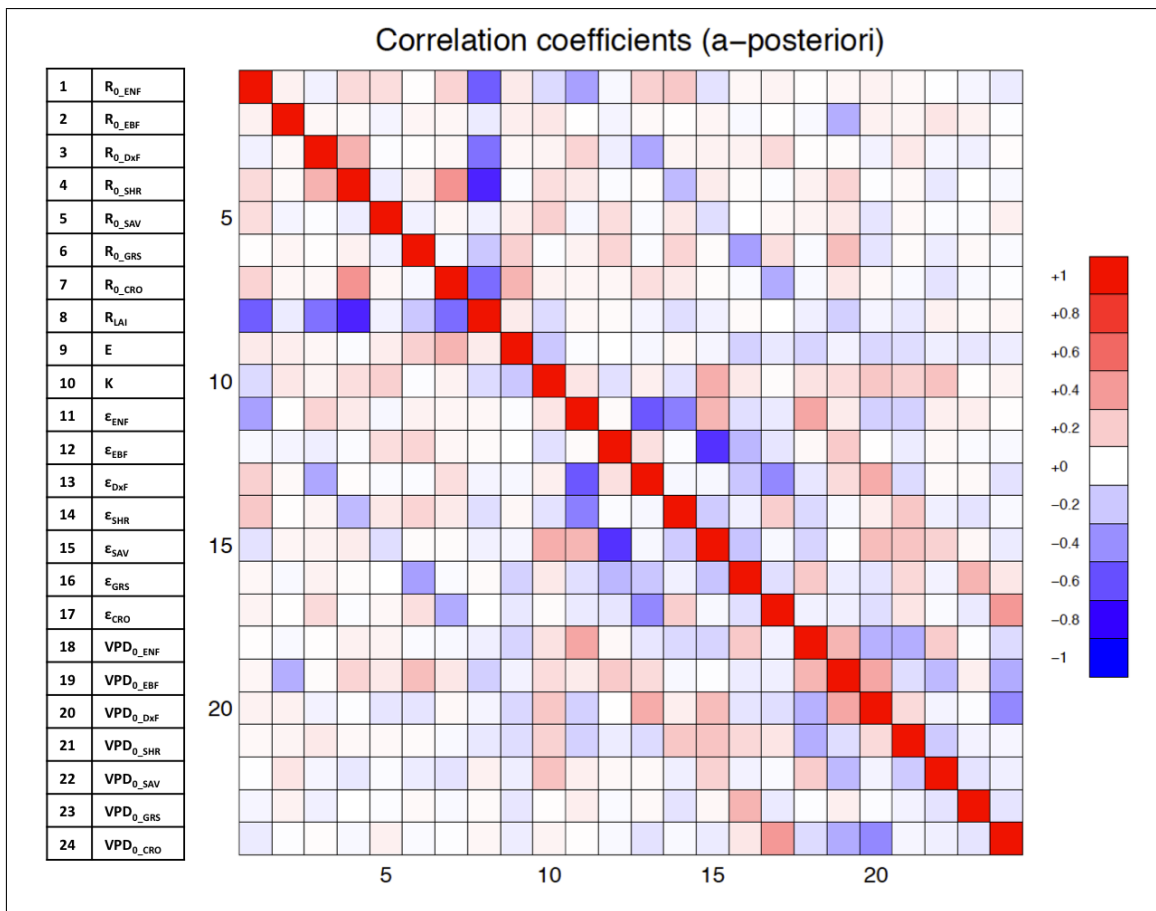
Figure 3.13— Matrix of the error correlation coefficients of the optimized parameters. The left legend shows the individual parameter assigned with an index which is presented in the row and column indices.

3.2.4.4   Total land fluxes

When considering the above results of the optimized parameters, we should take into account the relative biological importance of each biome. A measure of this importance is the total GPP associated with each biome. Figure 3.14 shows the a-priori and a-posteriori estimates of mean annual GPP for each PFT. The total of the optimized GPP has been increased from 74.5 PgC/year to 120 PgC/year, which is consistent with the earlier estimates in the IPCC AR4 (2007)(120 PgC/year).

Unfortunately, there is no direct way to validate these numbers. Recently, with a novel combination of observations and modeling, Beer et al. (2010) estimated GPP values for different biomes which can be compared with the estimates from SDPRM-inv. In the study of Beer et al. (2010), the global field (0.5° × 0.5°) of the median annual GPP (gC/m^2/year) was estimated based on several diagnostic models. For the comparison, the global field of GPP from Beer et al. (2010) (personal communication) has been mapped to the spatial resolution of SDPRM-inv (4° latitude × 5° longitude). Then, the annual GPP values have been calculated for the seven PFTs used in this thesis. In figure 3.14, the a-priori and a-posteriori GPP from SDPRM-inv are compared to GPP values from Beer et al. (2010) for seven biomes. It can be seen that the largest changes in GPP, compared to the a-priori values, occur for GRS (from 5.7 PgC/year to 24.9 PgC/year) and for EBF (from 16.7 PgC/year to 27.7 PgC/year) followed by ENF (from 8.0 PgC/year to 14.2 PgC/year) and DxF (from 11.5 PgC/year to 17.3 PgC/year). For SHR, SAV and CRO, the changes are small. Looking back to the optimized parameters, it can be seen that ε decreased for GRS and ENF while **VPD$_0$** increased, indicating that changes in VPD have more impact on GPP than changes in ε do for these biomes. For EBF, both ε and **VPD$_0$** decreased while GPP value increased, suggesting that either the effect of these parameters is negligible for EBF or the parameters are biased. The comparison, in figure 3.14, also shows that the a-priori estimates of GPP for ENF, DxF, SHR, and GRS from SDPRM are in good agreement with the estimates from Beer et al. (2010) compared to the a-posteriori estimates, in particular for GRS. This could be an indication that: (1) the inverse model tries to compensate for the contribution of the missing processes by increasing GPP for these biomes, (2) the global field of R$_{eco}$ could be wrong for these biomes, which could lead to incorrect estimates of the total GPP (the long-term mean of R$_{eco}$ is not adjustable, see section 3.2.3), or (3) the diagnostic biosphere models underestimate the long-term mean of GPP compared to what the atmospheric signal can produce. More investigation is needed to determine which explanation is correct. On the other hand, from 3.14, we can see that the a-posteriori GPP for EBF and CRO became closer to the estimates from Beer et al.

(2010). The global spatial pattern of the annual GPP from SDPRM-inv and from Beer et al. (2010) are shown in figure 3.15. Also, the difference between the two estimates is shown. The largest difference can be seen for GRS (see the land cover map in figure 2.4) and for EBF regions.

In this comparison, there are several sources of uncertainty which can explain some of the difference in the estimates of GPP. For example, the global field of GPP from Beer et al. (2010) is based on a land cover classification different from the one used in this thesis, leading to different biome areas. Also, the spatial distribution (location, size) of each PFT in both classifications is different (e.g. grassland), producing different GPP values. For example, in Beer et al. (2010), savannas represent both tropical savannas and grasslands, while savannas (SAV) and grasslands (GRS) are separated in SDPRM. In general, we can conclude that the atmospheric data have the potential to infer estimates of the terrestrial GPP for different biomes comparable to other studies.

Finally, table 3.6 shows the breakup of the a-priori and a-posteriori estimates of the mean annual values of R_{eco}, GPP and NEE for different regions as estimated by SDPRM-inv. For comparison, we also show the mean annual value of land fluxes as estimated by STD-inv. We should mention here that the fossil fuel emissions are considered to be known much better a-priori. Therefore, the fossil fuel deviations are neglected in the flux model (no adjustable term), and hence any errors of the a-priori fossil fuel flux will appear as corrections to the total GPP since long-term R_{eco} is fixed. Furthermore, the impact of processes that may affect the seasonality/total of the land fluxes but are not included in the underlying biosphere model (SDPRM) will most probably be compensated by the GPP and R_{eco} terms. Therefore, any conclusions should be drawn with caution from the optimized values here.

In table 3.6, for large spatial scale (3 latitudinal bands), our a-posteriori NEE is quite close to that inferred by STD-inv with a larger source over tropical land and a larger sink over northern hemisphere land (NH). This is not surprising since the estimates of the total fluxes for larger regions are well constrained by the data compared to smaller regions. This is clear when we look at the smaller regions where the differences between the estimates from STD-inv and SDPRM-inv become larger. Overall, more investigation is needed to figure out which processes can be added to account for these differences, which is not an easy task. For example, SDPRM has no treatment of land-use or fires and so they need to be specified as an external flux. However, it is not perfectly clear which quantity can be added to the model since this kind of data is highly uncertain which can result in the propagation of more errors into the model.
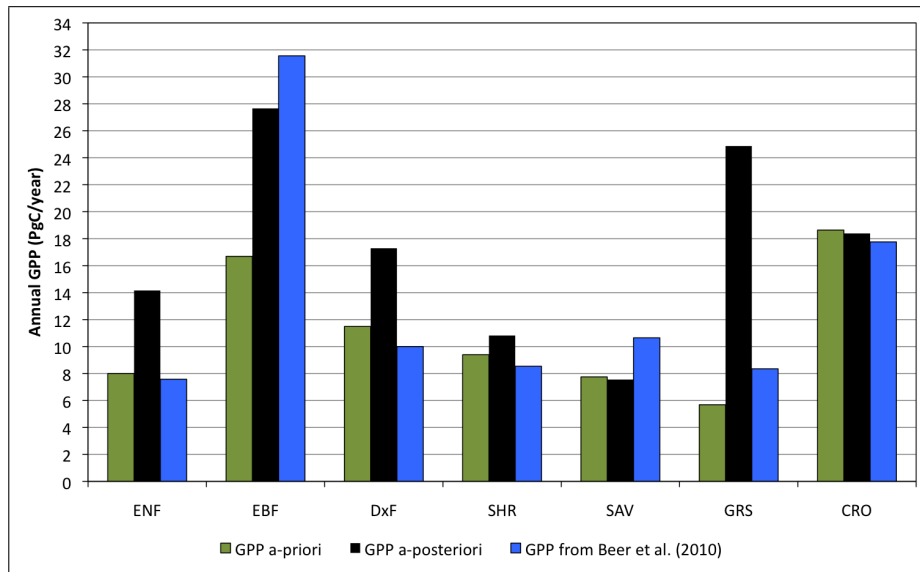
Figure 3.14— The a-priori (green) and a-posteriori (black) estimates of the mean annual GPP values (PgC/year) from SDPRM-inv and the annual GPP values from Beer et al. (2010) mapped to the seven PFTs used in this thesis.

Table 3.6— The a-priori and a-posteriori estimates of the mean annual values (PgC/year) of R_{eco} (release of carbon), GPP (uptake of carbon) and NEE (R_{eco}-GPP) for the period (1982-2006) estimated by SDPRM-inv. The long term mean of R_{eco} was fixed (see section 3.2.3). The last column represents the mean annual value of land fluxes as estimated by the STD-inv. For NEE, positive values denote a net source of non-fossil-fuel fluxes into the atmosphere. For a map of regions see figure 2.4.

Land region	SDPRM-STDinv					STD-inv
	$R_{eco_{pri}}$	GPP_{pri}	GPP_{post}	NEE_{pri}	NEE_{post}	NEE_{post}
LAND TOTAL	119.3	77.7	120.8	41.6	-1.5	-1.6
NH Land	49.7	34.5	53.4	15.1	-3.7	-2.4
Tropical Land	52.7	32.6	50.5	20.1	2.2	0.1
SH Land	16.9	10.6	17.0	6.4	-0.1	0.6
North American Boreal	6.0	4.5	6.2	1.6	-0.2	0.1
North American Temperate	10.9	7.8	13.8	3.1	-2.9	-0.2
South American Tropical	16.7	11.2	18.8	5.5	-2.1	-0.1
South American Temperate	10.7	7.9	11.8	2.9	-1.1	0.7
Northern Africa	14.2	6.4	9.8	7.8	4.4	0.2
Southern Africa	13.3	9.2	14.6	4.2	-1.3	0.1
Eurasian Boreal	10.0	7.7	11.2	2.3	-1.2	-0.4
Eurasian Temperate	14.2	7.6	13.2	6.6	1.0	-1.1
Tropical Asia	6.3	4.2	6.1	2.1	0.2	-0.3
Australia	7.9	3.9	5.9	4.0	2.0	0.0
Europe	9.1	7.3	9.5	1.8	-0.4	-0.7
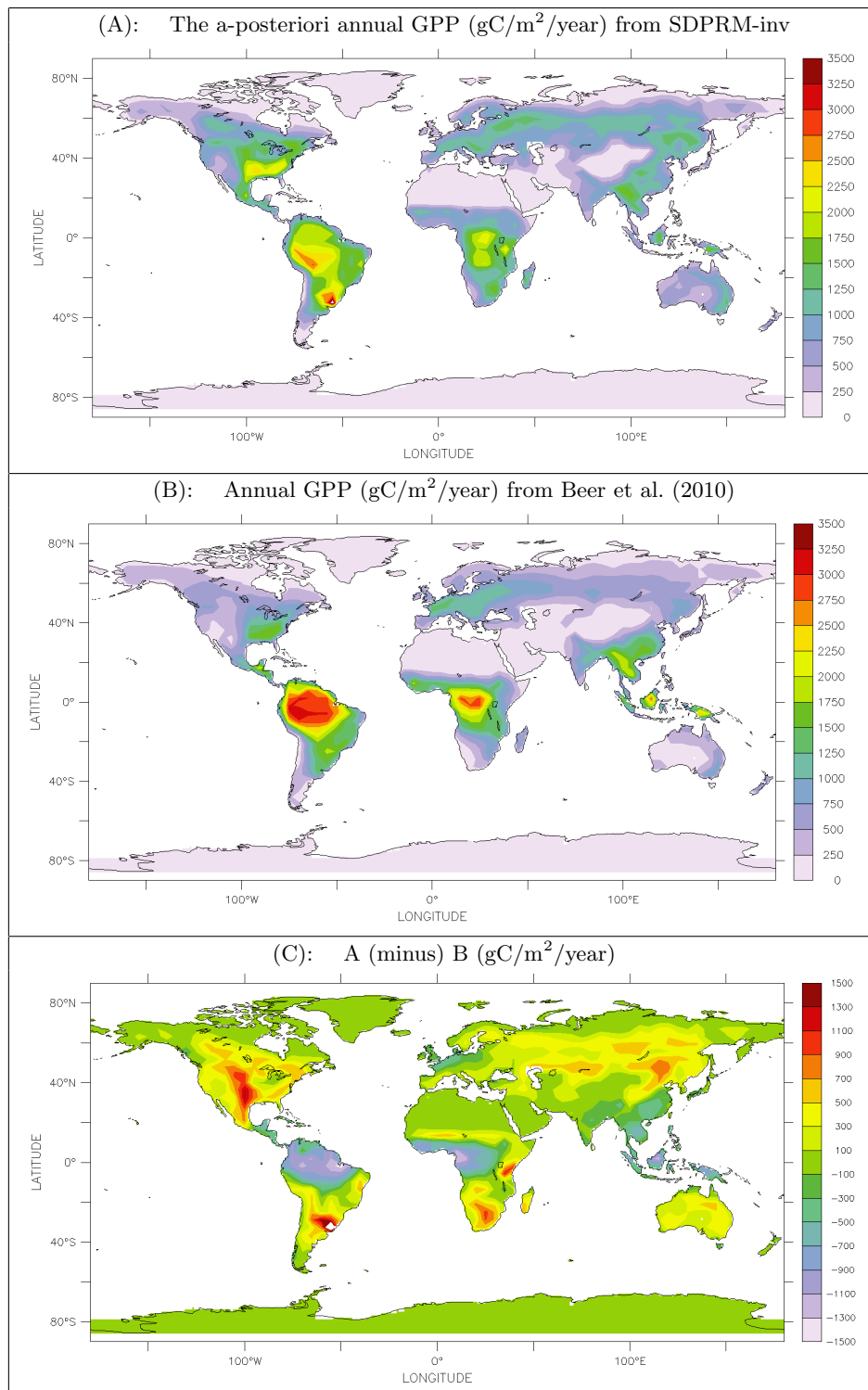
Figure 3.15— The global spatial pattern of the annual GPP (gC/m^2/year) estimated from SDPRM-inv (A), and from Beer et al. (2010) (B), and the difference between them (C).

3.2.4.5   Conclusion

In this chapter, SDPRM was coupled to the atmospheric inversion. This was done for two reasons: first, to provide reasonable a-priori CO_2 fluxes with high spatio-temporal resolution to STD-inv, second, to optimize some internal (physiological and interpretable) parameters of SDPRM in order to fit the atmospheric measurements of CO_2.

We attempted to use the coupled system (SDPRM-inv) to build process understanding into atmospheric inversions. In order to do that, 24 parameters controlling GPP and R_{eco} were optimized in the model using the information of the atmospheric concentrations measured at 40 stations.

The results are promising as they demonstrate that the method works and is capable of fitting the CO_2 concentration data with a set of 24 parameters, in particular the seasonal cycle. The optimization algorithm in the system substantially reduced the a priori uncertainties of most of parameters (more than 88%). In addition to the estimation of uncertainties, the calculation in the coupled system also provides the correlation matrix between the error of the optimized parameters, which allows one to identify which parameters are well constrained by the data and which are not (as discussed in section 3.2.4.3). This can help to establish a new structure of the model in order to improve the estimated fluxes that match the atmospheric signal.

The time series of the fluxes, integrated over different regions, show that the optimized NEE has been shifted from its a-priori pattern. This indicates that the atmospheric signals added more information to R_{eco} and GPP by adjusting their controlling parameters in order to match the variability in the atmospheric data, in particular the seasonal cycle. Also, the time series of the optimized fluxes show that respiration is a major driver of the IAV of NEE, in particular over the tropics. This is encouraging because it indicates that both processes (GPP and R_{eco}) can be constrained by the atmospheric signals using the current system. This is also clear from the high reduction of uncertainty of the parameters.

The optimized mean annual values of GPP shows some similarities to recent results by Beer et al. (2010). That means the atmospheric data have the potential to infer estimates of GPP for different biomes. However, any conclusions should be drawn with caution from the optimized values here.

Chapter 4

Summary and Outlook

4.1 General summary and Conclusion

Serious concerns about increasing CO_2 concentration and its potential impact on the Earth's climate have triggered a vast amount of research worldwide. Therefore, many studies have been conducted in order to understand the processes that control the exchange of CO_2 between the atmosphere, oceans and land ecosystems to decrease the uncertainties of the future climate. It has been found that land biosphere plays a substantial role in the global carbon cycle. However, the most uncertain aspect of the anthropogenic global carbon budget is the breakdown of the terrestrial biosphere sources and sinks of carbon. Therefore, within this thesis, we aimed to quantify the carbon sources and sinks of the terrestrial biosphere using different data constraints (atmospheric CO_2 concentrations, satellite-driven data, and meteorological fields) and different modeling approaches that have been coupled: the bottom-up approach, represented by a Simple Diagnostic Photosynthesis and Respiration Model (SDPRM) based on pre-existing models, and top-down approach, represented by the standard inversion algorithm (STD-inv) introduced by Rödenbeck (2005).

In the first part of this thesis (Chapter 1), an overview about the global carbon cycle has been given, with a focus on the processes that lead the land biosphere to be an important sink of carbon. Then, we have briefly summarized the current state of the art of the main methods that are used to determine the terrestrial carbon budget. Also, the advantages and disadvantages of each method have been discussed, leading to the objective of this thesis. Along with the objective, we highlighted a set of research questions. The conclusions given at the end of each chapter are here summarized in order to answer these questions. An outlook on the possible future development of the results will be discussed.

Simple Diagnostic Photosynthesis and Respiration Model (SDPRM)

In Chapter 2, the implementation details of the Simple Diagnostic Photosynthesis and Respiration Model (SDPRM) have been presented. The ecosystem respiration (R_{eco}) model is based on the formulations introduced by Lloyd and Taylor (1994) and modified by Reichstein et al. (2003), while the photosynthesis model is based on the light use efficiency logic suggested by Monteith (1977) for calculating the Gross Primary Production (GPP). SDPRM was driven by satellite-based and climate data.

To test the performance of the model, we compared simulated carbon flux components with two different approaches for estimating land fluxes. One approach is the process understanding approach presented by the BIOME-BGCv1 model. The second approach is the atmospheric CO_2 inversion in which land fluxes are inferred from the atmospheric data. The updated results of the inverse model of Rödenbeck (2005) are used for the comparison. The comparison showed that SDPRM is capable of producing realistic flux patterns comparable to the ones inferred from the atmospheric inversion or inferred from the process-based model. This is promising since the model is much simpler and easier to apply than sophisticated process-based models.

What is the role of the climatic drivers (e.g. precipitation, temperature, radiation) on the interannual variability of the estimated fluxes?

Different analyses were carried out to test the sensitivity of estimated fluxes of GPP, R_{eco} and NEE to their driving forces (fAPAR and climate data). These analyses suggested that using the mean seasonal cycle of fAPAR with varying climate data to simulate the interannual variability of NEE produces a reasonable match to the results of the atmospheric CO_2 inversion as well as to the process-understanding estimates. Furthermore, the relative contribution of individual climate variables to the interannual variability of GPP and R_{eco} has been evaluated. The results show that temperature is a limiting factor for the interannual variability of GPP and R_{eco} over the northern hemisphere regions, in particular in the cold boreal forest. Vapor pressure deficit (VPD) is the main limiting factor of the interannual variability of GPP over the water-limited regions (e.g. temperate forest in North America, Australia, and India), while radiation is the main limiting factor in the tropical regions. Also, the analyses show that precipitation controls the interannual variability of R_{eco} over large area of the globe but mainly over the tropics and the southern hemisphere. These results are consistent with the findings of Nemani et al. (2003).

Atmospheric CO_2 *Inversion*

In Chapter 3, we briefly described the mathematical algorithm of STD-inv, in particular the construction of the statistical linear flux model. Also, in this chapter, SDPRM has been coupled to STD-inv in different steps. First, SDPRM was linearized around the controlling parameters of GPP and R_{eco}. Then, the linearized model replaced the simple statistical linear flux model of STD-inv. This is in order to, first, provide reliable a-priori CO_2 fluxes with high tempo-spatial resolution to STD-inv, and second, optimize some internal interpretable parameters of SDPRM that fit the atmospheric measurements of CO_2. Based on that, our inversion framework has drawn on certain techniques from previous inversions while including some new features. The novel feature of this inversion is the independent estimation of GPP and R_{eco} instead of just NEE as in STD-inv, which to our knowledge has not previously been performed on the global scale.

Can we improve CO_2 flux estimates by such a coupling?

The results of the coupled system are promising as they demonstrate that the method works and is capable of correcting carbon fluxes from SDPRM over annual and seasonal time scales, as well as over the different GPP and R_{eco} components. This indicates that the atmospheric signals could add more information to GPP and R_{eco} by adjusting their controlling parameters in order to match the variability in the atmospheric data, in particular the seasonal cycle. The optimization algorithm in the system substantially reduced the a-priori uncertainties for most of the parameters (more than 88%). Additionally, the optimized mean annual values of GPP show some similarities to the results of the recent study by Beer et al. (2010). That means the atmospheric data has the potential to infer estimates of GPP for different biomes.

What is the role of different land processes (e.g. respiration, photosynthesis, fire) on the interannual variability of the estimated fluxes?

The optimized model produced a moderate fit to the interannual variability of atmospheric CO_2 concentrations and a good fit to its seasonal cycle. Also based on the optimized results, the interannual variability of NEE is dominated by the tropics which is in turn dominated by the interannual variability of R_{eco}. That implies that respiration is a major driver of the interannual variability of NEE in the tropics.

Furthermore, from such a system, we have learned that some of the missing processes in SDPRM (for example biomass burning) can explain some of the differences between the flux variability simulated by the coupled system and STD-inv as has been shown for

Tropical Asia in 1998.

However, we should keep in mind that the underlying biosphere model is very simple and certainly imperfect. Therefore, flaws in the model will manifest themselves as errors in the model parameters that may produce unreasonable results. Moreover, biases in the meteorological data used to drive SDPRM will certainly produce errors in the a-priori field of GPP and R_{eco}. The impact can be unrealistic optimized results as the inversion tries to resolve an impossible situation. Another consequence of the simplicity of SDPRM is that only 24 parameters are optimized using the atmospheric information, although in a more realistic world, more parameters would have to be specified.

There are other error sources that can produce incorrect flux patterns. For example, the choice of the observation network can affect the flux estimates in a systematic way. The remaining systematic errors in the concentration data after the calibration procedures are one of the error sources. The transport model is considered to be the main contributor to the inversion uncertainty. Unfortunately, the errors from the transport model cannot be assessed within the scope of this thesis. One way is to perform inversions with different transport models (e.g. Gurney et al. (2003)). More details about the error sources in the inversion can be found in Rödenbeck et al. (2003) and Gurney et al. (2003).

4.2 Outlook

There is a range of possible results to explore from the coupled system that can improve our understanding of the terrestrial carbon cycle. In addition, the coupled system is flexible enough to be modified and refined in order to include more sources of information. Eventually this system will of course be further developed. Related to that and based on the results from Chapters 2 and 3, new optimization strategies can be defined as follows:

- Different parameter configurations can be tested to determine which parameters are globally valid and which have to be spatially explicit. Also, some of the constraints can be changed. For example the assumption of perfectly known ocean fluxes can be removed allowing the ocean fluxes to be optimized. Similarly, the long-term mean of R_{eco} can be optimized by keeping the long-term component of GPP fixed.

- Fires contribute significantly to the budget of several trace gases and aerosols (Andreae and Merlet, 2001) and are one of the primary causes of interannual variability in the growth rate of several trace gases, including CO_2 (Langenfelds et al., 2002). Hence, large fluxes of carbon into the atmosphere from wildfires can have an impact on the global carbon cycle. Therefore, it is important to understand the role of fire emissions on the global carbon budget. In this study, fire emission was not included as a-priori fluxes to the model, and hence this can lead to unrealistic optimized fluxes. Therefore, fire emissions can be added as an additional process to the coupled system (SDPRM-inv). However, this should be done with great care, as a-priori knowledge on location and timing of fire emissions are associated with high uncertainty, which can propagate more errors into the model.

- Climate variability is an important factor causing spatial and temporal variations in the terrestrial carbon uptake by affecting the balance between the photosynthesis and ecosystem respiration (Bousquet et al., 2000), although the exact mechanisms remain unclear. Different regions have quite distinct responses to climate variations (DeFries et al., 1998). Hence, a better understanding of the response of the terrestrial carbon flux to the climate perturbation is required in order to understand how climate change will affect the future behavior of the terrestrial carbon sink. Therefore, the relationships between the spatial/temporal patterns of the optimized terrestrial carbon flux and the anomalies of the climate variables (e.g. temperature, precipitation, radiation) can be analyzed for different biomes/regions. This is in order to assess the impacts of the climate variability on the terrestrial carbon flux on individual biomes/regions as well as for different time variability (e.g. seasonal,

year-to-year). Understanding the responses of terrestrial ecosystem carbon fluxes to the climate variations should provide invaluable insights into the spatio-temporal patterns and the causes of the terrestrial carbon sink (Cao et al., 2002).

- Measured changes in the magnitude and the timing of seasonal fluctuations in atmospheric CO_2 concentrations imply an imbalance between terrestrial ecosystem photosynthesis and respiration (Keeling et al., 1995, 1996). However, changes in the atmospheric CO_2 measurements alone cannot differentiate between these two processes. Since photosynthesis and respiration have very different effects on the stable isotope ratio of atmospheric CO_2, measurements of the stable isotope ratio of atmospheric CO_2 in conjunction with atmospheric CO_2 measurements can be used for understanding the components of NEE (Baldocchi et al., 1996; Flanagan and Ehleringer, 1998). Thus, as a further possibility, the isotopic composition of atmospheric CO_2 (such as $^{13}CO_2$, $^{14}CO_2$) can be used as constraints in the coupled system (SDPRM-inv) to discriminate between the signals from different processes (GPP, R_{eco}, and fossil fuel burning). However, isotopic measurements are susceptible to systematic bias. Furtheremore, there are discrepancies between CO_2 isotope measurement laboratories that could lead to incompatible CO_2 carbon isotope dataset (Masarie et al., 2001; Levin et al., 2003). Therefore, different/conflicting biogeochemical interpretation can be obtained, depending on the source of carbon isotope data (Le Quéré et al., 2003).

Bibliography

Ahmadov, R., C. Gerbig, R. Kretschmer, and et al (2007), "Mesoscale covariance of transport and CO_2 fluxes: Evidence from observations and simulations using the WRF-VPRM coupled atmosphere-biosphere model." *Journal of Geophysical Research-Atmospheres*, 112, D22107, doi:10.1029/2007JD008552.

Andreae, M. O. and P. Merlet (2001), "Emission of trace gases and aerosols from biomass burning." *Global Biogeochemical Cycles*, 15, 955–966.

Andres, R. J., G. Marland, I. Fung, and E. Matthews (1996), "A 1*deg* x 1*deg* distribution of carbon dioxide emissions from fossil fuel consumption and cement manufacture, 1950-1990." *Global Biogeochemical Cycles*, 10, 419–429.

Aubinet, M., A. Grelle, A. Ibrom, Ü. Rannik, and J. Moncrieff (1999), "Estimates of the annual net carbon and water exchange of forests: the euroflux methodology." *Advances in Ecological Research*, 30, 113–175.

Baker, D. F., S. C. Doney, and D. S. Schimel (2006), "Variational data assimilation for atmospheric CO_2." *Tellus Series B-Chemical and Physical Meteorology*, 58, 359–365.

Baldocchi, D., R. Valentini, S. Running, OECD, and R. Dahlman (1996), "Strategies for measuring and modelling carbon dioxide and water vapour fluxes over terrestrial ecosystems." *Global Change Biology*, 2, 159–168.

Baldocchi, D. D. and K. B. Wilson (2001), "Modeling CO_2 and water vapor exchange of a temperate broadleaved forest across hourly to decadal time scales." *Ecological Modelling*, 142, 155–184.

Barr, A. G., T. A. Black, E. H. Hogg, N. Kljun, K. Morgenstern, and Z. Nesic (2004), "Inter-annual variability in the leaf area index of a boreal aspen-hazelnut forest in relation to net ecosystem production." *Agricultural and Forest Meteorology*, 126, 237–255.

Battle, M., M. L. Bender, P. P. Tans, J. W. C. White, J. T. Ellis, T. Conway, and R. J. Francey (2000), "Global carbon sinks and their variability inferred from atmospheric O_2 and $\delta^{13}C$." *Science*, 287, 2467–2470.

Beer, C., M. Reichstein, E. Tomelleri, P. Ciais, M. Jung, N. Carvalhais, C. Roedenbeck, and et. al. (2010), "Terrestrial Gross Carbon Dioxide Uptake: Global Distribution and Covariation with Climate." *Science*, 329, 834.

Bellamy, P. H., P. J. Loveland, R. I. Bradley, R. M. Lark, and G. J. D. Kirk (2005), "Carbon losses from all soils across England and Wales 1978-2003." *Nature*, 437, 245–248.

Bolin, B. and C. D. Keeling (1963), "Large-scale atmospheric mixing as deduced from the seasonal and meridional variations of carbon dioxide." *Journal of Geophysical Research*, 68, 3899–3920.

Bousquet, P., P. Peylin, P. Ciais, C. Le Quéré, P. Friedlingstein, and P. P. Tans (2000), "Regional changes in carbon dioxide fluxes of land and oceans since 1980." *Science*, 290, 1342–1346.

Braswell, B. H., W. J. Sacks, E. Linder, and D. S. Schimel (2005), "Estimating diurnal to annual ecosystem parameters by synthesis of a carbon flux model with eddy covariance net ecosystem exchange observations." *Global Change Biology*, 11, 335–355.

Brovkin, V., S. Sitch, W. von Bloh, M. Claussen, E. Bauer, and W. Cramer (2004), "Role of land cover changes for atmospheric CO_2 increase and climate change during the last 150 years." *Global Change Biology*, 10, 1253–1266.

Brown, M. (1993), "Deduction of emissions of source gases using an objective inversion algorithm and a chemical transport model." *Geophysical Research*, 98, 12,639–12,660.

Brown, S. (1997), "Estimating biomass and biomass change of tropical forests." *a primer FAO Forestry Paper no. 134*.

Canadell, J. G., H. A. Mooney, D. D. Baldocchi, J. A. Berry, J. R. Ehleringer, C. B. Field, S. T. Gower, D. Y. Hollinger, J. E. Hunt, R. B. Jackson, S. W. Running, G. R. Shaver, W. Steffen, S. E. Trumbore, R. Valentini, and B. Y. Bond (2000), "Carbon metabolism of the terrestrial biosphere: A multitechnique approach for improved understanding." *Ecosystems*, 3, 115–130.

Cao, M. K., S. D. Prince, and H. H. Shugart (2002), "Increasing terrestrial carbon uptake from the 1980s to the 1990s with changes in climate and atmospheric CO_2." *Global Biogeochemical Cycles*, 16, 1069, doi:10.1029/2001GB001553.

Carlyle, J. C. and U. Ba Than (1988), "Abiotic Controls of Soil Respiration Beneath an Eighteen-Year-Old Pinus Radiata Stand in South-Eastern Australia." *Journal of Ecology*, 76, 654–662.

Churkina, G and SW Running (1998), "Contrasting climatic controls on the estimated productivity of global terrestrial biomes." *Ecosystems*, 1, 206–215.

Churkina, G., J. Tenhunen, P. Thornton, E. M. Falge, J. A. Elbers, M. Erhard, T. Grünwald, A. S. Kowalski, Ü. Rannik, and D. Sprinz (2003), "Analyzing the ecosystem carbon dynamics of four European coniferous forests using a biogeochemistry model." *Ecosystems*, 6, 168–184.

Ciais, P., P. Peylin, and P. Bousquet (2000), "Regional biospheric carbon fluxes as inferred from atmospheric CO_2 measurements." *Ecological Applications*, 10, 1574–1589.

Ciais, P., P. P. Tans, M. Trolier, J. W. C. White, and R. J. Francey (1995), "A large northern hemisphere terrestrial CO_2 sink indicated by the $^{13}C/^{12}C$ ratio of atmospheric CO_2." *Science*, 269, 1098–1102.

Conway, T., P. Tans, L. Waterman, K. Thoning, D. Kitzis, K. Masarie, and N. Zhang (1994), "Evidence for interannual variability of the carbon cycle from the national oceanic and atmospheric administration/climate monitoring and diagnostics laboratory global air sampling network." *Journal of Geophysical Research*, 99, 22,831–22,855.

Cramer, W., A. Bondeau, F. I. Woodward, C. Prentice, R. A. Betts, V. Brovkin, P. M. Cox, V. Fisher, J. A. Foley, A. D. Friend, C. Kucharik, M. R. Lomas, N. Ramankutty, S. Sitch, B. Smith, A. White, and C. Young-Molling (2001), "Global response of terrestrial ecosystem structure and function to CO_2 and climate change: results from six dynamic global vegetation models." *Global Change Biology*, 7, 357–373.

D'Arrigo, R. D, C. M. Malmström, and et. al. (2000), "Correlation between maximum latewood density of annual tree rings and NDVI based estimates of forest productivity." *International Journal of Remote Sensing*, 21, 2329–2336.

Davenport, M. L. and S. E. Nicholson (1993), "On the Relation between Rainfall and the Normalized Difference Vegetation Index for Diverse Vegetation Types in East Africa." *International Journal of Remote Sensing*, 14, 2369.

DeFries, R. S., M. C. Hanson, J. Townshend, and R. Sohlberg (1998), "Global land cover classification at 8km spatial resolution: The use of training data derived from landsat imagery in decision tree classifiers." *International Journal of Remote Sensing*, 19, 3141–3168.

Denman, K.L., G. Brasseur, A. Chidthaisong, P. Ciais, P. M. Cox, R. E. Dickinson, D. Hauglustaine, C. Heinze, E. Holland, D. Jacob, U. Lohmann, S. Ramachandran, P. L. da Silva Dias, S. C. Wofsy, and X. Zhang (2007), *Couplings between changes in the climate system and biogeochemistry. In: Solomon, S., Qin, D., Manning, M., Chen, Z., Marquis, M., Averyt, K.B., Tignor, M. Miller, H.L. (eds.), Climate change 2007: The Physical Science Basis. Contribution of Working Group I to the Fourth Assessment Report of the Intergovernmental Panel on Climate Change (IPCC).* Cambridge University Press, Cambridge, United Kingdom and New York, NY, USA.

Denning, A. S., G. J. Collatz, C. G. Zhang, D. A. Randall, J. A. Berry, P. J. Sellers, G. D. Colello, and D. A. Dazlich (1996), "Simulations of terrestrial carbon metabolism and atmospheric CO_2 in a general circulation model. 1. Surface carbon fluxes." *Tellus Series B-Chemical and Physical Meteorology*, 48, 521–542.

Desai, A. R., P. V. Bolstad, B. D. Cook, K. J. Davis, and E. V. Carey (2005), "Comparing net ecosystem exchange of carbon dioxide between an old-growth and mature forest in the upper Midwest, USA." *Agricultural and Forest Meteorology*, 128, 33–55.

Dixon, R. K., A. M. Solomon, S. Brown, R. A. Houghton, M. C. Trexier, and J. Wisniewski (1994), "Carbon pools and flux of global forest ecosystems." *Science*, 263, 185–190.

EC-JRC/PBL (2009), "Emission Database for Global Atmospheric Research (EDGAR), release version 4.0." URL `http://edgar.jrc.ec.europa.eu`.

Enting, I., C. M. Trudinger, and R. J. Francey (1995), "A synthesis inversion of the concentration and δ^{13}C of atmospheric CO_2." *Tellus*, 47B, 35–52.

Enting, I. G. (1993), "Inverse problems in atmospheric constituent studies: III. Estimating errors in surface sources." *Inverse Problems*, 9, 649–665.

EPICA, community members (2004), "Eight glacial cycles from an Antarctic ice core." *Nature*, 429, 623–628.

Ewel, K. C., W. P. Cropper, and H. L. Gholz (1987), "Soil CO_2 evolution in florida slash pine plantations: II. importance of root respiration." *Canadian Journal of Forest Research*, 17, 330–333.

Falge, E, D Baldocchi, R Olson, P Anthoni, M Aubinet, C Bernhofer, G Burba, R Ceulemans, R Clement, H Dolman, A Granier, P Gross, T Grunwald, D Hollinger, NO Jensen, G Katul, P Keronen, A Kowalski, CT Lai, BE Law, T Meyers, H Moncrieff, E Moors, JW Munger, K Pilegaard, U Rannik, C Rebmann, A Suyker, J Tenhunen, K Tu, S Verma, T Vesala, K Wilson, and S Wofsy (2001), "Gap filling strategies for defensible annual sums of net ecosystem exchange." *Agricultural and Forest Meteorology*, 107, 43–69.

Falloon, P., P. Smith, R. I. Bradley, R. Milne, R. Tomlinson, D. Viner, M. Livermore, and T. Brown (2006), "RothCUK - a dynamic modelling system for estimating changes in soil C from mineral soils at 1-km resolution in the UK." *Soil Use and Management*, 22, 274–288.

Fang, Jingyun, Anping Chen, Changhui Peng, Shuqing Zhao, and Longjun Ci (2001), "Changes in Forest Biomass Carbon Storage in China between 1949 and 1998." *Science*, 292, 2320–2322.

Flanagan, L. B. and J. R. Ehleringer (1998), "Age-dependent variations in δ^{13}C of ecosystem respiration across a coniferous forest chronosequence in the Pacific Northwest." *Tree Physiology*, 13, 10–14.

Francey, R. J., P. P. Tans, C. E. Allison, I. G. Enting, J. W. C. White, and M. Trolier (1995), "Changes in oceanic and terrestrial carbon uptake since 1982." *Nature*, 373, 326–330.

Fung, I. Y., C. J. Tucker, and C. Prentice (1987), "Application of Advanced Very High Resolution Radiometer vegetation index to study atmosphere-biosphere exchange of CO_2." *Geophysical Research*, 92, 2999–3015.

Gerbig, C., J. C. Lin, S. C. Wofsy, B. C. Daube, A. E. Andrews, B. B. Stephens, P. S. Bakwin, and C. A. Grainger (2003a), "Toward constraining regional-scale fluxes of CO_2 with atmospheric observations over a continent: 1. Observed spatial variability from airborne platforms." *Journal of Geophysical Research-Atmospheres*, 108, 4756, doi:10.1029/2002JD003018.

Gerbig, C., J. C. Lin, S. C. Wofsy, B. C. Daube, A. E. Andrews, B. B. Stephens, P. S. Bakwin, and C. A. Grainger (2003b), "Toward constraining regional-scale fluxes of CO_2 with atmospheric observations over a continent: 2. Analysis of COBRA data using a receptor-oriented framework." *Journal of Geophysical Research-Atmospheres*, 108, 4757, doi:10.1029/2003JD003770.

Gloor, M., N. Gruber, J. Sarmiento, C. L. Sabine, R. A. Feely, and C. Rödenbeck (2003), "A first estimate of present and preindustrial air-sea CO_2 flux patterns based on ocean interior carbon measurements and models." *Geophysical Research Letters*, 30, 1010, doi:10.1029/2002GL015594.

Goodale, C. L., K. Lajtha, K. J. Nadelhoffer, E. W. Boyer, and N. A. Jaworski (2002), "Forest nitrogen sinks in large eastern U. S. watersheds: estimates from forest inventory and an ecosystem model." *Biogeochemistry*, 57, 239–266.

Goward, S. N. and K. F. Huemmrich (1992), "Vegetation canopy par absorbtance and the normalized difference vegetation index: An assessment using the sail model." *Remote Sensing of Environment*, 39, 119–140.

Greco, S. and D. D. Baldocchi (1996), "Seasonal variations of CO2 and water vapour exchange rates over a temperate deciduous forest." *Global Change Biology*, 2.

Gurney, K. R., Y.-H. Chen, T. Maki, S. R. Kawa, A. Andrews, and Z. Zhu (2005), "Sensitivity of atmospheric CO_2 inversions to seasonal and interannual variations in fossil fuel emissions." *Journal of Geophysical Research-Atmospheres*, 110, D10308, doi:10.1029/2004JD005373.

Gurney, K. R., R. M. Law, A. S. Denning, P. J. Rayner, D. Baker, P. Bousquet, L. Bruhwiler, Y.-H. Chen, P. Ciais, S. Fan, I. Y. Fung, M. Gloor, M. Heimann, K. Higuchi, J. John, T. Maki, S. Maksyutov, K. Masarie, P. Peylin, M. Prather, B. C. Pak, J. Randerson, J. Sarmiento, S. Taguchi, T. Takahashi, and C.-W. Yuen (2002), "Towards robust regional estimates of CO_2 sources and sinks using atmospheric transport models." *Nature*, 415, 626–630.

Gurney, K. R., R. M. Law, A. S. Denning, P. J. Rayner, D. Baker, P. Bousquet, L. Bruhwiler, Y.-H. Chen, P. Ciais, S. M. Fan, I. Y. Fung, M. Gloor, M. Heimann, K. Higuchi, J. John, E. Kowalczyk, T. Maki, S. Maksyutov, P. Peylin, M. Prather, B. C. Pak, J. Sarmiento, S. Taguchi, T. Takahashi, and C.-W. Yuen (2003), "Transcom 3 CO_2 inversion intercomparison: 1. Annual mean control results and sensitivity to transport and prior flux information." *Tellus Series B-Chemical and Physical Meteorology*, 55, 555–579.

Gurney, K. R., R. M. Law, A. S. Denning, P. J. Rayner, B. C. Pak, D. Baker, P. Bousquet, L. Bruhwiler, Y.-H. Chen, P. Ciais, I. Y. Fung, M. Heimann, J. John, T. Maki, S. Maksyutov, P. Peylin, M. Prather, and S. Taguchi (2004), "Transcom 3 inversion intercomparison: Model mean results for the estimation of seasonal carbon sources and sinks." *Global Biogeochemical Cycles*, 18, GB1010, doi:10.1029/2003GB002111.

Haxeltine, A. and I. C. Prentice (1996), "Biome3: An equilibrium terrestrial biosphere model based on ecophysiological constraints, resource availability, and competition among plant functional types." *Global Biogeochemical Cycles*, 10, 693–710.

Heimann, M., G. Esser, A. Haxeltine, J. Kaduk, D. W. Kicklighter, W. Knorr, G. H. Kohlmaier, A. D. McGuire, J. Melillo, B. Moore III, R. D. Otto, I. C. Prentice, W. Sauf, A. Schloss, S. Sitch, U. Wittenberg, and G. Würth (1998), "Evaluation of terrestrial carbon cycle models through simulations of the seasonal cycle of atmospheric CO_2: First results of a model intercomparison study." *Global Biogeochemical Cycles*, 12, 1–24.

Heimann, M. and S. Körner (2003), "The global atmospheric tracer model TM3." Technical Report 5, Max Planck Institute for Biogeochemistry, Jena, Germany.

Heinsch, F. A., M. Reeves, P. Votava, and et. al. (2003), *User's Guide, GPP and NPP (MOD 17A2/A3) Products, NASA MODIS Land Algorithm. Version 2.0.*

Houghton, R. A. (2003), "Revised estimates of the annual net flux of carbon to the atmosphere from changes in land use and land management 1850-2000." *Tellus Series B-Chemical and Physical Meteorology*, 55, 378–390.

Houghton, R. A., J. L. Hackler, and K. T. Lawrence (1999), "The U. S. carbon budget: Contributions from land-use change." *Science*, 285, 574–578.

Houweling, S., T. Kaminski, F. J. Dentener, J. Lelieveld, and M. Heimann (1999), "Inverse modeling of methane sources and sinks using the adjoint of a global transport model." *Geophysical Research*, 104, 26,137–26,160.

Howard, D. M. and P . J. A. Howard (1993), "Relationships between CO_2 evolution, moisture content and temperature for a range of soil types." *Soil Biology and Biochemistry*, 25, 1537–1546.

Hui, Dafeng, Shiqiang Wan, Bo Su, Gabriel Katul, R. Monson, and Yiqi Luo (2004), "Gap-filling missing data in eddy covariance measurements using multiple imputation (MI) for annual estimations." *Agricultural and Forest Meteorology*, 121, 93 – 111.

Ichii, K., H. Hashimoto, R. Nemani, and M. White (2005), "Modeling the interannual variability and trends in gross and net primary productivity of tropical forests from 1982 to 1999." *Global and Planetary Change*, 48, 274–286.

IPCC AR4 (2007), "Fourth assessment report." Technical report, Intergovernmental Panel on Climate Change.

Janssens, I. A., H. Lankreijer, G. Matteucci, A. S. Kowalski, N. Buchmann, D. Epron, and et. al. (2001), "Productivity overshadows temperature in determining soil and ecosystem respiration across European forests." *Global Change Biology*, 7, 269–278(10).

Jarvis, P. G., J. Massheder, D. Hale, J. Moncrieff, M. Rayment, and S. Scott (1997), "Seasonal variation of carbon dioxide, water vapor and energy exchanges of a boreal black spruce forest." *J. Geophys. Res.*, 102, 28953–28967.

Joos, F., G.-K. Plattner, T. F. Stocker, O. Marchal, and A. Schmittner (1999), "Global warming and marine carbon cycle feedbacks and future atmospheric CO_2." *Science*, 284, 464–467.

Jung, M., K. Henkel, M. Herold, and G. Churkina (2006), "Exploiting synergies of global land cover products for carbon cycle modeling." *Remote Sensing of Environment*, 101, 534–553.

Jung, M., M. Reichstein, and A. Bondeau (2009), "Towards global empirical upscaling of FLUXNET eddy covariance observations: validation of a model tree ensemble approach using a biosphere model." *Biogeosciences*, 6, 2013.

Jung, M., M. Verstraete, N. Gobron, M. Reichstein, D. Papale, A. Bondeau, M. Robustelli, and B. Pinty (2008), "Diagnostic assessment of European gross primary production." *Global Change Biology*, 14, 2349–2364.

Kalnay, E., M. Kanamitsu, R. Kistler, W Collins, D Deaven, L Gandin, M Iredell, S Saha, G White, J Woollen, Y Zhu, M Chelliah, W Ebisuzaki, W Higgins, J Janowiak, K C Mo, C Ropelewski, J Wang, A Leetmaa, R Reynolds, R Jenne, and D Joseph (1996), "The NCEP/NCAR 40-year reanalysis project." *Bull. Am. Met. Soc.*, 77, 437–471.

Kaminski, T. and M. Heimann (2001), "Inverse modeling of atmospheric carbon dioxide fluxes." *Science*, 294, 259a–259a.

Kaminski, T., M. Heimann, and R. Giering (1999), "A coarse grid three dimensional global inverse model of the atmospheric transport: (1) Adjoint model and Jacobian matrix." *Journal of Geophysical Research*, 104, 18,535–18,553.

Kaminski, T., W. Knorr, P. J. Rayner, and M. Heimann (2002), "Assimilating atmospheric data into a terrestrial biosphere model: A case study of the seasonal cycle." *Global Biogeochemical Cycles*, 16, 1066, doi: 10.1029/2001GB001463.

Kaplan, J. O., N. H. Bigelow, I. C. Prentice, S. P. Harrison, P. J. Bartlein, T. R. Christensen, W. Cramer, N. V. Matveyeva, A. D. McGuire, D. F. Murray, V. Y. Razzhivin, B. Smith, D. A. Walker, P. M. Anderson, A. A. Andreev, L. B. Brubaker, M. Edwards, and A. Lozhkin (2003), "Climate change and Arctic ecosystems: 2. Modeling, paleodata-model comparisons, and future projections." *Journal of Geophysical Research-Atmospheres*, 108.

Keeling, C. D., R. B. Bacastow, A. F. Carter, S. C. Piper, T. P. Whorf, M. Heimann, W. G. Mook, and H. Roeloffzen (1989), "A three-dimensional model of atmospheric CO_2 transport based on observed winds: 1. Analysis of observational data In: Aspects of Climate Variability in the Pacific and Western Americas, Geophysical Monograph 55 (ed. D. H. Peterson)." *Geophysical Monograph*, 55.

Keeling, C. D., A. F. Bollenbacher, and T. P. Whorf (2005a), "Monthly atmospheric $^{13}C/^{12}C$ isotopic ratios for 10 SIO stations." In: Trends: A Compendium of Data on Global Change. Carbon Dioxide Information Analysis Center, Oak Ridge National Laboratory,

U.S. Department of Energy, Oak Ridge, TN, http://cdiac.ornl.gov/trends/co2/iso-sio/iso-sio.html.

Keeling, C. D., J. F. S. Chin, and T. P. Whorf (1996), "Increased activity of northern vegetation inferred from atmospheric CO_2 measurements." *Nature*, 382, 146–149.

Keeling, C. D., S. C. Piper, R. B. Bacastow, M. Wahlen, T. P. Whorf, M. Heimann, and H. A. Meijer (2005b), "Atmospheric CO_2 and $^{13}CO_2$ exchange with the terrestrial biosphere and oceans from 1978 to 2000: observations and carbon cycle implications." In *A History of Atmospheric CO_2 and Its Effects on Plants, Animals, and Ecosystems* (J. R. Ehleringer, T. E. Cerling, and M. D. Dearing, eds.), volume 177 of *Ecological Studies, Vol. 177*, 83–113, Springer, New York.

Keeling, C. D. and T. P. Whorf (2005), "Atmospheric CO_2 records from sites in the SIO air sampling network." In: Trends: A Compendium of Data on Global Change. Carbon Dioxide Information Analysis Center, Oak Ridge National Laboratory, U.S. Department of Energy, Oak Ridge, TN, http://cdiac.esd.ornl.gov/trends/co2/sio-keel-flask/sio-keel-flask.html.

Keeling, C. D., T. P. Whorf, M. Wahlen, and J. van der Plicht (1995), "Interannual extremes in the rate of rise of atmospheric carbon dioxide since 1980." *Nature*, 375, 666–670.

Keeling, R. F., R. P. Najjar, M. L. Bender, and P. P. Tans (1993), "What atmospheric oxygen measurements can tell us about the global carbon-cycle." *Global Biogeochemical Cycles*, 37–67.

Keller, M., M. Palace, and G. Hurtt (2001), "Biomass estimation in the Tapajos National Forest, Brazil: examination of sampling and allometric uncertainties." *Forest Ecol. Manag.*, 154, 371–382.

Kimball, J. S., A. R. Keyser, S. W. Running, and S. Saatchi (2000), "Regional assessment of boreal forest productivity using an ecological process model and remote sensing parameter maps." *Tree Physiology*, 20, 761–775.

Klein Tank, A. M. G. and G. P. Können (2003), "Trends in Indices of Daily Temperature and Precipitation Extremes in Europe, 1946–99." *Journal of Climate*, 16, 3665–3680.

Knorr, W. and M. Heimann (1995), "Impact of drought stress and other factors on seasonal land biosphere CO_2 exchange studied through an atmospheric tracer transport model." *Tellus Series B - Chemical and Physical Meteorology*, 47.

Knorr, W. and M. Heimann (2001), "Uncertainties in global terrestrial biosphere modeling 1. A comprehensive sensitivity analysis with a new photosynthesis and energy balance scheme." *Global Biogeochemical Cycles*, 15, 207–225.

Krinner, G., N. Viovy, N. de Noblet-Ducoudré, J. Ogée, J. Polcher, P. Friedlingstein, P. Ciais, S. Sitch, and I. C. Prentice (2005), "A dynamic global vegetation model for studies of the coupled atmosphere-biosphere system." *Global Biogeochemical Cycles*, 19, GB1015, doi:10.1029/2003GB002199.

Langenfelds, R. L., R. J. Francey, B. C. Pak, L. P. Steele, J. Lloyd, C. M. Trudinger, and C. E. Allison (2002), "Interannual growth rate variations of atmospheric CO_2 and its $\delta^{13}C$, h2, CH_4, and CO between 1992 and 1999 linked to biomass burning." *Global Biogeochemical Cycles*, 16, 1048, doi:10.1029/2001GB001466.

Law, B. E., O. J. Sun, J. Campbell, S. Van Tuyl, and P. E. Thornton (2003), "Changes in carbon storage and fluxes in a chronosequence of ponderosa pine." *Global Change Biology*, 9, 510–524.

Le Quéré, C., O. Aumont, L. Bopp, P. Bousquet, P. Ciais, R. Francey, M. Heimann, C. D. Keeling, R. F. Keeling, H. Kheshgi, P. Peylin, S. C. Piper, I. C. Prentice, and P. J. Rayner (2003), "Two decades of ocean CO_2 sink and variability." *Tellus Series B-Chemical and Physical Meteorology*, 55, 649–656.

Le Quéré, C., M. R. Raupach, J. G. Canadell, G. Marland, and et. al. (2009), "Trends in the sources and sinks of carbon dioxide." *Nature Geoscience*, 2, 831–836.

Leuning, R., H. A. Cleugh, S. J. Zegelin, and D. Hughes (2005), "Carbon and water fluxes over a temperate Eucalyptus forest and a tropical wet/dry savanna in Australia: measurements and comparison with MODIS remote sensing estimates." *Agricultural and Forest Meteorology*, 129(3-4), 151–173.

Levin, I., B. Kromer, M. Schmidt, and H. Sartorius (2003), "A novel approach for independent budgeting of fossil fuel CO_2 over Europe by $14CO_2$ observations." *Geophysical Research Letters*, 30, 2194, doi:10.1029/2003GL018477.

Lloyd, J. and J. A. Taylor (1994), "On the temperature dependence of soil respiration." *Functional Ecology*, 8, 315–323.

Los, S. O., N. H. Pollack, M. T. Parris, G. J. Collatz, C. J. Tucker, P. J. Sellers, C. M. Malmström, R. S. DeFries, L. Bounoua, and D. A. Dazlich (2000), "A Global 9-yr Biophysical Land Surface Dataset from NOAA AVHRR Data." *Journal of Hydrometeorology*, 1, 183–199.

Malmstrom, C. M., M. V. Thompson, and et. al. (1997), "Interannual variation in global-scale net primary production: Testing model estimates." *Global Biogeochemical Cycles*, 33, 481–486.

Manning, A. C. and R. F. Keeling (2006), "Global oceanic and land biotic carbon sinks from the scripps atmospheric oxygen flask sampling network." *Tellus Series B-Chemical and Physical Meteorology*, 58, 95–116.

Manning, M. R., A. Gomez, and G. Brailsford (1997), "Annex B11: The New Zealand CO_2 measurement programme." In: Report of the Ninth WMO Meeting of Experts on Carbon Dioxide Concentration and Related Tracer Measurement Techniques. WMO Global Atmosphere Watch No. 132; WMO TD No. 952, Commonwealth Scientific and Industrial Research Organisation, Melbourne, pp. 120–123.

Marland, G., T. A. Boden, and R. J. Andres (2006), "Global, regional, and national CO_2 emissions." In: Trends: A Compendium of Data on Global Change. Carbon Dioxide Information Analysis Center, Oak Ridge National Laboratory, U.S. Department of Energy, Oak Ridge, TN, http://cdiac.esd.ornl.gov/trends/emis/tre$_g$lob.htm.

Marland, G. and R. M. Rotty (1984), "Carbon dioxide emissions from fossil fuels: a procedure for estimation and results for 1950–1982." *Tellus Series B*, 36, 232–261.

Masarie, K. A., R. L. Langenfelds, C. E. Allison, T. J. Conway, E. J. Dlugokencky, R. J. Francey, P. C. Novelli, L. P. Steele, P. P. Tans, B. Vaughn, and J. W. C. White (2001), "NOAA/CSIRO flask air intercomparison experiment: A strategy for directly assessing consistency among atmospheric measurements made by independent laboratories." *Journal of Geophysical Research-Atmospheres*, 106, 20445–20464.

McGuire, A. D., S. Sitch, J. S. Clein, R. Dargaville, G. Esser, J. Foley, M. Heimann, F. Joos, J. Kaplan, D. W. Kicklighter, R. A. Meier, J. M. Melillo, B. Moore III, I. C. Prentice, N. Ramankutty, T. Reichenau, A. Schloss, H. Tian, L. J. Williams, and U. Wittenberg (2001), "Carbon balance of the terrestrial biosphere in the twentieth century: Analyses of CO_2, climate and land use effects with four process-based ecosystem models." *Global Biogeochemical Cycles*, 15, 183–206.

Mikaloff Fletcher, S. E., N. Gruber, A. R. Jacobson, S. C. Doney, S. Dutkiewicz, M. Gerber, M. Follows, F. Joos, K. Lindsay, D. Menemenlis, A. Mouchet, S. A. Müller, and J. L. Sarmiento (2006), "Inverse estimates of anthropogenic CO_2 uptake, transport, and storage by the ocean." *Global Biogeochemical Cycles*, 20, GB2002, doi: 10.1029/2005GB002530.

Monson, R. K., A. A. Turnipseed, R. J. Sparks, P. C. Harley, L. E. Scott-Denton, K. Sparks, and T. E. Huxman (2002), "Carbon sequestration in a high-elevation, subalpine forest." *Global Change Biologyiology*, 8, 459–478.

Monteith, J. L. (1977), "Climate and efficiency of crop production in Britain." *Philosophical Transactions of the Royal Society of London Series B - Biological Sciences*, 281, 277–294.

Nabuurs, G. J., M. Schelhaas, G. M. J. Mohren, and C. B. Field (2003), "Temporal evolution of the European forest sector carbon sink from 1950 to 1999." *Global Change Biology*, 9, 152–160.

Nemani, R. R., C. D. Keeling, H. Hashimoto, W. M. Jolly, S. C. Piper, C. J. Tucker, R. B. Myneni, and S. W. Running (2003), "Climate-driven increases in global terrestrial net primary production from 1982 to 1999." *Science*, 300, 1560–1563.

Nemani, R. R. and S. W. Running (1989), "Estimation of Regional Surface Resistance to Evapotranspiration from NDVI and Thermal-IR AVHRR Data." *Journal of Applied Meteorology*, 28, 276–284.

Nemry, B., L. Fran, J. Gérard, A. Bondeau, and M. Heimann (1999), "Comparing global models of terrestrial net primary productivity (NPP): analysis of the seasonal atmospheric CO_2 signal." *Global Change Biology*, 5, 65–76.

Norman, J. M., R. Garcia, and S. Verma (1992), "Soil Surface CO_2 Fluxes and the Carbon Budget of a Grassland." *Journal of Geophysical Research*, 97(D17), 18,845–18,853.

Ogle, K. (2003), "Implications of interveinal distance for quantum yield in C 4 grasses: a modeling and meta-analysis." *Ecophysiology*, 136, 532–542.

Pacala, S. W., G. C. Hurtt, D. Baker, P. Peylin, R. A. Houghton, R. A. Birdsey, L. Heath, E. T. Sundquist, R. F. Stallard, P. Ciais, P. Moorcroft, J. P. Caspersen, E. Shevliakova, B. Moore, G. Kohlmaier, E. Holland, M. Gloor, M. E. Harmon, S.-M. Fan, J. L. Sarmiento, C. L. Goodale, D. Schimel, and C. B. Field (2001), "Consistent land- and atmosphere-based U. S. carbon sink estimates." *Science*, 292, 2316–2320.

Papale, D. and A. Valentini (2003), "A new assessment of European forests carbon exchanges by eddy fluxes and artificial neural network spatialization." *Global Change Biology*, 9, 525–535.

Patra, P. K., D. F. Baker, P. Bousquet, L. Bruhwiler, Y. H. Chen, P. Ciais, A. S. Denning, S. M. Fan, I. Y. Fung, M. Gloor, K. R. Gurney, M. Heimann, K. Higuchi, J. John, R. M. Law, T. Maki, S. Maksyutov, T. Nakazawa, B. C. Pak, P. Peylin, M. Prather, P. J. Rayner, J. L. Sarmiento, S. Taguchi, T. Takahashi, and C. W. Yuen (2006), "Sensitivity of inverse estimation of annual mean CO_2 sources and sinks to ocean-only sites versus all-sites observational networks." *Geophysical Research Letters*, 33.

Patra, P. K. and S. Maksyutov (2003), "Sensitivity of optimal extension of CO_2 observation networks to model transport." *Tellus Series B-Chemical and Physical Meteorology*, 55, 498–511.

Pérez-Landa, G., P. Ciais, G. Gangoiti, J. L. Palau, A. Carrara, B. Gioli, F. Miglietta, M. Schumacher, M. M. Millán, and M. J. Sanz (2007), "Mesoscale circulations over complex terrain in the Valencia coastal region, Spain - Part 2: Modeling CO_2 transport using idealized surface fluxes." *Atmos. Chem. Phys.*, 7, 1851–1868.

Peters, W., A. R. Jacobson, C. Sweeney, Arlyn E. Andrews, Thomas J. Conway, Kenneth Masarie, John B. Miller, Lori M. P. Bruhwiler, Gabrielle Pétron, Adam I. Hirsch, Douglas E. J. Worthy, Guido R. van der Werf, James T. Randerson, Paul O. Wennberg, Maarten C. Krol, and Pieter P. Tans (2007), "An atmospheric perspective on North American carbon dioxide exchange: CarbonTracker." *PNAS*, 104, 18925–18930.

Peylin, P., D. Baker, J. Sarmiento, P. Ciais, and P. Bousquet (2002), "Influence of transport uncertainty on annual mean and seasonal inversions of atmospheric CO_2 data." *Journal of Geophysical Research-Atmospheres*, 107, 4385, doi:10.1029/2001JD000857.

Peylin, P., P. J. Rayner, P. Bousquet, C. Carouge, F. Hourdin, P. Heinrich, and P. Ciais (2005), "Daily CO_2 flux estimates over Europe from continuous atmospheric measurements: 1, inverse methodology." *Atmospheric Chemistry and Physics*, 5, 3173–3186.

Piper, S. C., C. D. Keeling, M. Heimann, and E. F. Stewart (2001), "Exchanges of atmospheric CO_2 and $^{13}CO_2$ with the terrestrial biosphere and oceans from 1978 to 2000. II.

A three-dimensional tracer inversion model to deduce regional fluxes." *SIO Reference No. 01-07*, 01-07.

Potter, C. S., J. T. Randerson, C. B. Field, P. A. Matson, P. M. Vitousek, H. A. Mooney, and S. A. Klooster (1993), "Terrestrial ecosystem production: a process model based on global satellite and surface data." *Global Biogeochemical Cycles*, 7, 811–841.

Prentice, I. C. (2001), "Interactions of climate change and the terrestrial biosphere." In *Geosphere-Biosphere Interactions and Climate* (L. O. Bengtsson and C. U. Hammer, eds.), 176–195, Pontifical Academy of Sciences, Cambridge.

Prentice, I. C., W. Cramer, S. P. Harrison, R. Leemans, R. MONSERUD, and A. M. Solomon (1992), "A global biome model based on plant physiology and dominance, soil properties and climate." *journal of biogeography*, 19, 117–134.

Raich, J. W., C. S. Potter, and D. Bhagawati (2002), "Interannual variability in global soil respiration, 1980-94." *Global Change Biology*, 8, 800–812.

Raich, J. W. and Potter C. S. (1995), "Global patterns of carbon dioxide emissions from soils." *Global Biogeochemical Cycles*, 9, 23–36.

Raich, J. W. and W. H. Schlesinger (1992), "The global carbon dioxide flux in soil respiration and its relationship to vegetation and climate." *Tellus Series B - Chemical and Physical Meteorology*, 44, 81–99.

Ramankutty, N. and J. A. Foley (1999), "Estimating historical changes in global land cover: Croplands from 1700 to 1992." *Global Biogeochemical Cycles*, 13, 997–1027.

Randerson, J. T., M. V. Thompson, C. M. Malmström, C. B. Field, and I. Y. Fung (1996), "Substrate limitations for heterotrophs: Implications for models that estimate the seasonal cycle of atmospheric CO_2." *Global Biogeochemical Cycles*, 10.

Rayner, P., I. Enting, R. Francey, and R. Langenfelds (1999), "Reconstructing the recent carbon cycle from atmospheric CO_2, $\delta^{13}CO_2$ and O_2/N_2 observations." *Tellus*, 51B, 213–232.

Rayner, P. J., M. Scholze, W. Knorr, T. Kaminski, R. Giering, and H. Widmann (2005), "Two decades of terrestrial carbon fluxes from a carbon cycle data assimilation system (CCDAS)." *Global Biogeochemical Cycles*, 19, GB2026, doi:10.1029/2004GB002254.

Reichstein, M., T. Kätterer, O. Andrén, P. Ciais, E.-D. Schulze, W. Cramer, D. Papale, and R. Valentini (2005), "Temparature sensitivity of decomposition in relation to soil organic matter pools: critique and outlook." *Biogeosciences*, 2, 317–321.

Reichstein, M., A. Rey, A. Freibauer, J. Tenhunen, R. Valentini, J. Banza, P. Casals, Y. F. Cheng, J. M. Grünzweig, J. Irvine, R. Joffre, B. E. Law, D. Loustau, F. Miglietta, W. Oechel, J.-M. Ourcival, J. S. Pereira, A. Peressotti, F. Ponti, Y. Qi, S. Rambal, M. Rayment, J. Romanya, F. Rossi, V. Tedeschi, G. Tirone, M. Xu, and D. Yakir (2003),

"Modeling temporal and large-scale spatial variability of soil respiration from soil water availability, temperature and vegetation productivity indices." *Global Biogeochemical Cycles*, 17, 1104, doi:10.1029/2003GB002035.

Rödenbeck, C. (2005), "Estimating CO_2 sources and sinks from atmospheric mixing ratio measurements using a global inversion of atmospheric transport." Technical Report 6, Max Planck Institute for Biogeochemistry, Jena, Germany.

Rödenbeck, C., C. Gerbig, K. Trusilova, and M. Heimann (2009), "A two-step scheme for high-resolution regional atmospheric trace gas inversions based on independent models." *Atmospheric Chemistry and Physics*, 9, 5331–5342.

Rödenbeck, C., S. Houweling, M. Gloor, and M. Heimann (2003), "CO_2 flux history 1982-2001 inferred from atmospheric data using a global inversion of atmospheric transport." *Atmospheric Chemistry and Physics*, 3, 1919–1964.

Running, S. W. (1999), "A Global Terrestrial Monitoring Network Integrating Tower Fluxes, Flask Sampling, Ecosystem Modeling and EOS Satellite Data - a comparison of estimates from a constrained quantum-use efficiency model and eddy correlation." *Remote Sensing of Environment*, 70, 108–127.

Sabine, C. L., R. A. Feely, Y. W. Watanabe, and M. Lamb (2004), "Temporal evolution of the north Pacific CO_2 uptake rate." *Journal of Oceanography*, 60, 5–15.

Schär, C. and G. Jendritzky (2004), "Climate change: Hot news from summer 2003." *Nature*, 432, 559–560.

Schimel, D., J. Melillo, H. Q. Tian, A. D. McGuire, D. Kicklighter, T. Kittel, N. Rosenbloom, S. Running, P. Thornton, D. Ojima, W. Parton, R. Kelly, M. Sykes, R. Neilson, and B. Rizzo (2000), "Contribution of increasing CO_2 and climate to carbon storage by ecosystems in the United States." *Science*, 287, 2004–2006.

Schimel, D. S., J. I. House, K. A. Hibbard, P. Bousquet, P. Ciais, P. Peylin, B. H. Braswell, M. J. Apps, D. Baker, A. Bondeau, J. Canadell, G. Churkina, W. Cramer, A. S. Denning, C. B. Field, P. Friedlingstein, C. Goodale, M. Heimann, R. A. Houghton, J. M. Melillo, B. Moore III, D. Murdiyarso, I. Noble, S. W. Pacala, I. C. Prentice, M. R. Raupach, P. J. Rayner, R. J. Scholes, W. L. Steffen, and C. Wirth (2001), "Recent patterns and mechanisms of carbon exchange by terrestrial ecosystems." *Nature*, 414, 169–172.

Scholze, M., J. O. Kaplan, W. Knorr, and M. Heimann (2003), "Climate and interannual variability of the atmosphere-biosphere 13CO_2 flux." *Geophysical Research Letters*, 30.

Schulze, E.-D. and M. Heimann (1998), "Carbon and water exchange of terrestrial systems." In *Asian change in the context of global change* (J. N. Galloway and J. Melillo, eds.), 145–161, Cambridge University Press, Cambridge.

Schulze, E.-D., C. Wirth, and M. Heimann (2000), "Managing forests after Kyoto." *Science*, 289, 2058–2059.

Seinfeld, J. H. and S. N. Pandis (1998), *Atmospheric Chemistry and Physics: From Air Pollution to Climate Change*. Wiley, New York.

Sellers, P. J. (1985), "Canopy reflectance, photosynthesis and transpiration." *International Journal of Remote Sensing*, 6, 1335–1372.

Sellers, P. J., S. O. Los, C. J. Tucker, C. O. Justice, D. A. Dazlich, G. J. Collatz, and D. A. Randall (1996a), "A revised land surface parameterization (SiB2) for atmospheric GCMs. Part II: The generation of global fields of terrestrial biophysical parameters from satellite data." *Journal of Climate*, 9, 706–737.

Sellers, P. J., D. A. Randall, G. J. Collatz, J. A. Berry, C. B. Field, D. A. Dazlich, C. Zhang, C. D. Collelo, and L. Bounoua (1996b), "A revised land surface parameterization (SiB2) for atmospheric GCMs: Part 1. Model formulation." *Journal of Climate*, 9, 676–705.

Shvidenko, A. and S. Nilsson (2003), "A synthesis of the impact of Russian forests on the global carbon budget for 1961-1998." *Tellus Series B - Chemical and Physical Meteorology*, 55, 391–415. 6th International Carbon Dioxide Conference, SENDAI, JAPAN, OCT 01-05, 2001.

Sitch, S., V. Brovkin, W. von Bloh, D. van Vuuren, B. Eickhout, and A. Ganopolski (2005), "Impact of future land cover changes on atmospheric CO_2 and climate." *Global Biogeochemical Cycles*, 19, GB2013, doi:10.1029/2004GB002311.

Sitch, S., I. Prentice, B. Smith, W. Cramer, J. Kaplan, W. Lucht, M. Sykes, K. Thonicke, and S. Venevsky (2000), "LPJ – a coupled model of vegetation dynamics and the terrestrial carbon cycle." In *The role of vegetation dynamics in the control of atmospheric CO_2 content (S. Sitch, PhD Thesis)*, Lund University, Lund (Sweden).

Sitch, S., B. Smith, I. C. Prentice, A. Arneth, A. Bondeau, W. Cramer, J. O. Kaplan, S. Levis, W. Lucht, M. T. Sykes, K. Thonicke, and S. Venevsky (2003), "Evaluation of ecosystem dynamics, plant geography and terrestrial carbon cycling in the LPJ dynamic global vegetation model." *Global Change Biology*, 9, 161–185.

Stephenson, N. L. (1990), "Climatic control of vegetation distribution: the role of the water balance." *The American Naturalist*, 135, 649–670.

Takahashi, T., S. C. Sutherland, R. Wanninkhof, C. Sweeney, R. A. Feely, and et. al. (2009), "Climatological mean and decadal changes in surface ocean pCO$_2$, and net sea-air CO_2 flux over the global oceans." *Deep Sea Res. II*, 56, 554–577.

Tans, P. P., I. Y. Fung, and T. Takahashi (1990), "Observational constraints on the global atmospheric CO_2 budget." *Science*, 247, 1431–1438.

Tarantola, A. (1987), *Inverse Problem Theory: Methods for Data Fitting and Parameter Estimation*. Elsevier, Amsterdam.

Taylor, K. E. (2001), "Summarizing multiple aspects of model performance in a single diagram." *Journal of Geophysical Research*, 106(D7), 7183–7192.

Thornton, P. E., S. W. Running, and E. R. Hunt (2005), *Biome-BGC: Terrestrial Ecosystem Process Model, Version 4.1.1. Data model.* Oak Ridge National Laboratory Distributed Active Archive Center, Oak Ridge, Tennessee, U.S.A, URL `http://www.daac.ornl.gov`.

Trenberth, K. E., P. D Jones, P. Ambenje, R. Bojariu, D. Easterling, A. Klein Tank, D. Parker, F. Rahimzadeh, J. A. Renwick, Rusticucci M., Soden B., and P. Zhai (2007), "Observations: Surface and Atmospheric Climate Change In: Climate Change 2007. The Physical Science Basis. Contribution of WG 1 to the Fourth Assessment Report of the Intergovernmental Panel on Climate Change (IPCC)."

Trusilova, K. and G. Churkina (2008), "The terrestrial ecosystem model BIOME-BGC v1." Technical Report 14, MPI BGC, Jena (Germany).

Trusilova, K., J. Trembath, and G. Churkina (2009), "Parameter estimation and validation of the terrestrial ecosystem model BIOME-BGC using eddy-covariance flux measurments." Technical Report 16, MPI BGC, Jena, Germany.

Tucker, C. J, J. E. Pinzon, M. E. Brown, D. Slayback, E. W. Pak, R. Mahoney, E. F. Vermote, and N. E. Saleous (2005), "An Extended AVHRR 8-km NDVI Data Set Compatible with MODIS and SPOT Vegetation NDVI Data." *International Journal of Remote Sensing*, 26, 4485–5598.

Tucker, C.J. (1979), "Red and photographic infrared linear combinations for monitoring vegetation." *Remote Sensing of Environment*, 8, 127–150.

UN-ECE/FAO (2000), "Forest resources of Europe, CIS, North America, Australia, Japan and New Zealand (industrialized temperate/boreal countries) UN-ECE/FAO contribution to the global forest resources assessment 2000. (United Nations Economics Commission for Europe/Food and Agricultural Organisation on the United Nations)." *Geneva Timber and Forest Study Papers. United Nations, New York, Geneva*, No.17, 445.

UNFCCC (2000), "(United Nations Framework Convention on Climate Change):Methodological issue. Land-use, land-use change and forestry. Synthesis Report on National Greenhouse Gas Infromation Reported by Annexe I Parties for the Land-use Change and Forestry Sector and Agriclutural Soils Category. Note by the tariat, Sbsidiary Body for Scientific and Technical Advice." Technical report, FCCC/SBSTA/2000/3, Bonn, Germany.

van der Molen, M. K. and A. J. Dolman (2007), "Regional carbon fluxes and the effect of topography on the variability of atmospheric CO_2." *Journal of Geophysical Research-Atmospheres*, 112, D01104, doi:10.1029/2006JD007649.

van der Werf, G. R., J. T. Randerson, G. J. Collatz, L. Giglio, P. Kasibhatla, A. Arellano, S. C. Olsen, and E. S. Kasischke (2004), "Continental-scale partitioning of fire emissions during the 1997 to 2001 El Nino/La Nina period." *Science*, 303, 73–76.

van der Werf, G. R., J. T. Randerson, L. Giglio, G. J. Collatz, and P. Kasibhatla (2006), "Interannual variability in global biomass burning emission from 1997 to 2004." *Atmospheric Chemistry and Physics*, 6, 3423–3441.

van der Werf, G. R., J. T. Randerson, L. Giglio, G. J. Collatz, M. Mu, P. Kasibhatla, and et. al. (2010), "Global fire emissions and the contribution of deforestation, savanna, forest, agricultural, and peat fires (1997–2009)." *Atmospheric Chemistry and Physics Discussions*, 10, 16153–16230.

van Wesemael, B., S. Lettens, C. Roelandt, and J. Van Orshoven (2005), "Modelling the evolution of regional carbon stocks in Belgian cropland soils." *Canadian Journal of soil science*, 85, 511–521. Meeting on Soil Organic Carbon and Agriculture - Developing Indicators for Policy Analyses, Ottawa, CANADA, OCT, 2002.

Vermote, E. and Y. J. Kaufman (1995), "Absolute calibration of AVHRR visible and near-infrared channels using ocean and cloud views." *International Journal of Remote Sensing*, 16, 2317–2340.

Vetter, M., G. Churkina, M. Jung, M. Reichstein, S. Zaehle, A. Bondeau, Y. Chen, P. Ciais, F. Feser, A. Freibauer, R. Geyer, C. Jones, D. Papale, J. Tenhunen, E. Tomelleri, K. Trusilova, N. Viovy, and M. Heimann (2008), "Analyzing the causes and spatial pattern of the European 2003 carbon flux anomaly using seven models." *Biogeosciences*, 5, 561–583.

Vetter, M., C. Wirth, H. Böttcher, G. Churkina, E.-D. Schulze, T. Wutzler, and G. Weber (2005), "Partitioning direct and indirect human-induced effects on carbon sequestration of managed coniferous forests using model simulations and forest inventories." *Global Change Biology*, 11, 810–827.

White, W. B., J. Lean, D. R. Cayan, and M. D. Dettinger (1997), "Response of global upper ocean temperature to changing solar irradiance." *Journal of Geophysical Research-Oceans*, 102, 3255–3266.

Xiao, J. F., Q. L. Zhuang, D. D. Baldocchi, and et. al. (2008), "Estimation of net ecosystem carbon exchange for the conterminous United States by combining MODIS and AmeriFlux data." *Agricultural and Forest Meteorology*, 148, 1827–1847.

Yang, F., K. Ichii, M. White, H. Hashimoto, A. Michaelis, P. Votava, A. Zhu, A. Huete, S. Running, and R. Nemani (2007), "Developing a continental-scale measure of gross primary production by combining MODIS and AmeriFlux data through Support Vector Machine approach." *Remote Sensing of Environment*, 110, 109 – 122.

Zhao, M. and S. W. Running (2010), "Drought-induced reduction in global terrestrial net primary production from 2000 through 2009." *Sience*, 329, 940–943.